

Stellingen behorende bij het proefschrift:

Instrumentatie voor Parallel-Parallel Coincidentie Elektronen Spectroscopie

- 1 Het grootste probleem van parallelle detectoren is de dataverwerking, die, als hij eveneens parallel uitgevoerd wordt, een veelvoud van de kosten van de eigenlijke detector met zich mee brengt.
- 2 Een parallelle detector met een parallel dataverwerkingssysteem behoort als een enkel systeem gezien te worden, vanuit dit oogpunt verdient het de voorkeur om zoveel mogelijk onderdelen van dit systeem te integreren.
- 3 De ontwikkeling van betere en goedkopere CCD cameras zal er voor zorgen dat er binnen tien jaar transmissie elektronen microscopen op de markt komen die enkel een CCD camera hebben.
- 4 De trend in de IC industrie naar steeds kleinere dimensies zal een vraag doen ontstaan naar element-specifieke technieken met bijpassende hoge spatiele resolutie, zoals Auger spectroscopie in een SEM.
- 5 De toenemende eisen aan geladen deeltjes optische systemen, wat betreft resolutie en combinatie van analytische technieken, zullen slechts met complexere systemen (bestaande uit meer optische elementen) opgelost kunnen worden.
- 6 De steeds complexere eisen aan geladen deeltjes optische systemen maken de toepassing van computer ondersteunde ontwerp technieken onvermijdelijk, en met het ontstaan van geschikte software zullen nog geavanceerder systemen ontworpen worden.
- 7 Gezien de hoge kosten van clean-room ruimte, en de onvriendelijkheid van deze omgeving voor de mens, verdient het de voorkeur elektronen microscopen die in een dergelijke ruimte moeten staan op afstand te besturen.
- 8 De hoge verspreidingsgraad van het Internet maakt dit de enige logische keuze om elektronen microscopen op afstand te besturen.
- 9 De immer groeiende grafische kwaliteit van computer spellen is een zegen voor de wetenschap, daar het de kosten van snelle computers drukt.
- 10 Dat relatief veel goede Science Fiction schrijvers een natuurkundige achtergrond hebben komt doordat een grondige kennis van de beperkingen nodig is om de kleinst mogelijke aanname, met de grootst mogelijke gevolgen, te kunnen verzinnen.

Propositions accompanying the thesis:

Instrumentation for Parallel-Parallel Coincidence Electron Spectroscopy

- 1 The largest problem with parallel detectors is the data processing, which, if it is also implemented in parallel, will result in an overall cost that is a multiple of the actual detector price.
- 2 A parallel detector with a parallel data processing system should be seen as a single system, seen from this viewpoint as many parts of the system should be integrated as possible.
- 3 The development of cheaper and better quality CCD cameras will result, within ten years, in the introduction of transmission electron microscopes equipped with only such a camera.
- 4 The trend in the IC industry to ever smaller dimensions will create a demand for element-specific tools with corresponding high spatial resolution, such as Auger spectroscopy in a SEM.
- 5 The increasing demands, in the way of resolution and combination of analytical techniques, on charged particle optical systems will only be met by more complex systems (consisting of more optical elements).
- 6 The increasing demands on charged particle optical systems will make the use of computer-assisted design techniques inevitable, and with the development of suitable software even more complex systems will be designed.
- 7 Considering the high costs of clean-room space, and the unfriendliness of this environment for humans it should be preferred to control electron microscopes that need to be situated in such areas remotely.
- 8 The high penetration of the Internet makes this the only logical choice for remote control of electron microscopes.
- 9 The ever growing graphical qualities of computer games is a blessing for science, as it reduces the costs of high performance computing.
- 10 The reason that relatively many great Science Fiction writers have a physics background is that it requires a thorough understanding of the limits, to be able to think of the smallest possible change, with the largest possible consequences.

TR diss
2800

**Instrumentation for Parallel-Parallel Coincidence
Electron Spectroscopy**

Instrumentation for Parallel-Parallel Coincidence Electron Spectroscopy



PROEFSCHRIFT

ter verkrijging van de graad van doctor
aan de Technische Universiteit Delft,
op gezag van de Rector Magnificus Prof. ir. K.F. Wakker,
in het openbaar te verdedigen ten overstaan van een commissie,
door het College van Dekanen aangewezen,
op donderdag 19 september 1996 te 16:00 uur
door

Jacob Simon FABER

natuurkundig ingenieur
geboren te Amsterdam

Dit proefschrift is goedgekeurd door de promotor:
Prof. dr. ir. P. Kruit

Samenstelling promotiecommissie:

Rector Magnificus,	voorzitter
Prof. dr. ir. P. Kruit,	TU Delft, promotor
Prof. dr. ir. C.W.E. van Eijk,	TU Delft
Prof. dr. W. Th. Wenckebach,	TU Delft
Prof. dr. ir. A. F. Mehlkopf,	TU Delft
Prof. dr. ir. H.F. van Beek,	TU Delft
Dr. ir. R.H.J. Fastenau,	Philips Electron Optics B.V.

This work was part of a research program of the Foundation for Fundamental Research on Matter (FOM) and was financially supported under contract no. DTN-11.2521.

Cover design by Thrua Faber.

Printed by Barten & Semler Offset., Eindhoven.

ISBN 90-9009862-3

Copyright ©1996 by J.S. Faber.

Contents

Preface	9
Introduction	9
Acknowledgments	10
References	10
1 Introduction to coincidence electron spectroscopy	11
1.1 An overview of analytical techniques in electron microscopy	11
1.2 History of coincidence electron spectroscopy in TEM	11
1.3 Coincidence electron spectroscopy system requirements	12
1.4 An overview of the Delft Auger microscope	14
1.5 References	15
2 Component requirements	17
2.1 The interplay between component requirements	17
2.2 Requirements on the optics	18
2.2.1 Illumination optics	18
2.2.2 Energy loss analysis optics	19
2.2.3 Auger energy analysis optics	19
2.3 Requirements on the detectors	19
2.3.1 Energy loss detector	20
2.3.2 Auger electron detector	20
2.4 Requirements on the data acquisition system	22
2.5 Requirements on the microscope control system	22
2.6 References	23
3 Optics	25
3.1 Introduction	25
3.2 Illumination optics	25
3.2.1 Illumination optics overview	25
3.2.2 Optimum condenser-side lens settings	26
3.3 Energy loss analysis optics	32
3.3.1 Energy loss analysis optics overview	32
3.3.2 Post-spectrometer optics requirements	32
3.3.3 Post-spectrometer optics design	34
3.3.4 Post-spectrometer mechanics	35
3.4 Auger energy analysis optics	36
3.4.1 Auger energy analysis optics overview	36
3.4.2 Transport optics	37
3.4.3 Time-of-flight variations	37
3.5 References	43

4 Microscope control system	45
4.1 Introduction	45
4.2 User interface	45
4.2.1 Necessity of computer control	45
4.2.2 User interface	45
4.2.3 Philips CM series interface	46
4.2.4 Auger microscope user interface	46
4.3 Brief introduction to the P80 computer controlled power supply system	48
4.4 Illumination system	50
4.4.1 Beam deflection, alignment and stigmatism control	50
4.5 Energy loss analysis system	55
4.5.1 Spectrometer control	56
4.5.2 Post-spectrometer optics control	57
4.6 Auger energy analysis optics	58
4.6.1 Parallelizer control	58
4.6.2 Auger electron deflector control	59
4.6.3 Auger electron deflector alignment	61
4.6.4 Transport optics and analyzer control	62
4.6.5 Transport optics and analyzer alignments	62
4.7 Remote control interface	63
4.7.1 Analog interface	63
4.7.2 Serial interface	64
4.8 References	64
5 Detectors	67
5.1 Introduction; A summary of detector requirements	67
5.2 Detectors described in literature and detector choice	67
5.2.1 Detector literature study	67
5.2.2 Micro channel plate literature study	68
5.2.3 Detector choice	69
5.3 Test of the detector and the pre-amp/discriminator combination	70
5.4 Multi strip anode detector design considerations	71
5.4.1 Electrical aspects	71
5.4.2 Mechanical aspects	73
5.5 Energy loss electron detector design	75
5.5.1 Increasing MCP efficiency for 100 keV electrons	75
5.5.2 Energy loss detector design	76
5.6 Auger electron detector design	77
5.6.1 Anode shape	77
5.6.2 Auger detector feedthrough	79
5.6.3 Detector housing	79
5.6.4 Detector connector	81
5.6.5 Glass-tungsten detector	82
5.6.6 Stycast detector	83

5.7 References	85
6 Data acquisition system	87
6.1 Introduction; design philosophy	87
6.2 System requirements	87
6.3 System overview	88
6.4 CES hardware	90
6.4.1 Signal pre-processing	90
6.4.2 PCOS system	91
6.4.3 Delays	93
6.4.4 Trigger unit	94
6.4.5 Transputer hardware	95
6.5 CES software	97
6.5.1 Transputer software	97
6.5.2 PC software	99
6.6 Automatic tuning procedures	101
6.6.1 Time window search	101
6.6.2 TDC enable window	103
6.6.3 PCOS enable window	104
6.6.4 Peak find routine	105
6.7 References	105
7 Measurements	107
7.1 Introduction	107
7.2 Characterization of the primary beam at the specimen position	107
7.3 Auger spectroscopy	110
7.4 Energy loss spectroscopy	114
7.5 Coincidence Spectroscopy	115
7.5.1 CES test measurements	115
7.5.2 Time spectrum	115
7.6 Data acquisition system performance	118
7.7 References	119
Appendix A - Alignment procedures	121
A.1 Illumination optics alignment	121
A.1.1 Getting light	121
A.1.2 Gun tilt and shift alignment	122
A.1.3 C2 aperture alignment	122
A.1.4 Tilt pivot point alignment	123
A.1.5 Beam tilt alignment	124
A.1.6 Shift pivot point alignment	124
A.1.7 12-pole alignment	124
A.2 Auger electron optics alignment	125
A.2.1 Parallelizer coil alignment	125

Contents

A.2.2 Auger deflector alignment	126
A.2.3 Transport lens alignment	128
A.2.4 Auger spectrometer alignment	128
A.3 References	130
Appendix B - Tables	131
B.1 Spectra file format	131
B.2 Transport lens settings	133
B.3 Remote control commands	135
Summary	137
Samenvatting	139
Curriculum vitae	141

Preface

Introduction

In 1983 an article called '*Magnetic field paralleliser for 2π electron-spectrometer and electron-image magnifier*' was published by Kruit and Read¹. This article describes a device in which a specially shaped magnetic field (the parallelizer) collects electrons emitted over a solid angle of 2π steradians, bringing them together in a beam with a half opening angle of only 2° . Pieter Kruit realized that this parallelizer could also be included in the objective lens of a transmission electron microscope, enabling efficient collection of secondary and Auger electrons, and in 1987 a project was started in the Particle Optics Group in Delft to build such a microscope.

One of the first experiments, done in a prototype of this microscope, was the detection of energy loss and secondary electrons in time coincidence. The advantage of this technique is that it should be possible to decrease the background in Auger spectra, which together with the high spatial resolution of the transmission electron microscope would allow elemental analysis at nanometer scale. Another application is the study of secondary and Auger electron production mechanisms, and the escape paths of these electrons from the specimen. Folbert Pijper² showed the feasibility of detecting coincidences and published the first measurements ever on the production of secondary electrons in a carbon foil. Because the vacuum in the prototype instrument was not good enough, contamination prevented him from doing work on other materials.

The vacuum problem was solved in the redesign of a Philips EM430 microscope by Arno Bleeker³. In this redesign the entire objective lens section was replaced by a parallelizer objective lens, with ultra high vacuum (UHV) conditions around the specimen. Also part of this design were a deflector to separate the secondary and Auger electrons from the primary electron beam and an Auger electron energy spectrometer.

An UHV-compatible specimen stage, based on piezo-electric actuators, was designed by André van Voorst. He also designed a preparation chamber directly connected to the microscope, a transport systems to move specimens between the preparation chamber and the microscope, as well as a load lock to move specimens between the preparation chamber and the outside environment.

In this thesis the completion of the modified EM430 is described, consisting of parallel detectors for both the energy loss and the Auger electrons, a data acquisition system for these detectors, a computerized microscope control system, the replacement of the thermionic electron source by a high brightness Schottky field emission electron source, and the design and construction of an optical system to match the energy loss spectrometer to the parallel detector.

Acknowledgments

Henk Hoever's has read the entire manuscript, and given it back full of comments, without which this thesis would have been a lot worse than it is now. Working with him has been a pleasure and I wish to thank him for many useful discussions, especially because these were not all about work. André van Voorst has done an enormous amount of work on the microscope, for which I'm grateful. Harold Brink has enormously helped me by very independently designing and building the post-spectrometer optics. Jan de Loeff, Peter van der Reijken and Bram Huis have helped me solve many mechanical problems, even though these usually popped up on Friday afternoons. Working out the electronics of the microscope control system and the field emission source with Jacques Nonhebel was a pleasure. Without Rob Hollander, Victor Bom and Jef Dirker the data acquisition system would not have been designed and built. I am indebted to Aad van der Lingen for all the effort he put in making the golden anodes on the Auger electron detector. With Erik van Straten and Michiel van der Stam I have had many discussions, some of these were even not about computers. Last but not least I wish to thank Nien and my parents, Dies and Theo, for their support.

References

1. P. Kruit and F.H. Read, Magnetic field paralleliser for 2π electron-spectrometer and electron-image magnifier, *J. Phys. E: Sci. Instrum.* **16** (1983), 313-324.
2. F.J. Pijper, *Possibilities for Coincidence Spectroscopy in the Scanning Transmission Electron Microscope*, Ph.D. thesis Delft University of Technology, the Netherlands (1993).
3. A.J. Bleeker, *Optical and mechanical design for 1 nm resolution Auger spectroscopy in an Electron Microscope*, Ph.D. thesis Delft University of Technology, the Netherlands (1991).

1 Introduction to coincidence electron spectroscopy

This chapter starts with an introduction to coincidence electron spectroscopy, followed by the system requirements for this technique. The last section of this chapter gives an overview of the microscope as it was at the start of this project, and the changes that have been made to make it suitable for the coincidence technique.

1.1 An overview of analytical techniques in electron microscopy

Analytical techniques are based on the observation of signals from a specimen which is excited in some way. In electron microscopy the stimulus is an electron beam which illuminates the specimen under observation. The advantage, compared to other stimuli, of an electron beam is the very short wavelength of electrons, making it possible to illuminate a very small area on the specimen, down to (in principle even below) the atomic scale.

Depending on the emitted radiation we can distinguish the following techniques: if the incident electron is re-emitted (transmission or reflection) we can study the angle over which it has scattered (High Energy Electron diffraction, HEED) or we can study the energy loss it has experienced (Electron Energy Loss Spectroscopy, EELS). The energy lost can lead to the production of several types of emitted radiation: secondary electrons (Secondary Electron Spectroscopy, SES), Auger electrons (Auger Electron Spectroscopy, AES) or photons (Energy Dispersive X-ray analysis, EDX, Wavelength Dispersive X-ray analysis, WDX, and Cathode Luminescence, CL).

Most of the above techniques can be combined in a coincidence experiment: the incident beam consists of individual electrons, so the interactions in the specimen are unique events. If such an interaction leads to two types of radiation being emitted, and if we detect both these types of radiation in a very short time interval, we can assume that they arose from the same event in the specimen. The advantage of the coincidence technique is that it can provide extra information (for instance about signal production mechanisms) or that it can lower the signal background (if the background consists of mainly non-coincident events).

Our microscope has been designed for coincidence electron spectroscopy (CES), the detection of coincidences between energy selected energy loss electrons and energy selected secondary or Auger electrons. The advantage of performing this experiment in a Transmission Electron Microscope (TEM) is the high spatial resolution that can be obtained; our aim is for 1 nm resolution.

1.2 History of coincidence electron spectroscopy in TEM

The first electron-electron coincidence experiments were done in the 1960's with the aim of mapping atomic or molecular wave functions. Coincidence experiments are easier to perform on gases than on solids because in solids only a fraction of the secondary or Auger electrons can

1. Introduction to coincidence electron spectroscopy

escape. The first experiments were done on gases for this reason, and the first coincidence experiment on a solid sample (a thin carbon foil) was done by Amaldi *et al.*¹ in 1969.

The first coincidence experiments in electron microscopes were aimed at the study of secondary electron production mechanisms. In 1976 Voreades² detected all (without energy selection) secondary electrons in coincidence with energy selected energy loss electrons and was able to conclude that most secondary electrons are produced by losses of about 20 eV and that the escape depth of secondary electrons is about 3 nm. In 1991 Pijper and Kruit³ were able to also energy-select the secondary electrons and measured the average production probability of these electrons as a function of the energy loss. They concluded that for energy losses up to 125 eV the average production probability rises linearly with the energy loss, and that above 125 eV the production probability is roughly constant. In 1992 Müllejans⁴ found the same linear relation, but then up to 1000 eV. His conclusion was that the flattening at 125 eV was an artifact caused by instrumental background.

The instrumentation described in this thesis is a follow-up of the microscope used by Pijper and Kruit.

1.3 Coincidence electron spectroscopy system requirements

Count rates

A study of the count rates that can be expected is useful because it reveals several aspects of the coincidence experiment that are of importance. First of all we will look at the non-coincident energy loss and secondary-electron count rates, R_{el} and R_{se} , respectively. Under the assumption that dead-time effects do not play a role these rates are given by

$$R_{el} = \frac{I}{e} n t \sigma_{el} f_{el} \eta_{el} \quad (1.1a)$$

$$R_{se} = \frac{I}{e} n t \sigma_{se} f_{se} \eta_{se}, \quad (1.1b)$$

where I is the primary electron beam (probe) current, e is the electron charge, n is the atomic density of the specimen, and t is the thickness of the specimen. The cross section σ , the fraction f that can escape from the specimen, and the collection and detection efficiency η , are a function of the energy loss and secondary electron energy, as indicated by their indices. The coincident count rate R_c is given by

$$R_c = \frac{I}{e} n t \sigma_c f_{el} f_{se} \eta_{el} \eta_{se} + \tau_c R_{el} R_{se}, \quad (1.2)$$

where τ_c is the width of the coincidence time window. It is assumed that the time window is so wide that all coincidence events fall in it. This sets a lower limit on τ_c , because it means that τ_c must be larger than the time-of-flight (TOF) variations that the electrons have when traveling from specimen to detectors.

The first term in Eq. 1.2 contains the rate of the true coincidences, which are the events where we detect both the energy loss and the secondary electron that come from the same event

in the specimen. The second term in Eq. 1.2 contains the false coincidences, which are caused by energy loss and secondary electrons from two distinct events in the specimen happening to fall in the same time window.

The first thing we can learn from Eq. 1.2 is that, unless the detection and collection efficiencies η_{el} and η_{se} are close to 100%, the coincidence rates are lower than the non-coincident rates. This can lead to longer measurement times, and increased risk of specimen contamination and drift. It should be noted that, if the coincidence experiment is used to lower the signal background, a lower total number of counts may already be sufficient for a good signal to noise ratio, and that it is not necessarily so that we need to measure for longer periods of time.

The second thing we can learn is that, to compensate for the lower count rates, we cannot increase the probe current I beyond a certain value. This is because the false coincidence term in Eq. 1.2 rises with the square of I , and if the current becomes too large the true coincidences will drown in the false coincidences. There are three ways around this problem. The first is to decrease the time window width τ_c to its minimum value (limited by the TOF). The second is to estimate the false coincidence contribution by measuring in a second time window which is positioned in time in such a way that the true coincidences do not fall in it. We can then subtract the estimated false background from the total signal. The third is to use parallel detectors, measuring not only coincidences between one energy loss and one secondary electron energy, but between many energy losses and many secondary electron energies simultaneously.

Specimen environment

Because secondary and Auger electrons can only escape from the topmost atomic layers of a specimen, any technique involving them is surface-sensitive. This means that specimens have to be free of contamination during a measurement, and if we look at the rate at which contamination is deposited we can conclude that only ultra high vacuum (UHV, less than 10^{-7} Pa.) conditions can keep a specimen clean long enough. This also means that we need a means of preparing or cleaning a specimen, either in situ, or in a UHV preparation chamber from which it can be transported under vacuum to the microscope.

High resolution transmission electron microscopy

It must be realized that (scanning) transmission electron microscopes obtain their high spatial resolution at the cost of great stability. As an example the microscope, especially the specimen stage, must be insensitive to mechanical vibrations and temperature fluctuations and must be insensitive to outside magnetic fields. These requirements must of course still be met. An additional complication is that the collection and energy analysis of the secondary electrons may not disturb the primary electron beam, if we wish to make nanometre scale analytical measurements, the beam must be stable within a nanometre.

Summary

The optics should collect and transport as much of the emitted signals as possible, and should provide an illumination current that is the maximum which still provides an adequate true over false ratio. The detectors should have a high detection efficiency, and must be able to handle the count rates associated with the maximum illumination current. Finally the microscope should still reach the performance level of a conventional (S)TEM.

1.4 An overview of the Delft Auger microscope

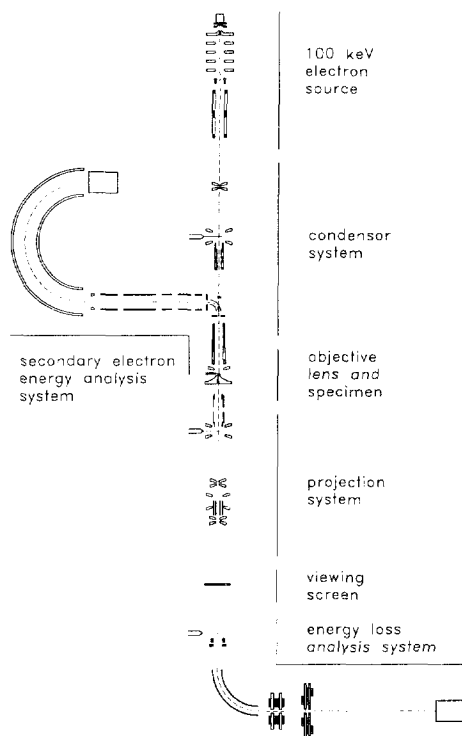


Figure 1.1 An overview of the Delft Auger electron microscope.

The microscope, which started out as a Philips EM430, is shown in Figure 1.1. In this section the main modifications will be discussed.

At the top we have the 100 keV electron source; the original thermionic source has been replaced by a (much brighter) Schottky field emission source (see Chap. 3). The condenser system, which together with the objective lens focuses the beam to a small probe, is still original; the scan coils in the condenser system, which scan the probe over the specimen, have however been brought under computer control (see Chap. 4). The objective lens has been replaced by the design of Bleeker, which is optimized for the collection of secondary and Auger electrons. Inserted above the objective lens is the achromatic deflector for the separation of the secondary electrons from the primary beam (also designed by Bleeker). Both these sections are ultra high vacuum compatible. The specimen stage inside the objective lens has been designed by Van Voorst and is based on piezo-electric actuators.

The (energy loss) electrons that pass through the specimen are imaged on the fluorescent screen by the (original) projection system. In this mode the microscope operates as a conventional TEM. Alternatively the screen can be moved aside, and the electrons enter the energy loss

analysis system. For the energy dispersion we use a commercial Gatan spectrometer, followed by a custom post-spectrometer system and the detector (see Chap. 5).

The secondary electrons that leave the achromatic deflector are transported to the spectrometer by an electrostatic lens system, which has been designed by van der Stam. The spectrometer has been designed by Bleeker. The energy dispersed secondary (or Auger) electrons are detected by a detector that is discussed in Chap. 5.

Not shown are the microscope control computer (see Chap. 4), the data acquisition system (see Chap. 6), and the specimen preparation chamber.

1.5 References

1. U. Amaldi, Jr., A. Egidi, R. Marconero and G. Pizella, Use of a two channeltron coincidence in a new line of research in atomic physics, *Rev. Sci. Instrum.* **40** (1969), 1001.
2. D. Voreades, Secondary electron emission from thin carbon films, *Surf. Sci.* **60** (1976), 325.
3. F.J. Pijper and P. Kruit, Detection of energy-selected secondary electrons in coincidence with energy-loss events in thin carbon foils, *Phys. Rev. B.* **44** (1991), 9192-9200.
4. H. Mülleijans, *Secondary Electron Emission in Coincidence with Primary Energy Losses*, Ph.D. thesis University of Cambridge (1992).

2 Component requirements

In this chapter the microscope is divided into components and the requirements on these components are derived. Special attention is paid to the interaction between components.

2.1 The interplay between component requirements

Two different methods have been used to divide the microscope into smaller pieces. The first method divides the microscope into three sub-systems (optics, detectors, and data acquisition system) which each perform a specific task. The optics sub-system is further subdivided into the illumination optics, the energy loss analysis optics, and Auger electron energy analysis optics. The advantage of this division is that the sub-systems can be designed and build fairly independently. For the microscope control system this division is however not practical, because the control system should provide a uniform interface for the whole microscope. Therefore a second method has been used to divide the microscope, this time into four layers: hardware (mechanics), electronics, software, and user interface. Figure 2.1 schematically displays both methods of division.

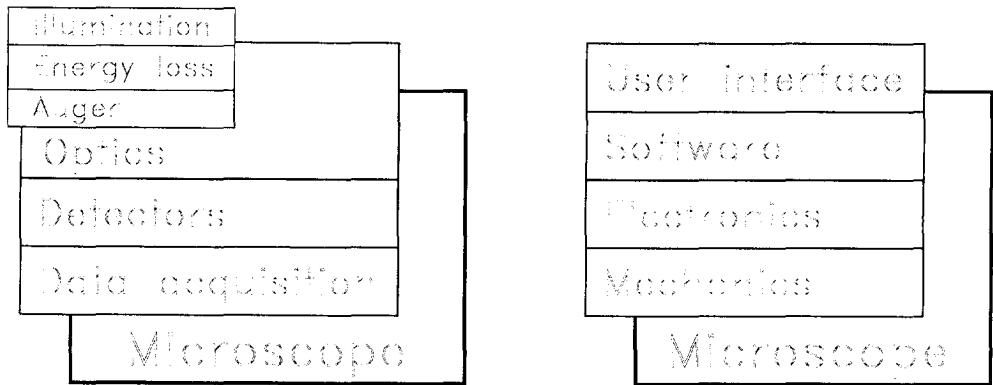


Figure 2.1 The microscope has been subdivided using two methods. The first method divides it into optics (in turn subdivided into illumination optics, energy loss optics, and Auger optics), detectors, and data acquisition system. The second method divides it into user interface, software, electronics, and mechanics.

Although subdividing the microscope assumes independent parts this is of course never completely so. Especially the interplay between the components, which after all *together* have to provide a specific functionality, is an important aspect. This interplay is strongest in the detectors and data acquisition system: the acquisition system requirements strongly depend on the types of detectors used. Another region of interplay is the spectrometer-detector matching, to match the energy loss spectrometer to the detector extra optics are required (to enlarge the

2. From system requirements to component requirements

spectrum). A final region of interplay is around the Auger electron deflector, which is necessary for the Auger electrons, but also influences the illumination optics.

2.2 Requirements on the optics

The optics can be divided into three almost independent parts: the illumination optics, the energy loss analysis optics, and the Auger electron analysis optics. Each of these will be discussed below.

2.2.1 Illumination optics

The illumination optics should provide two modes of illumination. In Transmission Electron Microscopy (TEM) mode a parallel beam illuminates the specimen over a relatively large area, and the projection system makes an enlarged image of the specimen on the viewing screen. In Scanning Transmission Electron Microscopy (STEM) mode the beam is focused to a small probe which is scanned over the specimen, and at every step in the scan the intensity of some signal from the specimen is recorded. The Auger microscope is intended to be used in STEM mode, so this is where the emphasis lies. Although the design of this part of the microscope has already been done, it is still useful to look over the demands, so that we have a clear goal in Chap. 3 where we search for optimum illumination system settings.

Basically the smaller the spot size the better (because the spatial resolution is improved), and the higher the current in the spot the better (because of shorter measurement times). The design for the optical system by Bleeker¹ aims for a 1 nm diameter spot with 1 nA of current in it, and his design of the objective lens is such that, with a Schottky field emission gun, this goal should be within reach.

Maximum spot current

An upper limit to the current in the spot is given by the time resolution with which coincidences can be detected: as the current goes up, the false (random) coincidence rate increases more rapidly than the true coincidence rate, so the true-to-false ratio becomes worse. This can be seen in Eq. 1.2, where the first term represents the true coincidence rate and the second term represents the false coincidence rate. Taking the ratio of these two terms, we get the true-over-false ratio, which is given by

$$\frac{R_{true}}{R_{false}} = \frac{e \sigma_c}{I n t \tau_c \sigma_{el} \sigma_{se}}, \quad (2.1)$$

where e is the electron charge, I is the probe current, n is the atomic density of the specimen, t is the specimen thickness, τ_c is the time window with, and σ_c , σ_{el} , and σ_{se} are the coincidence, energy loss, and secondary-electron cross sections, respectively.

The true coincidence rate (detecting an Auger electron in coincidence with the energy loss electron that created it) of course goes linearly with the probe current I . The false coincidence rate (detecting an Auger electron not in coincidence with the energy loss electron that caused it, but with another electron that happened to pass through the sample almost simultaneously) goes with

the product of the *square* of the current and the coincidence window width τ_c . This means that, the smaller τ_c is, the higher the illumination current can be, before the true coincidences drown in the background of random coincidences. The minimum coincidence window width is determined by the width of the coincidence peak in the time spectrum.

The width of the peak in the time spectrum depends both on the time scale at which the processes in the sample occur (negligibly small) and on the variations in time-of-flight (TOF) from sample to detector (typically in the order of 1 ns, see *timing resolution* in section 2.3.1). Taking $\tau_c = 1$ ns, assuming a mean free path $\lambda = 1/n\sigma_{el} = 70$ nm, a specimen thickness $t = 70$ nm, and assuming $\sigma_c = \sigma_{se}$, we find that I can be 0.16 nA for a true-over-false ratio of one.

2.2.2 Energy loss analysis optics

Because the inelastic scattering angles in the specimen are small, the imaging optics of the microscope can collect nearly 100% of the energy loss electrons. A Gatan model 607 energy loss spectrometer energy disperses the electrons, which is necessary as there are no suitable detectors that provide sufficient energy resolution. Because the spectrometer provides an energy spectrum that consists of $2 \mu\text{m}$ spots displaced $2 \mu\text{m eV}^{-1}$, while the detector needs $250 \mu\text{m} \times 50 \text{mm}$ spots (for count rate reasons), we need post spectrometer optics to further enlarge the energy spectrum.

2.2.3 Auger energy analysis optics

The Auger analysis optics has been designed (and built) completely, so only a brief description is given here. The redesigned objective lens and the parallelizer collect the secondary and Auger electrons with nearly 100% collection efficiency². The next step is the separation of the Auger electrons from the primary electron beam (traveling in opposite direction). This is done by the Auger electron deflector³. A transport system between the Auger electron deflector and the spectrometer has been designed by van der Stam⁴. Because there is no energy sensitive detector providing sufficient energy resolution, the optics should provide energy dispersion. A 180° concentric hemispherical electrostatic spectrometer is used for this. The detector can be placed directly after the spectrometer.

2.3 Requirements on the detectors

The requirements on both detectors, taking into account the existing optics of the microscope, have previously been derived⁵, the results of this work are summarized below.

Timing resolution

The time resolution of the detectors should preferably be somewhat better than the width of the coincidence time peak. This width mainly depends on the time-of-flight (TOF) variations of the Auger electrons. The TOF is discussed in section 3.4.3 on page 37, a time resolution of 1 to 5 nanoseconds is probably the best that can be achieved (depending on the opening angle that is accepted), so a time resolution of the detectors in the 0.2 to 1 nanosecond range should be good enough.

2. From system requirements to component requirements

Vacuum compatibility

Both detectors must be ultra high vacuum compatible, 10^{-7} Pa. This means that out gassing should be low, and that a bake-out to at least 100°C (preferably 200°C) should be possible.

2.3.1 Energy loss detector

Energy of incoming electrons

The energy of the incoming electrons is the primary electron energy minus the energy loss, so the detector should handle 95 to 100 keV electrons.

Number of channels

The maximum useful number of channels for the energy loss detector is given by the energy range of interest divided by the energy resolution. The best energy resolution that can be obtained is given by the energy spread in the electron source (providing no energy filter is used), with the Schottky field emission gun this is in the order of 0.6 eV. An indication of the energy range of interest can be obtained by studying standard energy loss spectra⁶: all the major energy loss peaks of all elements (up to uranium) fall in the 0 to 3.5 keV range, leading to a maximum of 6000 channels of 0.6 eV width.

In practice a worse resolution (1 to 5 eV) is sufficient to distinguish the relevant peaks in energy loss spectra, and at any one time one is only interested in a smaller energy range, around one of the energy loss peaks. The width of most features is smaller than 20 eV, and practically all features are smaller than 200 eV, so about 200 channels of 1 eV width should suffice.

Maximum count rate

This value depends on the primary beam current. In the example of section 2.2.1 (*maximum spot current*) we assumed a specimen with a thickness equal to the inelastic mean free path. This means that $1/e$ of the electrons has not lost any energy, or that 63% has lost some energy. We also found that the current where the true-over-false ratio equals one is 0.16 nA, assuming this value we have 10^9 electrons arriving at the spectrometer per second, of which $4 \cdot 10^8$ fall in the zero-loss peak. The detector does not have to be able to handle this zero-loss peak (although being able to measure its position is important for alignment purposes, as well as for drift correction if this can be done during measurements). Assuming that the $6 \cdot 10^8$ electrons per second that have lost some energy fall in a flat energy spectrum from 0 to 2 keV, and that we use a 1 eV energy resolution, we would have $3 \cdot 10^5$ electrons per channel per second. In peaks of the spectra much higher values can occur, but in many other areas the rates will be lower. As a value to aim for 10^5 electrons per channel per second seems reasonable.

Because a peak will only occupy several channels, the count rate over the whole detector does not have to be the number of channels times the maximum count rate per channel, taking 10% of this value we get 10^6 events per detector per second.

2.3.2 Auger electron detector

Energy of incoming electrons

The energy with which the Auger electrons enter the detector depends on the pass energy of the

spectrometer, and this energy is between 55 and 550 eV for 0.1 to 1 eV resolution.

Number of channels

The maximum useful number of channels depends on what we wish to see:

Looking at standard Auger spectra⁷ we can see that for Auger peak identification a resolution of about 1 eV is enough, and as most relevant Auger peaks fall in the 0 to 2 keV range about 2500 channels is the maximum that could be useful. If we wish to look at a specific feature about 100 to 300 channels is enough, but if we wish to study several peaks at the same time a much larger value may be required.

If we wish to see details of the band structure (to look at the density of states) we need about 0.1 eV resolution, but over a much smaller energy range (about 10 eV), requiring only about 100 channels.

Maximum count rate

We follow the same estimation as for the energy loss detector: Assuming that the $6 \cdot 10^8$ electrons per second that have lost some energy all lead to the production of one secondary or Auger electron in the 0 to 2 keV energy range, and if we assume a flat energy spectrum at which we look with 1 eV resolution, we get $3 \cdot 10^5$ electrons per channel per second.

On the one hand this is an over-estimation, because some of the energy losses will result in X-rays rather than Auger electrons, some will result in energies larger than 2 keV, and finally most counts will fall in the low energy (secondary electron) range, so outside this range the count rate will be less. On the other hand this is an under-estimation, because, as just mentioned, the count rate in the low energy range can be much higher, and one energy loss event can lead to multiple secondary electrons. All in all a maximum count rate of 10^5 electrons per channel per second should suffice in most cases.

This maximum count rate will only occur in a peak in a few channels, again assuming that the count rate in most channels is only 10% of the maximum, we can see that the detector as a whole should be able to handle 10^6 events per second.

Spatial resolution

There is a trade-off between spectrometer energy resolution and transmission, and given the energy resolution there is an optimum setting for the entrance slit width and the accepted opening angle. These last two parameters determine the spatial width of an energy channel. The total number of (parallel) channels is also a parameter in the optimization, and is given by the exit slit width (available space) divided by the width of one channel.

When the energy spectrometer is operated in optimum mode for a parallel detector, we can have about 50 channels over a width of 25 mm, leading to 0.5 mm wide channels. The useful number of channels (resolution) can be somewhat higher (at the cost of transmission), to prevent a loss of resolution due to the detector in this case a spatial resolution of 0.25 mm is recommended.

2.4 Requirements on the data acquisition system

Having optics that allow a high illumination current and efficient signal collection, and having efficient detectors, we of course also need a data acquisition system that matches the above. This is again a region of overlap: the data acquisition system strongly depends on the type of detectors used. It turns out that only true multi channel detectors (without position encoding) can handle the count rate requirements, we have chosen to use detectors consisting of micro channel plates (MCPs), followed by multi-strip anodes (MSAs) for both detectors. For such detectors pre-amplifiers and discriminators are needed that match the detector output and that can handle the count rates. Because of the large numbers involved (one such set for each of 288 channels) this is not trivial.

Time resolution

The data acquisition system must be able to detect coincidences with at least 1 ns time resolution, with a window position and size that depends on the Auger electron energy (channel number) for the TOF variation correction.

Count rates

Apart from the count rates that come from the detectors (10^5 per channel per second, 10^6 total per detector per second, see the previous sections) the rate of coincidence events that have to be processed is also important, as such events take longer to process. The problem is that this rate strongly depends on the specimen and the energy ranges that are analyzed by the detectors. Assuming that the highest coincidence rates occur when we have a peak in the energy loss spectrum in coincidence with a peak in the Auger spectrum, and if we assume a combined collection and detection efficiency of 10%, then (using the previous estimate of 10^5 electrons per second per channel in the peaks, and peaks of a few channels wide) we can expect several times 10^4 coincidences per second. In many cases the coincidence rates are however probably lower than this value.

2.5 Requirements on the microscope control system

The microscope control system has to provide two interfaces via which the microscope can be controlled. The first is the user interface, which allows the operator to control the microscope. The second is the remote control interface, which is used by the data acquisition computer to change the selected energies and to scan the spot over the specimen.

The user interface should be easy to operate in the dark. It should preferably also be easy to learn and should minimize the work for the user. Minimizing the work means that it is possible to save the settings of the microscope so that they can be reused. It also means that the operator is presented with controls that control settings from the user's point of view, even if this means changing several settings in the microscope at once.

The remote control interface is necessary because the microscope and the data acquisition system are controlled by separate computers (following the philosophy to split the microscope into

independent parts when possible). This interface must provide a platform and operating system independent interface, and must allow the data acquisition system to make position and energy scans.

Illumination system control requirements

The illumination system user interface must provide a means to vary the spot size, the illumination angle and position, the current, and to perform the alignments. The illumination system remote control interface only needs to provide a means to move the spot over the specimen, so that a line or two-dimensional scan over an area of the specimen can be made. It is also necessary to be able to read-out the spot position, so that it is possible to move the spot relative to a certain starting position.

Energy loss analysis system control requirements

The energy loss analysis user interface should provide a means to set the energy loss (range) and the energy resolution, and to align the optics. The remote control interface only needs to allow reading and writing of the energy loss and the energy resolution.

Auger energy analysis system control requirements

The user interface must provide a means to set the Auger energy (range) and the resolution, and to align the optics. The remote control interface only needs to allow reading and writing of the Auger energy and the energy resolution.

2.6 References

1. A.J. Bleeker, *Optical and mechanical design for 1 nm resolution Auger spectroscopy in an Electron Microscope*, Ph.D. thesis, Delft University of Technology, The Netherlands (1991), unpublished.
2. A.J. Bleeker and P. Kruit, A condenser objective lens with asymmetric pole pieces to facilitate the extraction of secondary and Auger electrons, *Review of Scientific Instruments* **62** (1991), 350-356.
3. R.B. van Aken, *An achromatic 90° deflector for Auger electrons*, masters thesis Delft University of Technology, The Netherlands (1991), unpublished.
4. M.A.J. van der Stam, J.E. Barth and P. Kruit, Design of a multi mode transport lens with optimization program SOEM, *Proc. SPIE conference on Charged-Particle Optics*, W.B. Thompson, M. Sato, A.V. Crewe, Eds., SPIE - The International Society for Optical Engineering, Bellingham, **2014** (1993), 45-56.
5. J.S. Faber, *Possibilities for parallel detectors in coincidence experiments*, masters thesis Delft University of Technology (1991), unpublished.
6. Gatan Inc. and HREM Facility, *EELS Atlas*, Center for Solid State Science, Arizona State University, Tempe, AZ, USA (1983).
7. Jeol Ltd., *Handbook of Auger Electron Spectroscopy*, Jeol, 1-2 Musashino 3-chome Akishima, Tokyo, Japan (1982).

3 Optics

3.1 Introduction

The optics of the microscope can be divided into three subsystems: the illumination optics, the energy loss analysis (including the imaging) optics, and the Auger energy analysis optics. Each of these three will be treated in a separate section below. Although this chapter concentrates on the few parts of the optical system that still had to be designed, an overview of each complete subsystem is also given.

3.2 Illumination optics

We will start with a brief overview of the complete illumination system, followed by a section on optimum condenser lens settings.

3.2.1 Illumination optics overview

Figure 3.1 shows the complete illumination system. The brightness of the thermionic electron source ($B_r \approx 2 \cdot 10^4 \text{ Am}^{-2} \text{ sr}^{-1} \text{ V}^{-1}$, and a diameter of $1 \mu\text{m}$), with which the Philips EM430 microscope was originally equipped, is not high enough to achieve the desired current in the electron probe. To overcome this problem it has been replaced by the Schottky field emission source of a CM20 FEG ($B_r \approx 2 \cdot 10^7 \text{ Am}^{-2} \text{ sr}^{-1} \text{ V}^{-1}$, and a diameter of 30 nm). The condenser lenses and the scan coils are from the EM430. The pre-deflector, the Auger electron deflector, the parallelizer, and the objective lens have been designed and build in our group. The pre-deflector and the Auger electron deflector are housed in a separate (μ -metal) chamber normally not present in a transmission electron microscope (TEM).

The Auger electron deflector separates the Auger electrons from the primary electrons traveling in the opposite direction. When it is switched off the pre-deflector is also switched off and the beam passes straight through, as depicted in Fig. 3.1. When it is switched on the scan coils and pre-deflector are excited in such a way that the beam is deflected off-axis by the scan coils and is deflected back toward the axis by the pre-deflector, so that it intersects the axis in the Auger electron deflector. The effect of the Auger electron deflector is then to deflect the beam parallel to the axis again. In this way there is no first order effect of the Auger electron deflector on the illumination of the specimen.

We do however expect some sextupole aberrations from the Auger electron deflector, for this reason the 12-pole stigmator has been added near the objective lens. This stigmator can of course also produce a quadrupole effect to correct astigmatism.

The parallelizer coil extends the monopole-like field of the objective lens up to the magnetic aperture and serves to transport the Auger electrons to the deflector. Its effect on the primary beam is a very weak lens action.

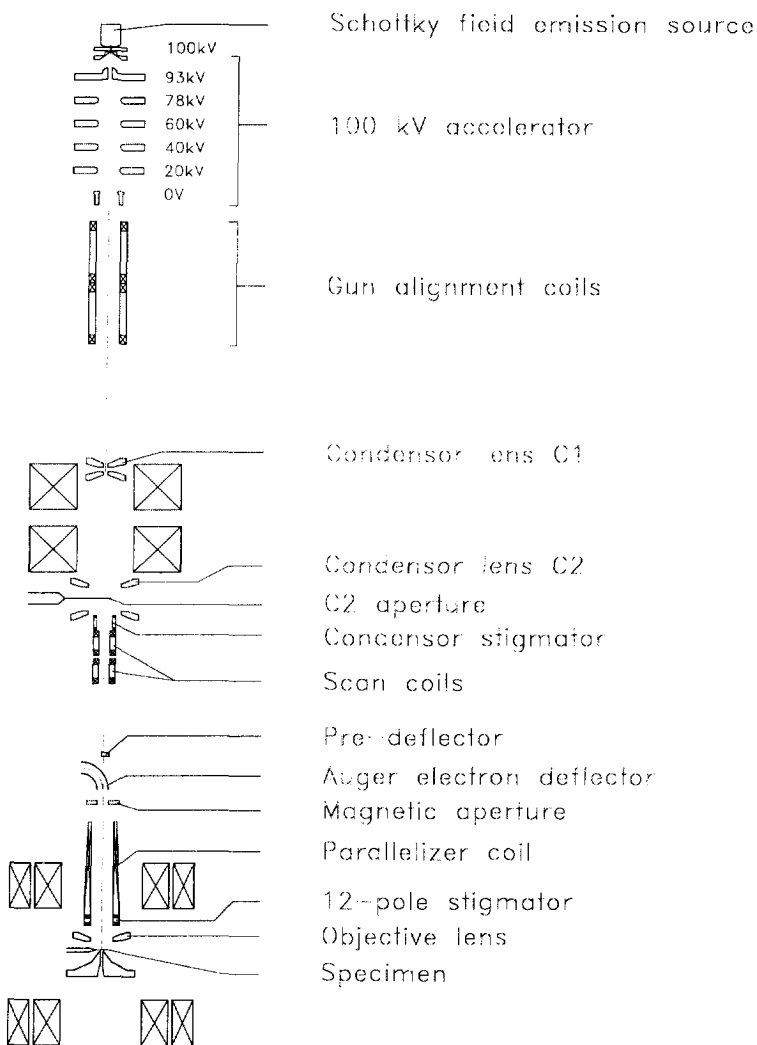


Figure 3.1 Overview of the illumination system. All parts are to scale, the distance between the source and the specimen is 812 mm.

3.2.2 Optimum condenser-side lens settings

The basic goal we have in optimizing the condenser lens settings is to get a small spot (1 nm diameter) on the specimen with a lot of current in it. It can be shown that the maximum current I_{probe} in a small spot d_{tot} is given by

$$I_{probe} = \frac{3}{16} \pi^2 d_{tot}^{8/3} C_s^{-2/3} B_r V_i, \tag{3.1}$$

where C_s is the coefficient of spherical aberration of the objective lens, B_r is the reduced brightness, and V_i is the acceleration voltage. The corresponding half opening angle α at the specimen is

$$\alpha = \sqrt[3]{\frac{d_{tot}}{C_s}}. \quad (3.2)$$

By filling in the parameters of our FEG ($B_r = 1.5 \cdot 10^7 \text{ A m}^{-2} \text{sr}^{-1} \text{V}^{-1}$, $V_i = 100 \text{ kV}$) and the spherical aberration of the objective lens ($C_s = 2.4 \text{ mm}$) we see that we can expect about 0.15 nA in a 1 nm diameter spot, with a half opening angle $\alpha = 7 \text{ mrad}$.

This is however under the assumption that the spherical aberration of the objective lens is dominant and that astigmatism can be reduced far enough - especially the Auger electron deflector is expected to cause a sextupole effect that may be a problem. In the following we will look at the degrees of freedom of the illumination system, and at how we should use these. We will start with the objective lens, then go to the gun lens and finish by looking at how C1 and C2 should 'interface' between these.

Objective lens and specimen height

The objective lens can best be viewed as two lenses (condenser and projector), of which the strengths are coupled. The condenser lens must image the crossover onto the specimen, which lies somewhere between the two lenses. The projector lens must make an image of the specimen on the selected area aperture. The position of the crossover (variable) and the position of the selected area aperture (fixed) together uniquely determine the specimen height (its position between the two lenses) and objective lens excitation. The crossover position depends on the excitations of the C1 and C2 condenser lenses; the best place for it is in the Auger electron deflector:

- In this position the effect of the Auger electron deflector aberrations is minimal.
- It is not too close to the 12-pole so this element can be used effectively to cancel the remaining effects of the Auger electron deflector.
- It results in a C2 aperture diameter of 160 μm , which is both reasonably below the maximum value of about 1 mm, and allows plenty of room to decrease the current by using a smaller aperture.

Gun lens setting

Next we will look at the gun lens setting. Because the FEG has a small virtual source size the total demagnification between this source and the specimen can become small, and the aberrations of the gun lens may become important.

To find the position and size of the image of the gun - as seen by C1 - we have simulated the gun lens and accelerator using the programs ELD¹ and EPROP². The extraction of electrons from a field emission tip cannot be simulated using these programs (due to the large ratio between radial and axial dimensions), so for this we have used a relation (Chmelik³) which gives the diameter of the virtual source as $d_{gun} = 2KR_{gun}\sqrt{U_t/U_e}$, where K is a geometrical coefficient ($K \approx 2$ for our FEG), R_{gun} is the radius of the tip ($R_{gun} = 0.82 \mu\text{m}$ for the tip installed at the moment of this writing), U_t is the thermal energy that the emitted electrons have tangent to the emission

3. Optics

surface, and U_e is the energy after extraction. There is still some debate what value should be used for U_p , the value which has been used here is $k_B T$ (the most probable energy), giving $U_i \approx 0.4$ eV. Chmelik gives the position of the virtual source as roughly 0.1 mm inside the tip (as the tip is heated it moves, so this position should not be critical anyway).

The two parameters that influence the image position and magnification are the extraction and gun lens potentials. The extraction voltage depends on the radius of the tip, and the way the tip has been mounted (how close it is to the extractor). This value is chosen so that optimum emission is obtained, and in almost all cases it will fall in the range between 2600 and 5800 V. The gun lens is at a potential halfway between the positive extraction potential and the negative gun lens power supply potential. This supply must produce at least -300 V for the suppressor to work, so the available range is -2200 (the maximum) to -300 V. Figure 3.2 shows the crossover position as a function of the gun lens power supply voltage for extraction voltages ranging between 2600 and 5800 V. Figure 3.3 shows the corresponding diameter of the image, including spherical and chromatic aberration of the gun lens. It has been assumed that the geometric spot size at the specimen is 1 nm, with a half opening angle of 7 mrad. From the (de)magnification required for the geometric spot size, the half opening angle at the crossover can be calculated. This angle has been used to calculate the diameters of the aberration disks.

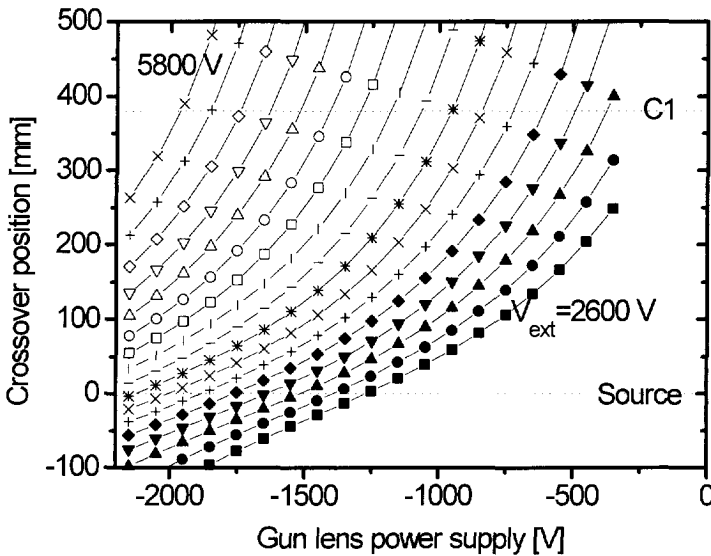


Figure 3.2 Position of the first image of the source (crossover) as a function of the gun lens power supply voltage. The source is at $z=0$, C1 is at $z=380$ (horizontal lines). Each curve corresponds to a certain extraction voltage, the curves are 200 V apart, the lower right curve is for 2600 V and the upper left curve is for 5800 V.

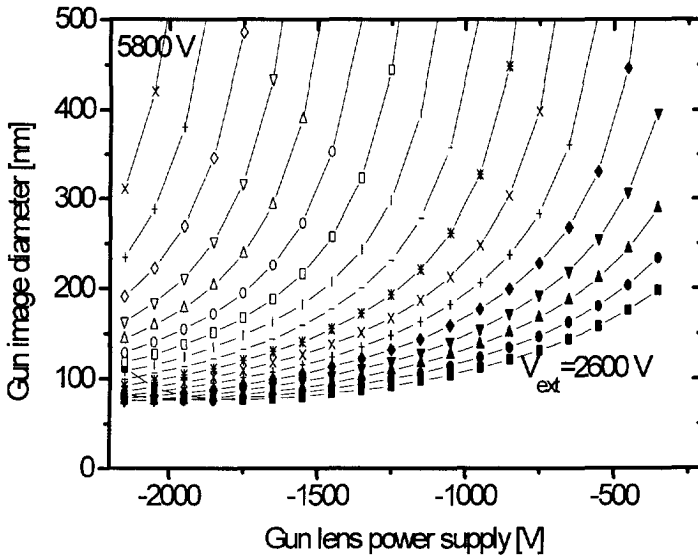


Figure 3.3 Total diameter of the first crossover as a function of the gun lens power supply voltage. The diameter has been calculated by assuming a 1 nm spot on the specimen with a 7 mrad half opening angle, and by adding the squares of the geometrical, the spherical and the chromatic spot contributions. Each curve corresponds to a certain extraction voltage, the curves are 200 V apart, the lower left curve corresponds to 2600 V and the upper right curve corresponds to 5800 V.

What we can learn from Figs. 3.2 and 3.3 is the following. First of all we do not want an image near C1, so in Fig. 3.2 we should stay away from (below) the horizontal line at $z = 380$, preferably below $z = 300$ or thereabouts. Secondly we would like a situation that can be obtained with any tip - the required extraction voltage varies from tip to tip - which means that we should also not go below $z \approx 100$ because this region is inaccessible with a blunt tip (high extraction voltage).

Looking at Fig. 3.3 we can see this even more clearly: for high extraction voltages the image lies in infinity if the gun lens setting is too low, which manifests itself in the crossover diameter also going to infinity. The lines in the upper left of Fig. 3.3 correspond to images flipping from +infinity to -infinity, and coming toward the tip again from -infinity.

A final point is that to minimize the Coulomb interactions in the gun lens it is best to decelerate the electrons as little as possible, from this point of view gun lens power supply voltages between -450 and -350 V are best.

Condenser lenses

The condenser lenses must fulfill two demands: the gun image made by the gun lens must in turn be imaged in the Auger electron deflector, and secondly it must be (de)magnified to 14 nm diameter. They have been modeled⁴ as thin lenses with focal length f given by $f = 0.897 f_{\min} / i \sin(2.03 i)$, where $f_{\min} = 0.5 \sqrt{(S^2 + 0.45 D^2)}$ is the minimum focal length (S is the

3. Optics

lens gap and D is the bore) and where $i = NI/NI_0$ is the relative excitation (N is the number of coil windings, I is the current through the coil, and $NI_0 = 13.5\sqrt{V^*}$, is the excitation necessary for f_{min} where $V^* = V(1 + 10^{-6}V)$ is the relativistic acceleration voltage ($V^* = 110$ kV). The characteristics of C1 and C2 are summarized in Table 3.1:

	D [mm]	S [mm]	f_{min} [mm]	NI_0	N
C1	4.0	2.5	1.9	4307	1792
C2	30	26	16	4440	1792

Table 3.1 Characteristics of the condenser lenses C1 and C2.

If we choose C1 and C2 so that the (de)magnification of the geometric image from Fig. 3.3 results in a 14 nm geometric image in the Auger electron deflector, and then take into account the aberrations of the gun lens, C1, and C2, we can compare the total spot size with the desired 14 nm. Figure 3.4 displays the total diameter in the Auger electron deflector. It can be seen that for gun lens power supply settings between -1200 V and 0 V, it is possible to stay close to the 14 nm geometric spot for all extraction voltages. The corresponding excitations of C1 and C2 are given in Fig. 3.5 and Fig. 3.6, respectively.

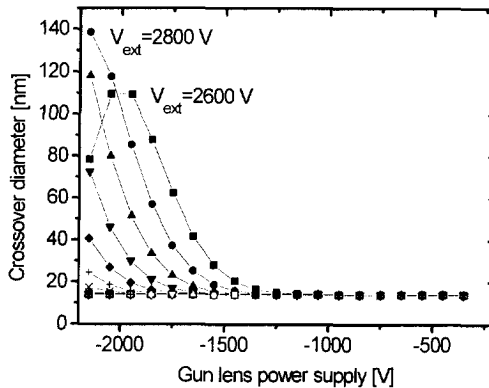


Figure 3.4 Total diameter of the crossover in the Auger electron deflector as a function of the gun lens power supply voltage. The curves correspond to extraction voltages 200 V apart, from 2600 V to 5800 V. It can be seen that for most extraction voltages the total diameter is close to the geometric size of 14 nm, so that the aberrations are neglectable. For gun lens settings above 1200 V this is even always so.

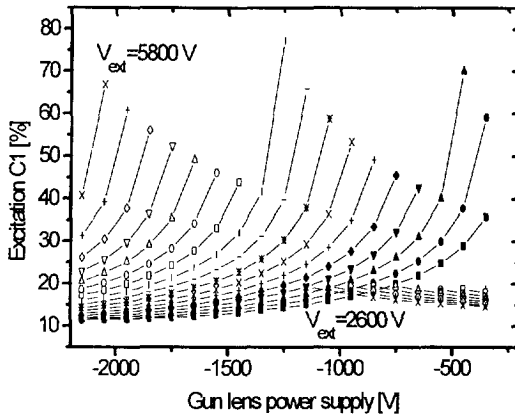


Figure 3.5 Relative excitation of C1 necessary for a 14 nm diameter crossover in the Auger electron deflector, as a function of the gun lens power supply voltage, for extraction potentials of 2600 to 5800 V, with 200 eV increments.

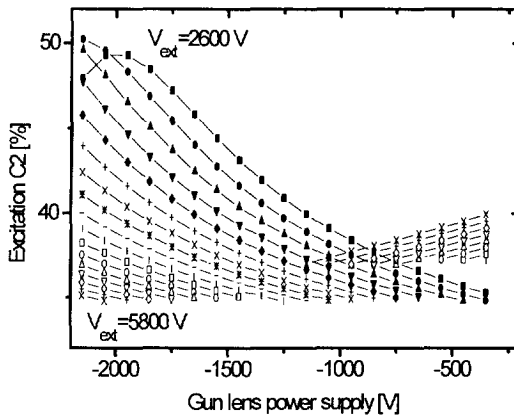


Figure 3.6 Relative excitation of C2 necessary for a 14 nm diameter crossover in the Auger electron deflector, as a function of the gun lens power supply voltage, for extraction potentials of 2600 to 5800 V, with 200 eV increments. The lines at the right are caused by switching to a mode where C1 uses a virtual rather than a real object. That this happens can best be seen in Fig. 3.2, which shows the position of the image made by the electrostatic gun lens, and where the position of C1 has been shown with a horizontal line.

Conclusions

The best position for the last crossover before the objective lens is in the Auger electron deflector. To obtain a 1 nm diameter spot on the specimen we need a 14 nm spot in this last crossover, in Fig. 3.4 we see that this is always possible for gun lens settings between -1200 and -300 V. In Figs. 3.5 and 3.6 we can find the corresponding c1 and C2 excitations.

The objective lens setting and specimen height are fully determined by the need to have a crossover in the Auger electron deflector and the need to have a specimen image in the selected area aperture. Once the crossover lies in the correct position we can determine these values experimentally.

3.3 Energy loss analysis optics

The energy loss analysis optics consists of the EM430 imaging optics, a Gatan 607 spectrometer, and the post-spectrometer (enlargement) optics. This section will concentrate on the post-spectrometer optics, which are necessary to convert between the spectrometer output and the detector input.

3.3.1 Energy loss analysis optics overview

The objective lens (projector side) and the imaging optics of the EM430 TEM efficiently collect the energy loss electrons (which scatter over relatively small angles). A Gatan 607 energy loss spectrometer provides the energy dispersion, however, because the dimensions of the energy spectrum after the spectrometer are too small for the detector, a post-spectrometer system is needed to enlarge it. Fig. 3.7 shows the complete optics of the energy loss analysis system.

3.3.2 Post-spectrometer optics requirements

The demands on the post-spectrometer optics follow from the spectrometer and detector characteristics sketched in Chap. 2. The energy spectrum after the spectrometer consists of $\phi 2 \mu\text{m}$ spots, which are displaced $2 \mu\text{m eV}^{-1}$. Each energy channel (of 1 eV width, i.e., a $2 \mu\text{m}$ spot) must be 'imaged' onto one of the two hundred $250 \mu\text{m} \times 50 \text{mm}$ rectangular strips of the detector, where 'imaged' is between quotes to indicate that a true image is not necessary, the enlargement (within an energy channel) may also be achieved by defocusing. We can see that a magnification of $250 \mu\text{m} / 2 \mu\text{m} = 125\times$ is necessary in the dispersive direction, and that in the non-dispersive direction a magnification (or defocus) of $50 \text{mm} / 2 \mu\text{m} = 25000\times$ is necessary. Further demands on the system are a variable magnification in the dispersive and in the non-dispersive direction, a focus in dispersive direction, and that the magnification in the dispersive direction can be varied without influencing the non-dispersive direction.

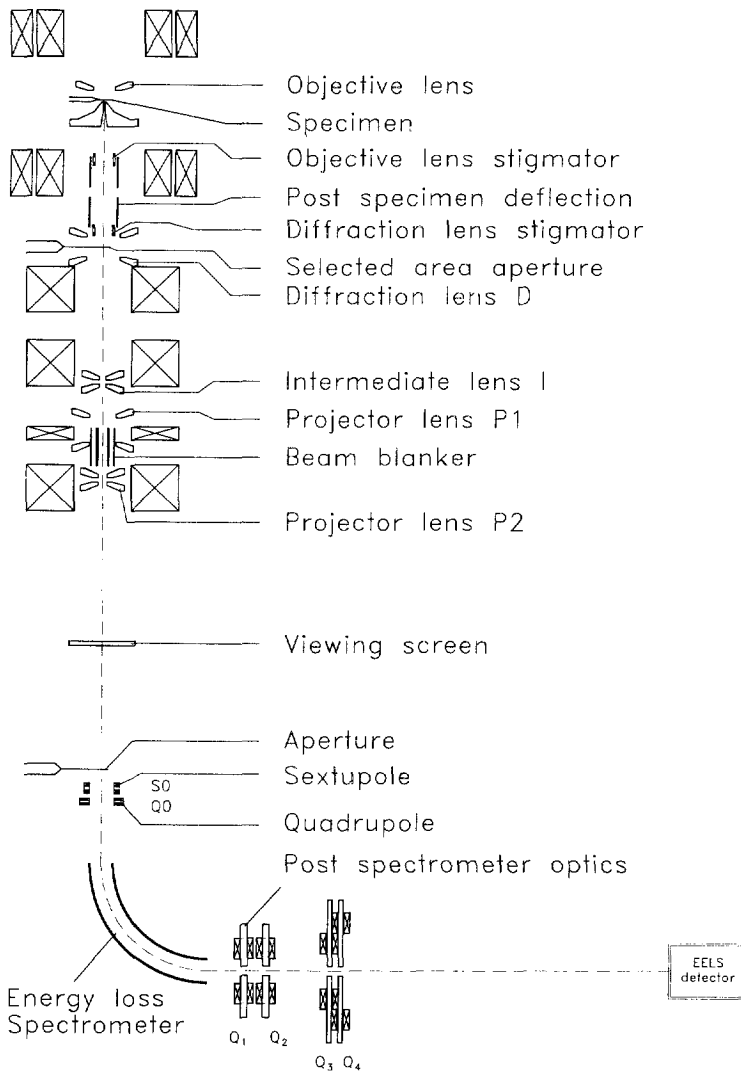


Figure 3.7 Energy loss analysis optics. The four post-specimen lenses (D, I, P1, and P2) transport the electrons to the spectrometer, which energy disperses them. The four quadrupoles (Q₁ to Q₄) of the post-spectrometer system enlarge this spectrum so that it matches the detector.

3. Optics

3.3.3 Post-spectrometer optics design

From designs described in literature^{3,6} and from the degrees of freedom required to fulfill all the demands we have come up with a design consisting of four magnetic quadrupoles (Q_1 to Q_4). The reason we use quadrupoles and not round magnetic lenses is that with the latter the total system would have been much longer. The reason that we use four quadrupoles is that this is the minimum number required to fulfill all demands.

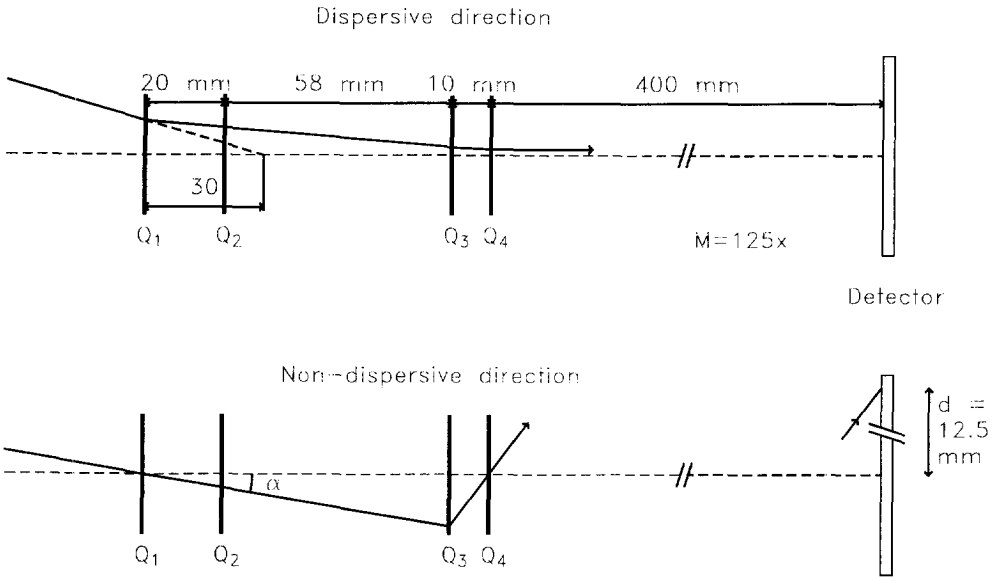


Figure 3.8 Optical design of the post-spectrometer optics. In the dispersive direction (top) the energy spectrum falls 30 mm inside the system. This virtual source for Q_1 is mainly enlarged by Q_1 and Q_4 , providing a magnification of around 125 times. In the non dispersive direction (bottom) the energy spectrum falls in Q_1 and is imaged in Q_4 by Q_2 and Q_3 . In this way Q_1 and Q_4 do not influence the non dispersive direction. Q_2 and Q_3 can also provide a defocus width of 25 mm for the whole range of half opening angle α .

The system works as follows (see Fig. 3.8): the spectrometer is normally double focusing, producing (energy dispersed) images on the entrance slit of the serial detector. By changing the setting of the quadrupole at the entrance of the spectrometer (Q_0) it is possible to separate the images in the dispersive and in the non-dispersive directions. If an image falls in the center of a quadrupole it will not 'feel' that quadrupole, we use this by having the image in the non-dispersive direction fall in the center of Q_1 , and by letting Q_2 and Q_3 image Q_1 (and the non-dispersive image) onto Q_4 we can vary Q_1 and Q_4 without influencing the image in the non-dispersive direction. The image in the dispersive direction falls further inside the post-spectrometer system (it is a virtual image for Q_1 and Q_2), and we can use Q_1 and Q_4 to change the magnification in this direction.

Quadrupoles Q_2 and Q_3 also set the defocus width in the non-dispersive direction. This defocus width also depends on the opening angle which is selected by the spectrometer entrance aperture, so if this aperture is changed we need to readjust Q_2 and Q_3 . Because we have two quadrupoles we can do this in such a way that Q_1 remains imaged on Q_4 . Because a change in Q_2 and Q_3 will also influence the dispersive direction we first set the defocus-width in the non-dispersive direction with Q_2 and Q_3 (and imaging Q_1 on Q_4), and then we can vary the magnification in the dispersive direction with Q_4 , and focus the energy spectrum with Q_1 .

3.3.4 Post-spectrometer mechanics

The optical design calls for four quadrupoles. The first two and the last two quadrupoles must be quite close together (20 mm and 10 mm, respectively) which has led to a design where these pairs are in a single housing. A spacer between these two housings sets the separation between Q_2 and Q_3 (58 mm). With the use of two dowels the spacer also defines the rotation between Q_1/Q_2 and Q_3/Q_4 , and the spacer itself can be rotated around the vacuum liner tube by a spring/adjustment screw assembly, providing rotation alignment of the whole system with respect to the spectrometer.

Because the quadrupoles Q_3 and Q_4 have to be close together there is not enough space to place the coils at the same height, instead they have been staggered as shown in Fig. 3.9. Also visible in this figure is the extra quadrupole that provides the rotation correction of Q_3 , the thinned ends of the cores of this quadrupole, and the NiFe ring that completes the magnetic circuit on the outside.

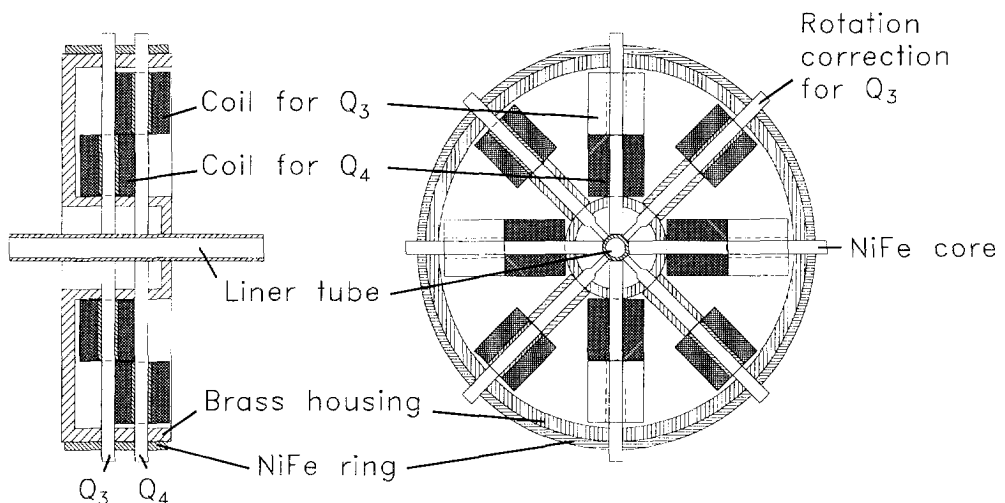


Figure 3.9 Housing of Q_3 and Q_4 . Because Q_3 and Q_4 are so close together the coils around the NiFe cores have been staggered as shown. The extra quadrupole rotated over 45° provides the rotation correction for Q_3 . Note that it does not need to be as strong as the main quadrupole, and to save space its cores have been thinned the end.

3. Optics

See Fig. 4.8 on page 76 for an overview of the post spectrometer optics and the energy loss detector. Chapter 4 describes the quadrupole power supplies and control system.

Acknowledgment: this work was done in close collaboration with Harold Brink, who obtained his masters thesis⁷ on this design.

3.4 Auger energy analysis optics

The Auger energy analysis optics must collect the Auger electrons that leave the specimen, transport them to the detector, and energy disperse them. This section will concentrate on two aspects: the (transport) lens which transports the electrons from the Auger electron deflector to the spectrometer, and the time-of-flight (from specimen to detector) variations.

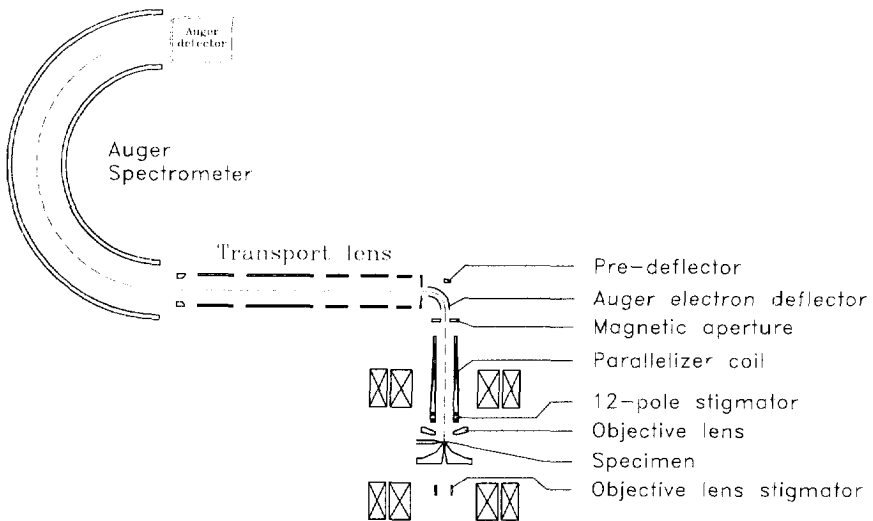


Figure 3.10 Auger electron analysis optics. The asymmetric pole pieces of the objective lens, together with the parallelizer coil produce a monopole field which effectively collects the electrons coming from the sample. The magnetic aperture cuts off the last part of the monopole field, after which the electrons are separated from the primary beam by the Auger electron deflector. A seven electrode electrostatic (transport) lens transports the electron to the spectrometer.

3.4.1 Auger energy analysis optics overview

The Auger energy analysis optics consists of (see Fig. 3.10): the objective lens, which due to its asymmetric pole pieces and 'floating' upper pole piece produces a monopole-like field ($B(z) \sim 1/z^2$). This field effectively collects and parallelizes the Auger electrons⁸. The parallelizer coil extends the monopole field up to the magnetic aperture, which abruptly terminates the

remaining field, so the electrons enter a field-free region. The Auger electron deflector separates the Auger electrons from the primary electrons traveling in opposite direction. This deflector is achromatic, i.e., it deflects a whole range of Auger electrons over 90° , which has the advantage that an energy range can be analyzed without the need to change the deflector settings, and without risk of moving the primary beam (and the spot on the sample). The seven electrode electrostatic lens transports the electrons to the spectrometer, and adapts their energy and opening angle to the spectrometer (so that the central energy of interest enters the spectrometer at the pass-energy, and so that the transmission of the spectrometer is optimal). The 180° electrostatic hemispherical spectrometer provides a dispersion which, depending on the desired resolution, varies between 5 mm eV^{-1} (0.1 eV resolution) and 0.5 mm eV^{-1} (1 eV resolution).

3.4.2 Transport optics

The design of the transport optics system has been done by van der Stam⁹, who has optimized the seven electrode electrostatic transport lens for several modes of operation: for each combination of entrance energy and energy resolution the lens needs to perform differently.

The lens images the electrons that come out of the Auger electron deflector on the spectrometer entrance slit and accelerates or decelerates them so that they enter the spectrometer with an energy equal to the pass energy for the desired energy resolution. It is an afocal system to minimize the maximum opening angle that enters the spectrometer. The magnification is such that the transmission through the spectrometer is optimal for a 48 energy channel parallel detector (so our 96 channel detector over-samples the spectrum). The simulations have also resulted in a table with optimum electron energies at each lens electrode for 35 different entrance energy and resolution pairs, this table is used to automatically set the lens voltages (see section 6.6.4 on page 62, and Table B.2 on page 133).

3.4.3 Time-of-flight variations

The time-of-flight (TOF) of Auger electrons traveling from the specimen to the detector is an important aspect in the coincidence experiment, because the position and width of the peak in the time spectrum depend on it. Especially variations in TOF will affect the peak width and can be a problem because the time window has to so be wide that the whole peak falls in it. The variations in the TOF are caused by different energy electrons traveling at different speeds, and by different starting angles leading to different trajectory lengths. Because we can set a different time window for each energy, the energy dependency of the TOF is not so important, but the TOF variations due to different starting angles may be a serious problem.

Energy loss electron TOF

Although we are talking about the Auger electrons here, the energy loss electrons of course also contribute to the coincidence peak width, however a simple calculation will show that their contribution can be neglected (due to their much higher energies).

The TOF of energy loss electrons with energies in the 95 to 100 keV range is 7.79 to 7.65 ns. The variation of 140 ps is so small that we can neglect the energy loss effect on the TOF.

3. Optics

For small half opening angles α the velocity v_z in z-direction (along the optical axis) will roughly be equal to $v_z = v(1 - \alpha^2)$, where v is the total velocity. The increase in TOF is then proportional to $1/(1 - \alpha^2)$, for the energy loss electrons the maximum opening angle we can accept is 0.1 rad, the corresponding increase in TOF is 1% of 7.7 ns, or 77 ps, which is also negligible small.

Auger electron TOF

The Auger electrons pass four elements: the parallelizer, the Auger electron deflector, the transport lens, and the spectrometer. The TOF for each element has been simulated using analytical formulas, by adding the TOF for all four elements the total TOF can be found.

Parallelizer TOF

The motion of electrons in a monopole field has been described extensively by Kruit and Lenc¹⁰. Basically the electrons spiral over the surface of a cone, with the apex of the cone in the (virtual) magnetic monopole, see Fig. 3.11.

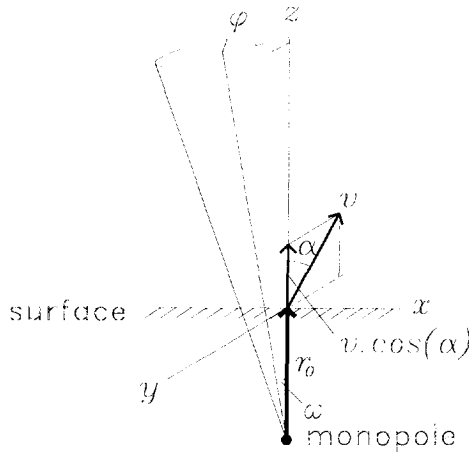


Figure 3.11 Coordinate systems used to describe the motion of an electron in a monopole field. The cartesian (x, y, z) system has its z-axis perpendicular to the specimen surface. The spherical coordinate system (r, θ, ϕ) has its origin in the magnetic monopole and is tangent to the z-axis. The cone is described by $\theta = \omega$. The electrons leave the sample in $(x=y=z=0)$ and $(r=r_0, \theta=\omega, \phi_d)$, under an angle α in the yz -plane.

They show that the motion can be described by (in the spherical coordinate system)

$$r(t) = \sqrt{v^2 t^2 + 2r_0 v t \cos(\alpha_0) + r_0^2} \quad (3.3a)$$

$$\theta = \omega = \sin^{-1} \left(\frac{\sin(\alpha_0)}{\sqrt{\sin^2(\alpha_0) + \left(\frac{e B_0 r_0}{m v} \right)^2}} \right) \quad (3.3b)$$

$$\phi(t) = \phi_0 + \frac{1}{\sin(\omega)} \left[\alpha_0 - \tan^{-1} \left(\frac{r_0 \sin(\alpha_0)}{v t + r_0 \cos(\alpha_0)} \right) \right], \quad (3.3c)$$

where Eq. 3.3b has been rewritten for our simplified case where the electron starts on the z -axis ($x_0 = 0, y_0 = 0, z_0 = r_0$).

We are interested in the time t at which the electron passes through the magnetic aperture at $z = z_f$, this is approximately when $r(t) = r_0 + z_f$ (assuming ω is small), giving

$$t = \frac{\sqrt{r_0^2 \cos^2(\alpha_0) + 2r_0 z_f + z_f^2} - r_0 \cos(\alpha_0)}{v} \quad (3.4)$$

as the TOF. We can find the position r_0 of the virtual monopole with respect to the sample from the initial field B_0 at the sample and the final field B_f in the magnetic aperture at $z = z_f$ via the relations $B_0 = B(r_0) = g/r_0^2$ and $B_f = B(r_0 + z_f) = g/(r_0 + z_f)^2$, giving

$$r_0 = \frac{z_f(B_f + \sqrt{B_f B_0})}{B_0 - B_f} \quad (3.5)$$

(the monopole strength g falls out). For the Auger microscope $B_0 = 1$ Tesla, $B_f = 0.001$ Tesla and $z_f = 132$ mm, so $r_0 = 4.3$ mm. The velocity v follows from the energy U with which the electrons leave the sample: $v = \sqrt{2U/m}$, where m is the electron mass. In Fig. 3.12 the TOF variation as a function of α is shown for energies in the 1 to 100 eV range (the specimen is at 0V, so there is no acceleration). Note that even for a 1 keV electron leaving the sample parallel to the surface ($\alpha_0 = \pi/2$) the assumption that $\omega = 0.6$ mrad is small is valid. The inset shows the total TOF as a function of energy for electrons starting parallel to the axis (zero angle).

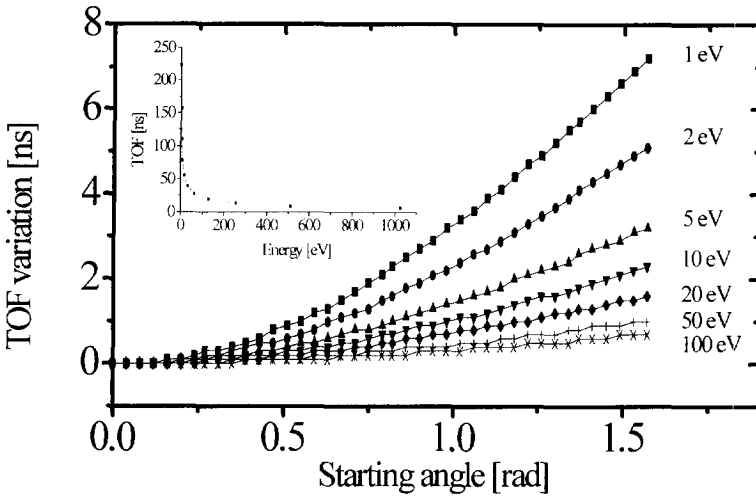


Figure 3.12 Variations in parallelizer time-of-flight as a function of the angle with which the electrons leave the specimen, for energies of 1 to 100 eV. The specimen is at 0 V (no acceleration). The inset shows the total TOF as a function of electron energy.

Figure 3.13 shows the same, but then for the case where the specimen is at -240 V. In the first section (1 mm), where the electrons are shielded by the specimen holder, no acceleration is assumed. The next section (8 mm length) has been divided into 20 slices, in each slice the electrons receive some extra energy (and their angle is changed accordingly), after which the parallelization (without accelerating field) is calculated. In the final section (123 mm length) the electrons travel at their final velocity and there is no more acceleration.

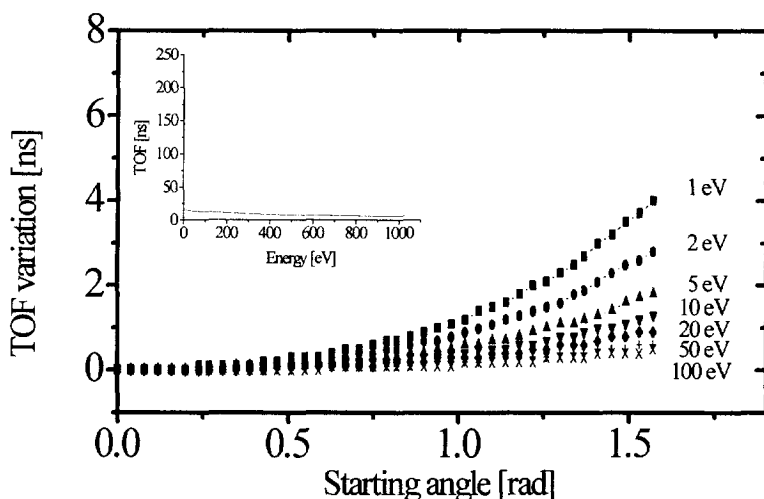


Figure 3.13 Variations in the parallelizer TOF as a function of starting angle and starting energy (inset). The specimen is at -240 V . The effect of the acceleration is taken into account by alternatively calculating parallelization without accelerating field, and adding extra energy (and calculating the change in angle).

Auger electron deflector TOF

The minimum energy with which the electrons pass through the Auger electron deflector is 300 eV (0 eV secondaries accelerated by 240 eV at the specimen, and by a further 60 eV just before the deflector). For this energy the TOF through the 20 mm radius deflector is 3 ns .

A worst case value for the TOF variations as a function of the half opening angle α can be found by calculating the TOF variations for an electrostatic deflector of the same dimensions. Because, contrary to normal electrostatic deflectors, the electrons are accelerated as the radius of their trajectory increases, the extra trajectory length is (partly) compensated by extra velocity, so the variations will be smaller than in the case of an electrostatic deflector. Using the paper by Imhof *et al.*¹¹, and taking half the variation in time (we only have a 90° deflector instead of 180° deflector) we find that the TOF variations are less than 0.2 ns .

Transport lens TOF

The TOF through the transport lens depends on the Auger energy of interest and the energy resolution of the spectrometer. The worst case is when the entrance, intermediate, and exit energies are low; looking at the results of the simulations we can see that 300 eV entrance energy and 54 eV exit energy is the worst case. The transit time for the axis trajectory has been estimated by calculating the velocity in each lens segment and assuming a linear acceleration/deceleration between the elements, for the case above this results in a TOF of 23.5 ns .

3. Optics

The effect of a half opening angle α will in first order be a decrease of the forward velocity via $v_z = v(1 - \alpha^2)$, for $\alpha = 0.1$ rad this is only a 1% decrease, so a 0.2 ns increase in the TOF.

Spectrometer TOF

For the TOF variation ΔT in a 180° hemispherical electrostatic energy spectrometer, as a function of entrance slit width d and entrance half opening angle α , Imhof *et al.*¹¹ give the following formulas

$$\begin{aligned}\Delta T(d)/T_0 &= (3/2r_0)d \\ \Delta T(\alpha)/T_0 &= (8/\pi)\alpha,\end{aligned}\tag{3.6}$$

where $T_0 = \pi r_0/v = \pi r_0/\sqrt{(2U/m)}$ is the time needed for the central trajectory, r_0 ($= 140$ mm) is the radius of the central trajectory, and v , U , and m are the electron velocity, energy, and mass, respectively.

When the transmission is optimized for a parallel detector with 48 energy channels, we have an entrance slit width $d = 0.43$ mm, an entrance half opening angle $\alpha = 50$ mrad, and the spectrometer pass energy U follows from the desired energy resolution ΔU as $U = 537.6 \Delta U$ (see van der Stam⁹). This gives $\Delta T(d)/T_0 = 4.6 \cdot 10^{-3}$ and $\Delta T(\alpha)/T_0 = 0.13$. Table 3.2 shows the TOF and the variations in the TOF for several energy resolutions:

ΔU	U	T_0	$\Delta T(d = 0.43 \text{ mm})$	$\Delta T(\alpha = 50 \text{ mrad})$
0.1 eV	53.8 eV	101 ns	0.46 ns	13 ns
0.2 eV	108 eV	72 ns	0.33 ns	9.2 ns
0.5 eV	269 eV	45 ns	0.21 ns	5.7 ns
0.8 eV	430 eV	36 ns	0.17 ns	4.6 ns
1.0 eV	538 eV	32 ns	0.15 ns	4.1 ns

Table 3.2 Electrostatic spectrometer central pass energy U , TOF T_0 , and TOF variation ΔT for several energy resolutions ΔU . Note that the entrance slit width d and the half opening angle α have been optimized for maximum transmission, assuming 48 energy channels.

Overall TOF

To get an impression of the total TOF effect we have simulated 10^4 electrons, with starting angles distributed over 2π steradian with a Lambert (cosine) distribution, with starting energies between 1 and 400 eV. The sample was assumed to be at -240 V, the parallelizer initial and final field were 1 T and 0.001 T, the Auger electron deflector was at +60 V and had 500 eV central energy, the spectrometer entrance slit was 0.43 mm and the energy resolution was 1 eV. At the magnetic aperture, the transport lens aperture, the spectrometer entrance aperture and the spectrometer exit aperture it was checked for each electron if it could go through, and if not that electron was not counted. The result of this simulation is shown in Fig. 3.14.

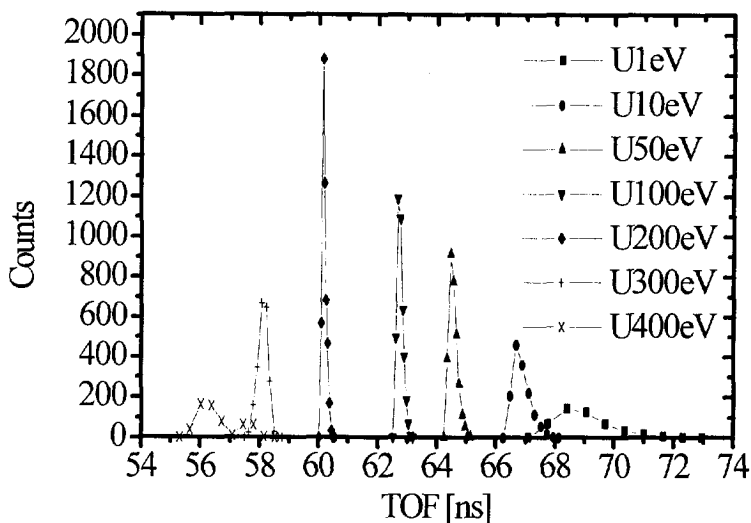


Figure 3.14 Simulated TOF for electrons with energies of 1 to 400 eV. For each energy 10^4 electrons have been simulated, starting with a Lambert distribution at the specimen, which was at -240 V. Low energy electrons have a TOF spread dominated by the parallelizer, high energy electrons have a TOF spread dominated by the spectrometer (because they enter the spectrometer with larger angles). The total TOF decreases with increasing energy.

TOF conclusions

The TOF is dominated by the spectrometer. It can be seen that the TOF variation due to the half opening angle is large, even for the highest energy resolution of 1 eV. This indicates that for coincidence experiments it will probably be necessary to decrease the half opening angle accepted by the spectrometer, at the cost of transmission (although this can partly be compensated by choosing a larger slit width). To obtain 1 ns resolution the opening angle will have to be decreased to about 12 mrad.

3.5 References

1. B. Lencova, Computation of electrostatic lenses and multipoles by the first order finite element method, *Nucl. Instr. Meth.* **A363** (1995), 190-197.
2. B. Lencova and M. Lenc, Computation of properties of electrostatic lenses, *Optik* **97**, 121-126.
3. J. Chmelik, private communication (1995).
4. T. Mulvey and M.J. Wallington, Electron lenses, *Report on Progress in Physics* **36** (1973), 347-421.

3. Optics

5. O.L. Krivanek, C.C. Ahn, and R.B. Keeney, Parallel detection electron spectrometer using quadrupole lenses, *Ultramicroscopy* **22** (1987), 103.
6. C.P. Scott, A.J. Craven, A quadrupole lens system for use in a parallel recording system for electron energy loss spectroscopy, *Ultramicroscopy* **28** (1989), 126-130.
7. H.A. Brink, *The Post-EELS Optics*, masters thesis Delft University of Technology, the Netherlands (1995), unpublished.
8. P. Kruit and J.A. Venables, High-spatial-resolution surface-sensitive electron spectroscopy using a magnetic parallelizer, *Ultramicroscopy* **25** (1988), 183-194.
9. M.A.J. van der Stam, J.E. Barth and P. Kruit, Design of a multi mode transport lens with optimization program SOEM. *Proc. SPIE conference on Charged-Particle Optics*, W.B. Thompson, M. Sato, A.V. Crewe, Eds., SPIE - The International Society for Optical Engineering, Bellingham, **2014** (1993), 45-56.
10. P. Kruit and M. Lenc, Optical properties of the magnetic monopole field applied to electron microscopy and spectroscopy, *Journal of Applied Physics*, **72** (1992) 4505-4513.
11. R.E. Imhof, A. Adams and G.C. King, Energy and time resolution of the 180° hemispherical electrostatic analyzer, *Journal of Physics E. Scientific Instruments*, **9** (1976), 138-142.

4 Microscope control system

4.1 Introduction

This chapter describes the microscope control system: the user interface (design), and the way it meets the demands from Chap. 2. The aim of the user interface is to enable an easy microscope control for both new and experienced users.

4.2 User interface

4.2.1 Necessity of computer control

A computerized interface offers so many advantages that, although even a complex instrument like the Auger microscope can in principle be operated without such an interface, it would be wasteful not to make use of these advantages. The main advantages that a computerized interface can provide are:

- 1) The provision of logical settings which influence several microscope settings at once. This reduces the number of controls a novice user has to learn, and it allows experienced users to operate the microscope more easily (faster). A good example is the Auger electron energy setting, which influences seven separate settings. As the relations between the settings are in software, it is also relatively easy to change them.
- 2) A reduction of the number of (re)alignments. Logical setting as described above need to be aligned once, from then on the computer maintains the alignment relation between the corresponding microscope settings.
- 3) Allowing the operator to save settings, making the microscope more forgiving to mistakes (novice users can play more easily, experienced users can make a back-up halfway during a complicated alignment).

For these reasons we have decided to computerize the microscope as much as can be done with relatively little effort, using computer controlled power supplies for all the new (not part of the original EM430) supplies, as well as replacing some of the old supplies - especially those which have to interact with other power supplies.

4.2.2 User interface

The user interface has been given a lot of thought: computer control in theory offers a flexible interface, but the user friendliness of the resulting interface depends strongly on the way this has been realized. Apart from the demands in section 2.3 (what the control system must be able to do) the wish for ease of use (how the control system fulfills the demands) leads to the following additional demands:

4. Microscope control system

- 1) The use of 'logical' knobs wherever applicable.
- 2) The use of alignments that, once performed correctly, are stored and enable the user to vary a wide range of settings without the need to realign.
- 603) The ability to operate the microscope in the dark, and having to look away from the microscope viewing screen as little as possible. This in turn implies several things:
 - a) It must be possible to find and operate the most often used controls by touch.
 - b) Because only a fairly limited number of controls can reliably be found by touch, additional controls will be needed that do need visual attention, but this attention must be minimal, and using the available light.
 - c) When looking away from the viewing screen, the operator must not be blinded.
- 4) The automation of standard tasks, such as an energy scan or the procedure to switch the microscope from standby to operate mode.

As described by Sanders and McCormick¹ there are many points to be taken into consideration during a human-machine interface design, rather than a trying to give an incomplete summation the reader is referred to this excellent book.

4.2.3 Philips CM series interface

The Philips CM series of microscopes has a computer-based user interface and it was a logical step to analyze this interface to obtain ideas for our interface.

The CM series of microscopes are operated using a menu structure, starting at a top-level menu with an overview of the main groups of settings sub-menus provide increasing detail. This has been implemented as a small computer monitor with several buttons just to the left and right of it. The buttons are used to go to another menu, or to select a setting to change. The function of the buttons changes, depending on where you are in the menu structure and is displayed next to the button. The middle of the monitor screen is used to display settings relevant to the current menu. Several rotary knobs (softknobs) are used to change settings, which setting a knob will change again depends on where you are in the menu structure.

The two pros of this system are: 1) that it is easy to learn (confusing detail is hidden deeper in the menu) and 2) the softknobs, which are ideal for the typical increase/decrease changes that have to be made. The three cons are: 1) that for experienced users it is slow to operate: it takes several button pushes to go from one sub-menu to another, 2) that the bright computer screen is needed to traverse the menu structure, deteriorating the adaption to the darkness, and 3) that here is no easy provision for entering alphanumerical input, like the name of a file to save/restore settings in.

4.2.4 Auger microscope user interface

The user interface we have come up with is the following (see Fig. 4.1). A large console with groups of push buttons replaces the computer monitor and push buttons used in the CM interface, softknobs in two boxes (on either side of the microscope column) are used to change selected settings manually, the computer monitor has been given a less prominent place (behind the operator), and finally a keyboard added next to the monitor completes the interface.

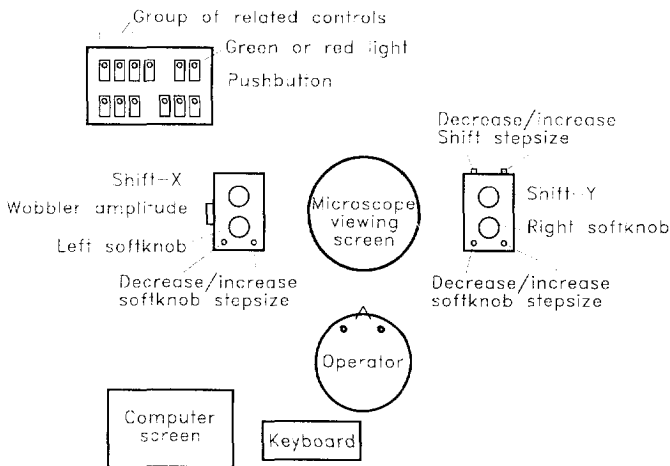


Figure 4.1 Top view of the Auger microscope user interface: a setting is selected by pushing a button, after which the rotary softknobs operate on that setting. The computer screen displays values relevant to the selected setting, and the current function of the softknobs.

The console with groups of push buttons is like all sub-menus spread out next to each other: the grouping provides order, but now every setting is available with one single push. Each push button is illuminated by a two-color light emitting diode (LED), which normally glows dim red. When the button is pushed, the LED switches to green, indicating what the currently active setting is. The operator of course still needs to know which button to push, he can learn this by reading the labels next to the button (difficult in the dark), but because in practice only a small subset of all available settings is needed most operators quickly learn which buttons in which groups they need. Because all buttons are always illuminated, the patterns of the groups can easily be seen in the dark.

The number of controls on the boxes containing the rotary knobs is so limited that they can be found and operated reliably by touch, and because the boxes can be placed anywhere on the console the operator can ensure that they are within easy reach. The boxes contain two rotary knobs each: the upper knobs are always shift-x (left hand) and shift-y (right hand), and the lower knobs are the softknobs: their function depends on the currently selected setting.

The step size of the softknobs can be varied logarithmically ($step = 2^n$, with $0 \leq n \leq 5$) using two small push buttons near each knob, the left button decreases, the right button increases the step size. In this way a large change can be made with a few turns using a large step size, while fine adjustments can be made using a small step size

During alignments it can be advantageous to continually vary a specific setting, modulating with a certain amplitude around the normal setting. Some misalignments can very easily be adjusted by minimizing the movement caused by such modulation. The modulator amplitude is an important factor in this, it must be large enough to see the effect of misalignment, but it must not be so larger that the image can no longer be recognized. This amplitude can be varied using a third rotary knob on the side of the left-hand box. It turned out in practice that the

4. Microscope control system

modulator amplitude required a third knob, rather than a separate (push button) setting, because it needs to be adjusted often during alignments. The modulator is activated automatically when a setting is selected that may require it, but by turning the amplitude down to zero it can be 'switched off' if it is not required.

For most work the computer monitor is no longer necessary, and it has been given a less prominent place behind the operator, where it cannot blind him, but where it can easily be inspected to check a setting. The information displayed is divided into several windows:

- One window always displays several important microscope settings: the primary electron energy, the energy of Auger electrons, the resolution with which these are analyzed, the central energy of the Auger deflector, the potential of the sample and the Auger deflector, the modulator amplitude, the beam shift position, and the shift step size.
- A second window displays the currently selected setting as well as the function of both softknobs, their value, the units in which the values are displayed, and the step sizes.
- A third window can be opened which displays 'debug' information, like for example the commands coming in via the serial interface.
- A line at the bottom of the screen provides a reminder of the most often needed key strokes, like those for saving and restoring settings and activating the (hypertext) help.

Finally a keyboard near the monitor provides an efficient way to save/restore settings, and to select special functions (which are used so rarely that they are not available using the push button interface).

4.3 Brief introduction to the P80 computer controlled power supply system

Transmission electron microscopes in general require very stable (within a ppm per minute) current supplies in the typical ranges of -100 to 100 mA (deflectors) and 0 to 10 A (lenses), and the Auger microscope is no exception. Commercial supplies meeting these requirements are hard to find, as well as being prohibitively expensive. The system used by the Philips CM series of electron microscopes fulfills our requirements and is available to us, and for this reason we have chosen to use this P80 system.

The P80 system (developed by Philips in 1980) is a modular system, consisting of various types of cards that are plugged into a crate which provides them with raw power supplies and a digital interface bus. This interface bus has 256 addresses. Each card typically occupies 4 to 16 addresses starting at a base address set by dip switches.

Each card provides a well-defined function like a reference voltage, a digital to analog conversion, or the readout of push buttons. In general most cards provide the same function several times, for example an MDAC contains eight digital to analog converters. See Table 4.1 for an overview of the cards used in the Auger microscope.

REF	REFERENCE voltage. Provides a stable (drift $< 1 \text{ ppm minute}^{-1}$) reference voltage (V_{ref}). Two 12-bit digital to analog converters provide individual 0 to V_{ref} outputs: L_{ref} and H_{ref} (from Lens and High tension).
MDAC	Multiple Digital to Analog Converter. Provides 8 voltage outputs which are a 12-bit fraction of the applied reference voltage. Mainly used to extend the resolution of the QDCR cards.
QDCR	QuaD Current regulator. Provides 4 output currents (40 mA max) which are a 12-bit fraction of the applied reference voltage. Personality boards determine the current/voltage ratio. Using MDAC cards the resolution can be increased up to about 20 bits (although the total output will not be monotonic over this range).
DCA, DCB	Dual Current Amplifier, Dual Current booster. Provide 2 current amplifiers, boosting the output of a QDCR from 40 mA to 500 mA and 1 A, respectively.
PCI	Pulse Coder Interface. Generates an interrupt when one of (maximum) 6 rotary knobs (pulse coders) is turned, subsequent read out will show which knob was turned in which direction.
PBI	Push Button Interface. Generates an interrupt when one of 64 buttons is pushed, subsequent read out provides the address of the button.
MOB	Multiple Output Board. Provides 28 digital (open collector) outputs.
MIB	Multiple Input Board. Monitors 16 digital inputs, a MIB can provide an interrupt when one of the input changes state, or it can be polled.
BTR	Bus TRanslator. Couples the P80 bus to an external controller (typically an IO card in a PC). All bus signals are buffered and electrically decoupled using opto-couplers.
HVT	High Voltage Translator. The P80 system does not provide high voltage supplies, to fill this gap an interface from the P80 system to the 12 computer controlled high voltage supplies, which we already had, was designed.

Table 4.1 Brief description of the P80 cards used in the Auger microscope.

Communication on the bus follows a fairly simple protocol, which is easily implemented on a PC. The interface between the PC and the P80 crate goes via a standard IO card in the PC and a bus-coupler in the P80 crate. There is also a facility for interrupts, so the PC does not need to poll the P80 cards, but can still react quickly when the operator activates a button or a knob.

A disadvantage of the P80 system is that the communication is fairly slow, limiting the total number of supply updates to little more than 1000 per second.

4. Microscope control system

4.4 Illumination system

This section describes the part of the illumination system that has been brought under computer control, see Chap. 2 for the requirements on the illumination system, and see Chap. 3 for a description of the optics of the illumination system.

4.4.1 Beam deflection, alignment and stigmatism control

First the hardware available to perform these functions will be described, followed by the logical functions as seen by the operator, and the way the software translates between these two.

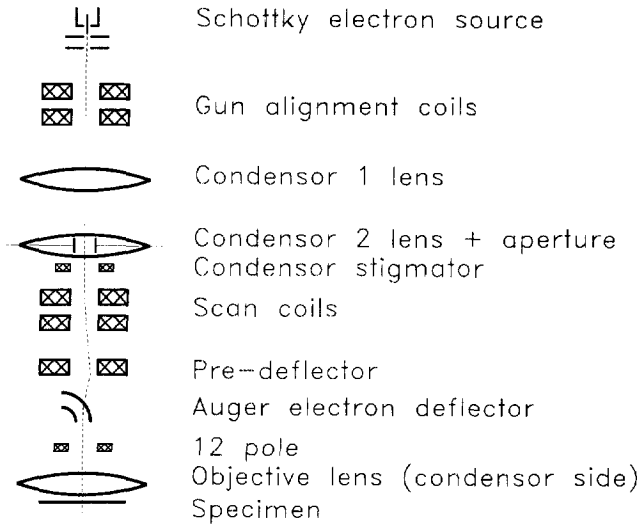


Figure 4.2 Hardware available for beam deflection and beam stigmatism.

Hardware

The hardware available to perform these functions (see Fig. 4.2) consists of: the gun alignment coils, the condenser stigmator, the scan coils, and the 12-pole. Of these only the scan coils and the 12-pole have been brought under computer control, the scan coils because they have to interact with the pre-deflector and the Auger electron deflector, and the 12-pole because it is a new element in the microscope, for which there were no power supplies available. This means that the gun alignment and condenser stigmatism have to be carried out using the original EM430 controls.

Beam deflection

For an operator beam deflection (beam shift and beam tilt) is an often used feature allowing him to illuminate the sample in the way he wants. The fact that it is often needed means that it should be readily available.

Before going to beam shift and beam tilt first a short word about the hardware used to accomplish these: the scan coils are the coils normally used to generate beam shift and beam tilt. In the Auger microscope however these coils have been moved much further away from the objective lens by the new section with the pre-deflector and the Auger electron deflector, as a result of which the maximum deflection in the pivot points for beam tilt and beam shift has become less, leading to smaller shift and tilt ranges.

Although this has not been tested, it might be a good idea to use the dipole effect (deflection) which can be generated by the 12-pole, combined with either the lower or the upper scan coils. The 12-pole is roughly at the position where originally the lower scan coils (nearest to the objective lens) were, and it would be a more effective deflector. The reason that we have not yet tried this is that the 12-pole is not a very strong deflector, and that it was mainly meant to be used to correct the sextupole effect expected from the Auger deflector. Using it as a dipole would mean that the sextupole strength would be decreased: part of the current through the 12-pole coils would be from the dipole, and the maximum current through a coil would be reached sooner in some coils.

A compromise is that there are controls for the dipole effect of the 12-pole. Deflection by this dipole will lead to a combination of shift and tilt on the sample, which for alignment purposes might still be useful - to get the beam in a region where the scan coils can be used for the final alignment.

Beam shift

Beam shift, the most often needed setting, has been made available always: the left upper rotary knob is shift-x, the right upper knob is shift-y. Because the shift function is always available, the shift values (position) are always displayed on the computer monitor.

The units in which beam shift is displayed are Angstrom [\AA] - this to get integer values on the computer screen. It should be realized that these values are calculated assuming a pencil beam deflected in the (thin) objective lens upper focal plane (see Fig. 4.3). The focal length f is assumed to be 11 mm (see Bleeker²), the deflection φ necessary for a shift δ is calculated from $\varphi = \delta/f$. The currents through the scan coils necessary to obtain this φ are calculated from the position of the pivot point (as aligned by the user) and the scan coil positions and dimensions (see the section on beam deflection alignment below).

4. Microscope control system

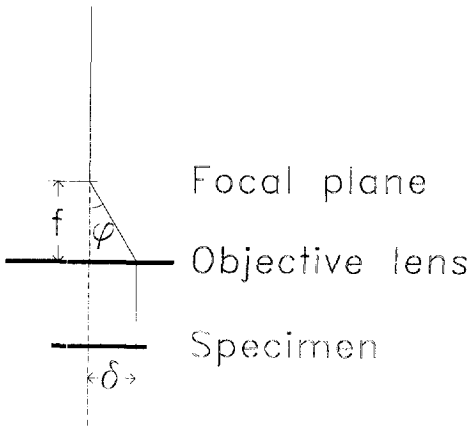


Figure 4.3 The beam is shifted over the specimen by deflecting it in the upper objective lens focal plane.

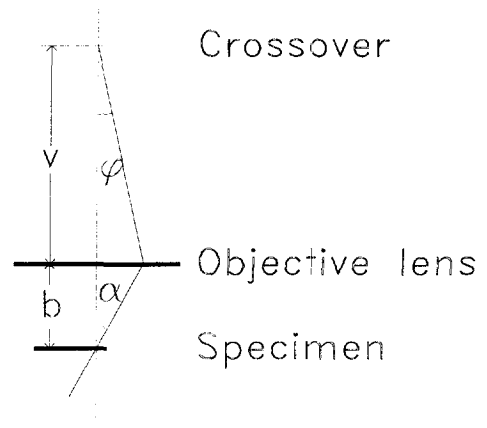


Figure 4.4 The beam is tilted on the specimen by deflecting it in the crossover before the objective lens.

Beam tilt

Beam tilt is not always available, but has to be selected using a push button. Because it is an often used setting, this button has been given a prominent place: it is the button closest to the operator, and also the only button in its group. The beam tilt values are shown when the tilt function has been selected.

The units in which beam tilt is displayed are degrees [$^{\circ}$]. Again it should be realized that these values are only correct when the following assumptions are met (see Fig. 4.4): the beam should be deflected in the crossover (gun image) between the condenser 2 and the objective lens, the objective lens is thought of as a thin lens with focal distance $f = 11$ mm, and the sample is thought to be in the lower focal plane (so the image distance $b = f$). The deflection φ necessary in the pivot point to obtain an angle α on the specimen is given by $\varphi = \alpha b / v$, where the image distance b is approximated by the focal length f , and the object distance v can be calculated from the position of the pivot point with respect to the scan coils (of which the position is well known).

The currents necessary to obtain φ are again calculated from the position of the pivot point and the scan coil positions and dimensions, see below.

Beam deflection alignment

The alignments for beam shift and beam tilt are very similar: the pivot points (both for x - and y -direction) must be placed at the correct position. For beam shift the correct position is the objective lens focal plane and for beam tilt this is the crossover (gun image) between the condenser 2 and the objective lens. Also the rotation between the upper and lower scan coils must be aligned as there will always be some misalignment between the upper and lower scan coils (due to mechanical imperfections).

The parameters that the user has to adjust are the four pivot points mentioned above (displayed on the computer monitor as Z mm below the center of the lower coils) and the rotation correction for both the x - and the y -coils (displayed as 0.0° to 359.9° with respect to the upper coils).

Beam tilt alignment will have to be performed regularly as the correct pivot point position depends on the condenser lens settings, which are changed fairly often. Perhaps if the condenser lenses were also computer controlled, this alignment could be carried out automatically, after initial calibration. The beam shift alignment depends on the objective lens focal plane, which normally is not varied much, and after the initial alignment this will probably not have to be carried out very often, if ever. The rotation correction should only have to be carried out once.

The deflections α and β necessary to obtain a deflection ϕ in a pivot point at a distance Z from the lower scan coil are given by $\alpha = -Z\phi/L$ and $\beta = \phi(1 + Z/L)$, as can easily be derived from Fig. 4.5. Note that α is negative in the example as shown in Fig. 4.5. The distance L between the scan coils is known to be 25 mm, so from the desired deflection ϕ and the pivot point Z as set by the user the deflections α and β in the scan coils can be calculated.

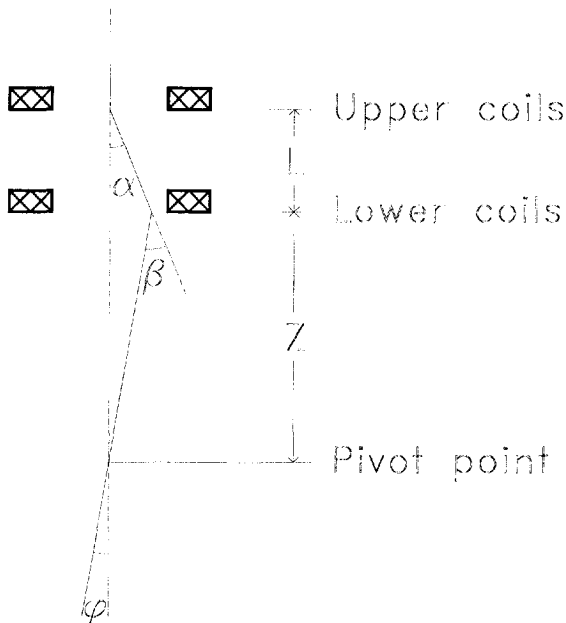


Figure 4.5 Deflections α and β necessary to obtain a deflection ϕ in a pivot point at a distance Z below the lower scan coil.

The scan coils have the 120° saddle-coil geometry, for such coils the current I through the coils necessary for a deflection α is known³ to be given by

$$I = \alpha R \sqrt{V} / (0.12 N l), \quad (4.1)$$

where R is the coil radius, V is the acceleration voltage, N is the number of windings on the coil, and l is the length of the coil.

The rotation alignment is achieved by virtually rotating the lower coils with respect to the upper coils, by letting part of the current for the x -direction flow through the coils of the y -direction, and vice versa. If the uncorrected currents for the x and y coils are $I_{lower-x}$ and $I_{lower-y}$ then

4. Microscope control system

the corrected currents are given by $I'_{lower-x} = \cos(\omega_x)I_{lower-x} + \sin(\omega_y)I_{lower-y}$ and $I'_{lower-y} = \sin(\omega_x)I_{lower-x} + \cos(\omega_y)I_{lower-y}$, where ω_x and ω_y are the rotation corrections in the x and the y -direction.

As was mentioned above, the dipole effect generated by the 12-pole is not used as part of the shift and tilt system, but as a standalone deflector (which will give a combination of shift and tilt). The only alignment of this deflector is the rotation: the directions in which the x -deflector and y -deflector act. This is rather like the rotation alignment of the scan coils, although in this case the rotation is just a matter of convenience, this alignment never has to be carried out if the user does not care in which direction a specific knob deflects the beam. See beam stigmatism (alignment) below for more detail.

Beam stigmatism

The condenser 2 stigmator is still powered by the EM430 supplies, so this stigmatism has to be carried out using the original controls of the microscope.

The 12-pole was mainly added to be able to correct the sextupole effect (3-fold symmetry) expected from the Auger electron deflector, but of course it can also be used to create a dipole effect (discussed under beam deflection), and a quadrupole effect. All three effects are controlled in the same way: the operator specifies the strengths (in arbitrary units) for two orthogonal dipoles, quadrupoles, and sextupoles. A first experiment where the operator adjusted strength and rotation (rather than two strengths) for the quadrupole and the sextupole was a bit disappointing: in practice the rotation is hard to judge when the amplitude has been set almost correctly.

The current through each of the 12 coils ($n = 0$ to 11) is given by $I_n = I_{2n} + I_{4n} + I_{6n}$ where I_{2n} , etc. are the contributions of the dipole, quadrupole, and sextupole effect, given by:

$$I_{2n} = A_{2x} \cos(n \pi/6 - \omega_2) + A_{2y} \sin(n \pi/6 - \omega_2) \quad (4.2a)$$

$$I_{4n} = A_{4x} \cos(n \pi/3) + A_{4y} \sin(n \pi/3) \quad (4.2b)$$

$$I_{6n} = A_{6x} \cos(n \pi/2) + A_{6y} \sin(n \pi/2), \quad (4.2c)$$

where A_{2x} and A_{2y} , A_{4x} and A_{4y} , and A_{6x} and A_{6y} are the amplitudes of the dipoles, quadrupoles, and sextupoles, respectively, and ω_2 is the rotation of the dipole.

Beam stigmatism alignment

There are two sources of beam stigmatism misalignment: 1) mechanical imperfections (some coils may have slightly more windings than others, or be nearer to the beam), and 2) the electron beam might not pass through the mechanical center, because of beam deflection higher up.

Mechanical misalignment requires 11 parameters for a first order correction - of the relative strengths: there are 12 coils, one coil can be taken as the 'standard', and the 11 others must be tuned to match. There are two disadvantages to this method: there is no simple way to compare the coils one by one (although one could in principle try to let the coils - one by one - deflect the beam a fixed distance from the screen center) and the correction is likely to be less accurate in practice when combinations of coils are used: it is like trying to get a stack of 12 plates to an accurate thickness by making each plate accurately (rather than stacking the plates and making the stack to size).

Correction of the misalignment of the electron beam (due to deflection higher up) with respect to the quadrupole/sextupole center requires two parameters: the shift in x and y direction of the quadrupole/sextupole center.

We have chosen to implement the alignment as follows: The alignment of the dipole only consists of the rotation ω_2 , which is mainly a matter of convenience and which is already incorporated in Eq. 4.2a. The alignment of the quadrupoles and the sextupoles consists of moving the four virtual centers until they coincide with the electron beam center, giving a total of eight parameters (two shifts for two quadrupoles and two sextupoles each). With these corrections the dipole effect in the quadrupoles and sextupoles can be corrected, for the sextupoles a correction of the quadrupole effect might also be needed, if in practice this turns out to be necessary the correction can easily be added in the software. The corrected currents I_{4n} and I_{6n} are given by

$$I_{4n} = A_{4x} \cos(n\pi/3) (1 + d_{4xx} \cos(n\pi/6) + d_{4xy} \sin(n\pi/6) + A_{4y} \sin(n\pi/3) (1 + d_{4yx} \cos(n\pi/6) + d_{4yy} \sin(n\pi/6)) \quad (4.3a)$$

$$I_{6n} = A_{6x} \cos(n\pi/2) (1 + d_{6xx} \cos(n\pi/6) + d_{6xy} \sin(n\pi/6)) + A_{6y} \sin(n\pi/2) (1 + d_{6yx} \cos(n\pi/6) + d_{6yy} \sin(n\pi/6)), \quad (4.3b)$$

where d_{4xx} and d_{4xy} , d_{4yx} and d_{4yy} , d_{6xx} and d_{6xy} , and d_{6yx} and d_{6yy} are the relative shifts in x and y -direction, for the x and y quadrupole, and the x and y sextupole, respectively. If these are zero there is no correction, typical (absolute) values are much smaller than unity.

4.5 Energy loss analysis system

Hardware

The energy loss analysis system consists of four main parts (see Fig 4.6): the EM430 imaging optics (everything below the specimen), the Gatan 607 spectrometer, the post-spectrometer optics, and the detector. The EM430 imaging optics are still powered by the original - not computer controlled - supplies and the reader is referred to the EM430 Operating Instructions⁴. The only part of the imaging optics that would be nice to have computer control over is the objective lens, in this way an important microscope setting could be added to saved configurations, and the interaction with the parallelizer would be easier (see Auger energy analysis system).

The next two parts, the spectrometer and the post-spectrometer optics, will be discussed below.

4. Microscope control system

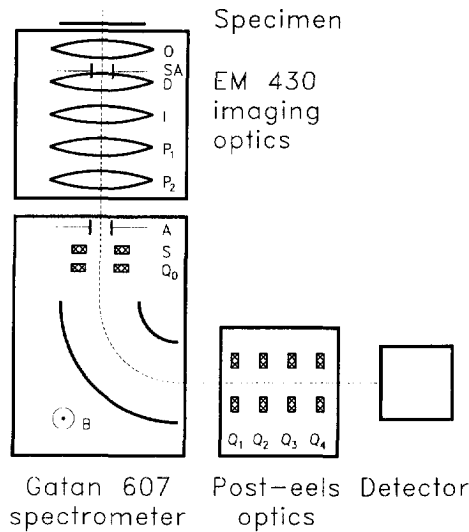


Figure 4.6 Overview of the energy loss analysis system.

4.5.1 Spectrometer control

Spectrometer hardware

The spectrometer, a Gatan model 607⁵, consists of a sector magnet which deflects the central energy over 90° and provides the energy dispersion, two quadrupoles rotated 45° with respect to each other, and a sextupole. Originally the liner tube inside the spectrometer magnet was electrically isolated, enabling electrostatic energy scans, but this feature has been given up for the sake of better (UHV) vacuum.

The elements above are still fed by the original (non computer controlled) power supplies, an analog energy-offset input (0 to 10V) connected to a digital-to-analog converter however allows computer-controlled energy scans (although the starting energy and the energy range still need to be set by hand).

Spectrometer user interface

As indicated above the spectrometer is still operated using the original controls: the strengths of the quadrupoles, the sextupole strength, the main magnet strength, and the strengths of two phases ac line compensation. The main magnet setting is so critical that three knobs with varying step size are used to tune it.

Because the spectrometer has to work together with the post-spectrometer optics (see Post-spectrometer optics control below) it would be useful to switch to P80 power supplies, some preliminary work (like reserving P80 addresses space and providing the necessary control-push buttons) has already been done. Problems can be expected with the ac compensation (there is no direct provision in the P80 system for this) and the fast scan system which is used to tune the

system by minimizing the zero-loss peak width on an oscilloscope screen.

The user interface will not change much when the switch to the P80 system is made, the current interface works well enough. The main advantage will come from the ability to save settings, and the more direct energy scan control.

The current interface for computer controlled energy scans is fairly primitive: the user must specify the starting energy, ending energy, and the number of steps to make. The spectrometer must previously have been tuned by hand, and the correct scan range must have been selected.

4.5.2 Post-spectrometer optics control

Post-spectrometer hardware

The post-spectrometer optics consists of four magnetic quadrupoles ($Q_1 \dots Q_4$), Q_3 in fact consists of two quadrupoles which are at the same position, but mutually rotated over 45° . Each coil in each quadrupole has its own computer controlled power supply, giving complete software control over all 20 coils and making it possible to do all alignments in software.

Post-spectrometer user interface

The system has been designed by Brink⁶ in such a way that the first (Q_1) and the last (Q_4) quadrupole set the magnification and focus in the dispersive direction, respectively, while the second (Q_2) and the third (Q_3) quadrupole set the defocus-width in the non-dispersive direction, as well as imaging Q_1 on Q_4 . Because each quadrupole has a fairly clear function there is no need for the software to provide virtual settings, the only virtual setting that might be useful is to 'teach' the software the relation between Q_2 and Q_3 so that they always image Q_1 on Q_4 , leaving one virtual knob for the defocus-width. Since this is a parameter that will probably not have to be changed often it was thought that the extra effort in the software was probably more than the time gained in practice.

The controls for the user are:

- 1) The strength all four quadrupoles.
- 2) The alignment of the center of each quadrupole (the ratio between opposite coils).
- 3) The rotation of Q_3 (the ratio between the two quadrupoles at that position).

Alignment

The alignments of the post-spectrometer optics consist of moving the effective centers of the quadrupoles so that they fall together with the beam center, and for Q_3 the rotation must be adjusted so that the enlarged spectrum is not rotated with respect to the detector. See Appendix A for alignment procedures.

Without any corrections the current I_n through each coil ($n = 0$ to 3) of a quadrupole is given by $I_n = A \cos(n\pi)$, where A is the amplitude (strength) of the quadrupole. With the correction for the center this becomes $I_n = A \cos(n\pi) (1 + d_x \cos(n\pi/2) + d_y \sin(n\pi/2))$, where d_x and d_y are the correction factors ($\ll 1$) for x - and y -direction.

The rotation of Q_3 is done as follows: the amplitudes A_{3x} and A_{3y} of the two quadrupoles (Q_{3x} and Q_{3y}) from which Q_3 is composed are given by $A_{3x} = A_3 \cos(\omega_3)$ and $A_{3y} = 1.3 A_3 \sin(\omega_3)$, where A_3 is the amplitude of Q_3 . The factor 1.3 in A_{3y} arises from the fact that

4. Microscope control system

this quadrupole (rotated 45° with respect to all other quadrupoles) is less strong than the others (it is only meant for small corrections, and for mechanical reasons it is slightly smaller).

There is no dipole (shift) correction of quadrupole Q_{3y} , because this quadrupole is only used to make a small correction on Q_{3x} it was thought to be an acceptable simplification (and this indeed has not given any problems in practice).

4.6 Auger energy analysis optics

Hardware

The hardware to energy-analyze the Auger electrons consists of (see Fig 4.7): the objective lens, the parallelizer coil, the Auger electron deflector, the electrostatic transport lens, the 180° hemispherical electrostatic energy analyzer, and the electron detector. All of these, except the objective lens and the detector, are powered by computer controlled supplies.

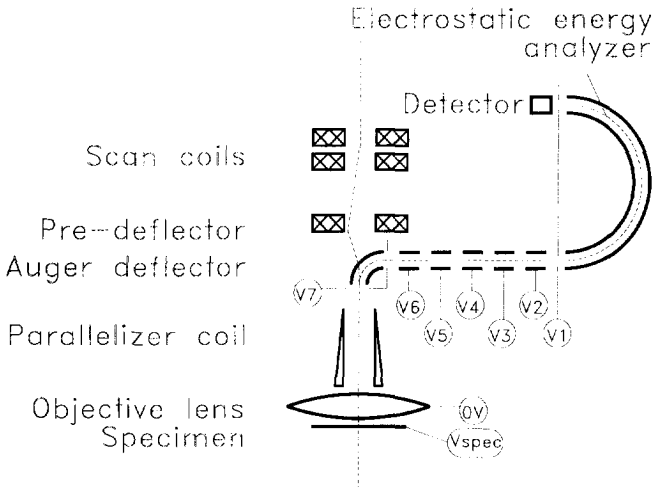


Figure 4.7 Auger electron analysis optics with the correction of the Auger deflector influence on the primary beam.

4.6.1 Parallelizer control

The design by Bleeker² incorporates a parallelizer coil that extends the $1/z^2$ magnetic field of the objective lens. A small extra coil is used to tune the low field area, just before the field is suddenly terminated by a μ -metal magnetic aperture.

The axial field profiles of the objective lens, the parallelizer coil and the extra coil have been measured independently and are shown in Fig. 4.6. The bump just before the Auger electron deflector is caused by stray field from the objective lens, so it scales with the objective lens current. The remanence of this field is also rather high.

In principle, for a given objective lens current, a best $1/z^2$ fit can be made, giving the ideal parallelizer and extra coil currents. Regretfully the objective lens current is not computer controlled, nor can it be read-out via the computer, so there is no way to let the software automatically adjust the parallelizer and extra coil currents. Also there is only one power supply for both the parallelizer coil and the extra coil, however, the $1/z^2$ fit shows that an extra coil current equal to the parallelizer coil current, but opposite in direction, gives quite a good fit (the current should be in opposite direction to correct the bump near the Auger electron deflector).

A final problem is that the relatively high impedance (almost 300 Ω) of the (long) parallelizer coil and the 15 V P80 power supply limits the current to about 55 mA, rather less than the 200 mA which would probably be optimal.

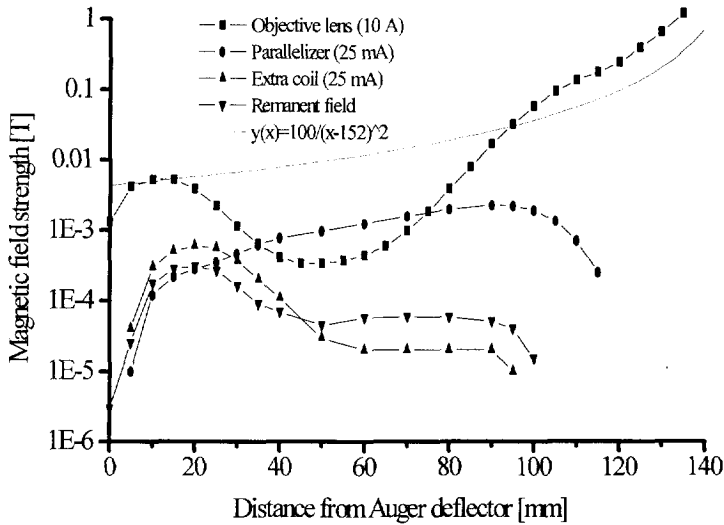


Figure 4.8 Magnetic field strength on the optical axis as a function of the distance below the Auger electron deflector. The sample is at 142 mm, the upper pole piece of the objective lens is at 134 mm, the parallelizer coil runs from 121 mm to 27 mm, the extra coil is centered at 29 mm, and the magnetic aperture is at 9 mm. Also shown is the line that corresponds to a (virtual) magnetic monopole 10 mm below the specimen.

4.6.2 Auger electron deflector control

Introduction

This is the most complex new system, mainly because two beams are affected: the primary (100 keV) beam illuminating the sample, and the secondary/Auger (0 to 5 keV) 'beam' coming back from the sample. The purpose of the Auger electron deflector is to separate the two beams by deflecting the Auger electrons over 90°, and preferably affecting the primary beam as little as

4. Microscope control system

possible. Rather than trying not to influence the primary beam at all we use a deflector which is monochromatic over a range of Auger energies: this range is deflected more or less by 90° , without the need to change the deflector settings, and without risk of changing the influence on (moving) the primary beam. The deflector consists of a combined $\vec{E} \times \vec{B}$ field, by letting the achromaticity of the electrostatic (\vec{E}) field work against that of the magnetic (\vec{B}) field not only the central Auger energy U_{Aug} - which is deflected over exactly 90° - will pass the deflector, but a whole energy range can do so.

Achromatic setting

The optimum achromatic setting is where the derivative of the radius R_{Aug} over which the electrons travel is zero with respect to the electron energy U_{Aug} . This occurs when the magnetic field force is twice as large as the electrostatic field force, and in opposite direction. From the desired radius R_{Aug} the magnetic and the electrostatic field strengths can be found by

$$B = \sqrt{8U_{Aug} m} / q R_{Aug} \quad (4.4a)$$

$$E = -2 U_{Aug} / q R_{Aug}, \quad (4.4b)$$

where m is the electron mass and q is the electron charge.

The energy range which can then be deflected is almost $U_{Aug}/2$ to $2U_{Aug}$, to achieve the largest range R_{Aug} should be chosen somewhat smaller as the central radius of the deflector (20 mm) because both higher and lower energies will follow a larger radius, as was shown by Van Aken⁷. A good choice is $R_{Aug} = 18.5$ mm.

Primary beam correction

The $\vec{E} \times \vec{B}$ field will also deflect the primary electron beam to such a large extent that correction with an extra magnetic pre-deflector and the scan coils is necessary. Basically what happens is that the scan coils deflect the beam off-axis, the pre-deflector directs the beam back to the optical axis - in such a way that it intersects the axis in the pivot point of the Auger electron deflector - and the $\vec{E} \times \vec{B}$ field deflects the beam exactly parallel (on axis) again. This is also the main reason that the scan coils have been brought under computer control: only in that way can these demands be fulfilled automatically (after alignment).

To find the correct settings for the pre-deflector and the scan coils we need to know the deflection φ_{90} of the primary beam in the Auger deflector, because this beam does not pass through the magnetic and electrostatic fields of the Auger deflector in such a way that the fields are always perpendicular to the beam it is not possible to write down a simple analytical expression for φ_{90} . It can however be reasoned that (in first order) the deflection must be directly proportional to E and to B , so that $\varphi_{90} = C_E E + C_B B$, where C_E and C_B are the proportionality factors. C_E and C_B are estimated in the alignment section below.

The deflections φ_{pre} of the pre-deflector and φ_{90} of the scan coils necessary to correct the effect of the Auger deflector are given by

$$\varphi_{pre} = \varphi_{90} + \varphi_{scan} = \varphi_{90}(1 + d_{Aug-pre} / d_{pre-scan}) \quad (4.5a)$$

$$\varphi_{scan} = \varphi_{90} d_{Aug-pre} / d_{pre-scan}, \quad (4.5b)$$

where $d_{Auger-pre}$ is the distance between the Auger deflector and the pre-deflector and $d_{pre-scan}$ is the distance between the pre-deflector and the upper scan coils.

4.6.3 Auger electron deflector alignment

The voltage V_{90} and the currents I_{90} , I_{pre} , and I_{scan} necessary to obtain E , B , ϕ_{pre} , and ϕ_{scan} can be estimated from the dimensions of the deflectors, respectively. These estimations will however never be completely accurate, and some means of correcting the estimations must be available, preferably in such a way that, once adjusted, readjustment can be minimal.

For the Auger deflector the power supply settings are calculated as

$$V_{90} = f_{E90} C_{E90} E \quad (4.6a)$$

$$I_{90} = f_{B90} C_{B90} B, \quad (4.6b)$$

where f_{V90} and f_{B90} are the correction factors, if these are 100% the estimated settings are used. The constants $C_{V90} = d_{el}$ and $C_{B90} = gap_{90} / N_{90} \mu_0$ depend on the deflector dimensions: d_{el} ($= 10$ mm) is the distance between the electrodes and gap_{90} ($= 20$ mm) is the gap between the magnetic pole pieces, both measured at the position of the central trajectory, N_{90} ($= 508$) is the number of windings on the deflector coil, and μ_0 is the magnetic permeability of vacuum.

The deflection of the primary beam can be estimated by $C_E = L_E q / \sqrt{2U_{prim}}$ and $C_B = L_B q / \sqrt{2m U_{prim}}$, where L_E (≈ 25 mm) and L_B (≈ 30 mm) are the lengths over which average fields E and B work and U_{prim} is the energy of the primary electrons. In principle we could use $I_{pre} = f_{pre} \phi_{pre} C_{pre}$ and $I_{scan} = f_{scan} \phi_{scan} C_{scan}$, where f_{pre} and f_{scan} are the correction factors and C_{pre} and C_{scan} are the constants containing the dimensions, however in practice an operator wishes the beam to be stable when he tunes the $\vec{E} \times \vec{B}$ settings, so a better choice is

$$I_{pre} = (f_{pre-E} f_{E90} C_E E + f_{pre-B} f_{B90} C_B B) C_{pre} \quad (4.7a)$$

$$I_{scan} = (f_{scan-E} f_{E90} C_E E + f_{scan-B} f_{B90} C_B B) C_{scan}, \quad (4.7b)$$

where f_{pre-E} , f_{pre-B} , f_{scan-E} , and f_{scan-B} are separate correction factors for the electrostatic and the magnetic correction.

The constant $C_{pre} = \sqrt{2m U_{prim}} gap_{pre} / q \mu_0 L_{pre} N_{pre}$ can be estimated by assuming a magnetic block field with a length L_{pre} ($= 3$ mm), generated by a coil with N_{pre} ($= 720$) windings (on two coils) over a $gap_{pre} = 1$ mm[†] between the pole-pieces.

The constant $C_{scan} = 15.8 R_{scan} \sqrt{m U_{prim}} / \mu_0 N_{scan} L_{scan}$ can be found by rewriting Eq. 4.1 to get the deflection angle as a function of electron energy U_{prim} rather than accelerating voltage V .

[†] Note that this gap was originally 2 mm, however, because the stray flux was a factor 10 larger than the flux between the pole pieces, the cores of the pre-deflector coils saturated at a central energy of the Auger deflector of only 200 eV. One of the adaptations of the pre-deflector to overcome this problem was a reduction of the gap by a factor of two.

4. Microscope control system

The scan coils are not likely to work in exactly the same plane as the Auger deflector and the pre-deflector, so a rotation correction of the scan coils will be necessary, dividing the current I_{scan} over the x and the y coils:

$$I_{scan-x} = \cos(\omega_{scan}) I_{scan} \quad (4.8a)$$

$$I_{scan-y} = \sin(\omega_{scan}) I_{scan}, \quad (4.8b)$$

where ω_{scan} is the rotation correction factor.

4.6.4 Transport optics and analyzer control

The electrostatic transport lens has been designed by Van der Stam⁸ and is capable of imaging the Auger electrons (after their passage through the Auger electron deflector) onto the entrance slit of the 180° hemispherical electron energy analyzer, in such a way that the analyzer has optimum transmission. The transport lens at the same time accelerates or decelerates the electrons, so that the Auger electrons which left the sample with the energy of interest enter the analyzer with the correct energy to be deflected over 180°, onto the detector. This analyzer pass energy depends on the desired energy dispersion (resolution): the lower the pass energy, the higher the resolution.

The parameters involved are the seven potentials of the transport lens - with respect to the sample, and the potential over the two hemispheres of the analyzer. For the user there are however only two parameters of interest: the energy he wishes to analyze, and the energy resolution with which he wishes to do this. The software again should provide two virtual settings and translate to the eight actual settings.

With simulations the transport lens has been optimized for five energy resolutions (1.0, 0.8, 0.5, 0.25, and 0.1 eV), as well as for seven entrance energies (60, 150, 300, 600, 1100, 1600, and 2100 eV). To simplify matters somewhat the user is restricted to one of the five simulated energy resolutions, but the energy which is analyzed can be chosen freely between 0 eV and 2100 eV. The 35 simulation results for each of the seven electrodes of the lens have been stored on disk (see Table B.2 on page 133) and a linear interpolation/extrapolation between the two nearest of these is used to find the setting for each electrode for any energy. A better interpolation is not sensible as the simulations jump between several modes of operation, and any interpolation between two such modes is not likely to be an optimum setting.

The correct voltage over the analyzer depends only on the energy resolution, and can be estimated from the analyzer dimensions.

4.6.5 Transport optics and analyzer alignments

The transport optics and analyzer alignments can be divided into three categories: 1) the energy resolution, 2) the analyzed energy, and 3) the efficiency with which electrons are transported and analyzed.

Energy resolution

The energy resolution is set by the voltage over the hemispheres of the analyzer, and the effect

of misalignment is in this case a scaling of the energy axis of energy spectra. The correct value can be estimated fairly accurately from the analyzer dimensions, calibration can be done using a specimen with known peak positions.

Analyzed energy

The analyzed energy is set by the voltage difference between the sample and the entrance slit of the analyzer ($V_{spec} - V_1$), or, in other words, the netto acceleration or deceleration from specimen to analyzer. The correct value is given by the energy with which the electrons of interest leave the sample minus the energy which the electrons must pass through the analyzer (this pass energy depends on the energy resolution). The effect of misalignment is in this case a shift of the energy axis of energy spectra. Calibration can be done using a known peak position. The most logical peak is probably the zero-energy secondary electron peak.

Transport efficiency

The transport efficiency depends on the potentials V_2 to V_7 of the transport lens and the potential of the specimen with respect to the rest of the microscope (this potential determines the initial acceleration of the electrons). V_7 also sets the central potential of the Auger electron deflector and so influences the energy with which the electrons pass through this deflector.

Linear interpolation between the two nearest simulation results is used to find the potentials V_2 to V_6 of the transport lens (V_1 is a function of the analyzed energy and V_7 can be chosen freely), in most cases this should produce a near optimum setting, but because the simulations sometimes jump between different modes of operation there will also be cases where the interpolation produces garbage. There is no simple way to optimize the system once and for all. Better results could be achieved by storing the optimum setting (as found in practice by trial and error) for many combinations of energy resolutions and energies, in this way increasing the number and the quality of the points to interpolate between. Support for this has however not been implemented.

Alignments

The potentials V_1 to V_6 of the transport lens and the potential V_{180} over the analyzer are calculated automatically, but the user can influence these by setting the fractions f_1 to f_6 and f_{180} with which the calculated values are multiplied. The range for adjustment is 0% to 200%, except for f_4 which cannot be turned above 100% (this is the highest supply voltage, 14 kV is really the limit).

4.7 Remote control interface

4.7.1 Analog interface

The P80 system is not able to make fast scans over the specimen due to the limited bandwidth of the digital P80 bus. Four analog (voltage) inputs provide a way to modulate the scan coils at higher frequencies, circumventing this limit. A disadvantage is that the software-aligned pivot points for shift and tilt cannot be used, and that the pivot points will have to be adjusted separately by tuning the ratio of the voltages on these inputs.

4. Microscope control system

4.7.2 Serial interface

The data acquisition system is controlled by another computer than the one controlling the microscope via the P80 system, a serial (RS232) interface between these two computers provides the means of communication and synchronization. The data acquisition computer acts as a master, sending commands to the microscope control computer, which acknowledges all commands by sending a reply. The data acquisition computer is able to specify the Auger electron energy, the energy loss, and the deflection on the sample, which is what is needed for energy scans and position (line or two-dimensional) scans.

Protocol

A 'standard' (often used) 7-wire RS232 protocol is used for communication: 9600 baud, 8 data bits, 1 stop bit, no parity, and hardware handshake. Using this protocol packets of data are sent between the two computers, these packets are composed as follows:

length		data 1		data 2		...		data N		checksum	
lo byte	hi byte	lo byte	hi byte								

Table 4.2 Composition of data packets for the serial-line remote control interface.

Packets consist of words, which are sent as low byte / high byte. The first word contains the length of the packet in bytes, $length = 2 + 2 \cdot N + 2$ (2 bytes length, $2 \cdot N$ bytes data, and 2 bytes checksum). Next follow N words of data, and the final word is a checksum (modulus 10000h) over the first $length - 2$ bytes.

Commands and replies

The first data word contains a command or a reply from the other side. Commands fall in the range 0 to 7FFFh, replies fall in the range 8000h to FFFFh. Table B.3 on page 135 lists the commands that have been defined so far. If no additional data is required $N = 1$ and the checksum follows immediately after the command or reply word, giving a minimum packet with a size of 6 bytes. If the command or reply does require additional data, this is put in data words 2 to N .

4.8 References

1. Mark S. Sanders and E.J. McCormick, *Human factors in engineering and design*, McGraw-Hill, Singapore (1987).
2. A.J. Bleeker, *Optical and mechanical design for 1 nm resolution Auger spectroscopy in an Electron Microscope*, Ph.D. thesis, Delft University of Technology, The Netherlands (1991), unpublished.

3. K.D. van der Mast, *Intro II*, Delft University of Technology, The Netherlands (1985), unpublished.
4. N.V. Philips Gloeilampenfabrieken, *Operating Instructions EM430*, part no. 9432 060 09001, Eindhoven, The Netherlands (1983), unpublished.
5. Gatan Inc., *Instruction manual for Electron Energy Loss Spectrometer Model 607*, Pleasanton California, USA (1982), unpublished.
6. H.A. Brink, *The Post EELS Optics*, masters thesis Delft University of Technology, The Netherlands (1995), unpublished.
7. R.B. van Aken, *An achromatic 90° deflector for Auger electrons*, masters thesis Delft University of Technology, The Netherlands (1991), unpublished.
8. M.A.J. van der Stam, J.E. Barth and P. Kruit, Design of a multi mode transport lens with optimization program SOEM, *Proc. SPIE conference on Charged-Particle Optics*, W.B. Thompson, M. Sato, A.V. Crewe, Eds., SPIE - The International Society for Optical Engineering, Bellingham, **2014** (1993), 45-56.



5 Detectors

This chapter describes the energy loss and Auger electron detectors, starting with the requirements, followed by possible detector types, the selected detector type, and the detector design.

5.1 Introduction; A summary of detector requirements

The count rate in coincidence experiments is always lower than in non-coincident cases - the whole purpose is to throw away signal, so that only the signal that is normally buried beneath other signal remains. One way of increasing count rate is to increase the excitation rate (the primary beam current), however, as can be seen in Eq. 2.1, there is a limit to the illumination current, given by the true-over-false ratio.

Another way to compensate the lower count rate is not to detect only one energy channel at a time, but to use a multi channel detector. In our microscope this means that the spectrometer exit slits that normally select one energy channel must be opened up, and that the detector must in some way provide position information about incoming electrons. This position then corresponds to an energy.

Summarizing from Chap. 2: both detectors must have a timing resolution of 1 ns or better and must be able to handle count rates of 10^5 events per channel per second, and 10^6 events per second over the whole detector. The energy loss electron detector must work with 100 keV electrons and must have about 200 channels. The Auger electron detector must work with 50 to 550 eV electrons and must have about 100 channels. The channels of the Auger detector should preferably be curved, matching the image of the spectrometer entrance slit.

5.2 Detectors described in literature and detector choice

This section describes the detector types found in literature and the most suitable detector type for our experiment is chosen.

5.2.1 Detector literature study

A good starting point for a detector literature study is the review article by Richter and Ho¹. It turns out that most types of detectors consist of micro channel plates (MCPs) followed by anodes. There are several common anode systems: wedge-and-strip anodes divide the incoming charge over several anodes, whose shape is such that the ratio in which the charge is divided depends on the position of the incoming cloud (Martin *et al.*² and Knibbeler *et al.*³). Resistive anodes and discrete anodes interconnected by RC elements can be used either with charge division (Lampton *et al.*⁴, Gao *et al.*^{5,6}, Firmani *et al.*⁷, Downie *et al.*⁸, and Tromp *et al.*⁹), or as delay lines, where the difference in arrival time between the pulses defines the position (Lampton *et al.*¹⁰ and Parkes *et al.*¹¹). The conclusion is that apparently these detectors can have between

5. Detectors

100 and 400 channels, can handle a count rate of up to 10^6 counts per second^{3,8}, can have a spatial resolution of 40 to 200 μm , and a time resolution between 0.15 and 5 ns.

The only true parallel discrete anode system (with an amplifier and discriminator per channel) that was found is that of Richter *et al.*¹² They use 96 independent channels and obtain $1.8 \cdot 10^5$ counts per second *per channel* at 100 % detection efficiency, and can go up to $2.5 \cdot 10^6$ counts per second per channel with 30 % efficiency.

Solid state detectors were also investigated, the 1 mm thick PIN diode detector described by Evensen *et al.*¹³ achieves a timing resolution of 2 ns at -130°C . In their setup the channels were 5 mm wide, but perhaps this can be reduced. The detector designed by McMullan *et al.*¹⁴ has 500 channels of 4 μm wide that can handle $8 \cdot 10^3$ counts s^{-1} each, but the timing resolution is only 10 to 100 ns (estimated). The conclusion is that these detectors do not (yet) achieve the timing resolution we need.

Detectors that have anodes, pre-amplifiers, discriminators and counters all integrated on a single chip (Hatfield *et al.*^{15,16}, Birkinshaw¹⁷) are an interesting development, but counting detectors such as these cannot provide the timing information we need. The same problem occurs with integrating detectors such as CCDs.

Another disadvantage of these integrated detectors is that they use small-area anodes which limits the count rate due to MCP saturation. The $25 \mu\text{m} \times 2 \text{ mm}$ anodes in the case of Birkinshaw can handle about 600 events per second per anode without danger of saturation (see *maximum count rate* in the next section).

5.2.2 Micro channel plate literature study

Because micro channel plates (MCPs) are an important aspect of most detectors, a literature study of their characteristics was also made.

Gain

The gain of MCPs depends on the energy of incoming electrons, on the voltage applied over them, and of course of the number of plates in a stack. Figure 5.1 shows the gain of our MCPs (as provided on the test sheets), and the generic gain characteristic of a dual plate stack (according to Hamamatsu¹⁸).

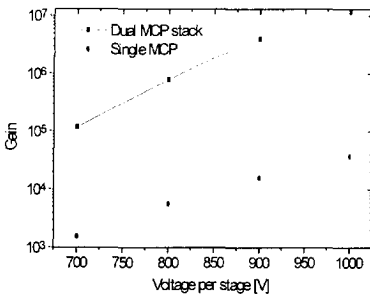


Figure 5.1 MCP gain as a function of the applied voltage.

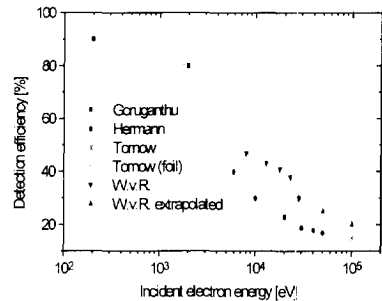


Figure 5.2 MCP detection efficiency as a function of the incident electron energy.

Detection efficiency

Goruganthu and Wilson¹⁹ give a quantum detection efficiency of 90% at 200 eV and of 80% at 2 keV. Hermann and Korn²⁰ have measured less than 40% at 5 keV and 20% above 20 keV. Wijnaendts van Resandt²¹ finds 50% at 10 keV, decreasing to 30% at 30 keV. He expects 20% at 100 keV, which is roughly in agreement with Tornow's²² result of 15% at 100 keV. Note that Tornow expects to be able to increase the detection efficiency to almost 100% for 100 keV electrons by using a special foil, see section 5.5.1 on page 75. Figure 5.2 combines all these values in a single graph.

Maximum count rate

The maximum count rate depends on the dead time per channel, the number of channels and the number of channels (in the last MCP) used per event. The dead time per channel is given by Hamamatsu¹⁸ as $T_d = egNR/Vn$, where e is the electron charge, g is the gain, N is the total number of channels, R is the plate resistance, V is the applied voltage, and n is the number of channels triggered in the last MCP per event. For the Auger detector we use Hamamatsu type F1208-21 plates, these have a 32 mm effective diameter, 12 μm diameter channels, an open-area-ratio of 57%, $R = 62 \text{ M}\Omega$ resistance, and $n = 7$. From the dimensions we can derive $N = 4 \cdot 10^6$ channels. At $V = 900 \text{ V}$ the gain will roughly be $g = 10^6$, so the dead time per channel $T_d = 6 \text{ ms}$. If we take the maximum rate that can be handled per channel as 10% of $1/T_d$ we can handle about $9 \cdot 10^6$ events per second over the whole MCP, which should suffice.

Should a higher count rate be required in the future then special *hot* plates can be used that have lower impedances and correspondingly shorter recovery times (but also higher dissipation, so they are *hot*). MCPs have a negative temperature resistance coefficient and are thermally instable if the resistance becomes too low. It has however been shown by Feller²³ that cooling via discrete anodes in direct contact with the MCP can increase the maximum count rate by a factor 100, leading to maximum count rates in the $10^{14} \text{ m}^{-2} \text{ s}^{-1}$ range (which seems rather more than enough for a coincidence experiment with 1 ns time resolution).

Kawarabayashi *et al.*²⁴ describe an array of miniature photo multipliers, which resembles an MCP cut in even thinner disks. The advantage is that each disk has its own power connection, so recharging does not have to take place via the resistive wall. In principle this arrangement should be able to attain very high count rates, at present however the gain (measured: $\times 3$ using 3 dynodes, expected: $\times 230$ using 14 dynodes) is nowhere near the values we need.

5.2.3 Detector choice

Time resolution

The 1 ns timing resolution requirement rules out detector types that somehow accumulate events on the detector, be it charge in a CCD pixel, or counts in an integrated counter. It also rules out solid state detectors which work by collecting the charge of electron-hole pairs - created by incoming radiation - because the integration time required for sufficient charge collection is too long.

Count rate

The count rate requirement of 10^6 events per second over the whole detector rules out most

5. Detectors

encoding detectors like resistive-anode or wedge-and-strip detectors. Only one detector has been found that can achieve 10^6 events per second³, and this was after we had built most of the detection system. The bottleneck is not in the detector itself, but in the read-out and decoding electronics; to give an indication of the problems that can be expected: assuming 100 channels, and that the MCP produces 10^6 electrons, an electron landing in channel 1 corresponds to charge pulses of 10^4 and $9.9 \cdot 10^5$ electrons; reliably measuring 10^4 electrons in less than $1 \mu\text{s}$ is not trivial. The calculation of the ratio is probably best done digitally, this however requires digitization of the input signal with an accuracy between 14 and 16 bits (to prevent differential nonlinearity problems with the ADCs, see Johnson *et al.*²⁵), again this will not be easy to do within $1 \mu\text{s}$.

Conclusions - detector choice

For both detectors we have opted for dual (chevron) MCPs combined with multi-strip anodes (MSAs) which each have their own amplifier and discriminator. The advantage of such true parallel detectors is that they can achieve very high count rates, only limited by the recovery time of the MCPs. From the MCP exit plane a timing pulse with the desired resolution should be easily obtainable.

The main disadvantage of this solution is the large quantity of electronics needed to process all the individual channels. However, wire chamber detectors as used in high energy physics have roughly the same output characteristics as our multi strip anodes and are also associated with large numbers of channels. For these detectors read-out electronics have been developed which are commercially available, one such system is LeCroy's PCOS III system, which we plan to use.

5.3 Test of the detector and the pre-amp/discriminator combination

To confirm that the PCOS III wire chamber read-out system can also be used with our MCP-MSA detectors we have first build a simple test setup consisting of an electron gun, a magnetic lens, an aperture, a micro channel plate, 96 multi strip anodes, and the PCOS read-out electronics. Figure 5.3 schematically displays this setup.

First of all we have tested several ferrite cores for the Auger detector decoupling transformers (the anodes will be at high tension, while the pre-amplifiers and discriminators are at ground potential). Because of space constraints and the large quantity (96) needed these transformers need to be small. We have tested several types of miniature ($\phi 6 \times \phi 4 \times 2 \text{ mm}$) ferrite cores, coming to the conclusion²⁶ that the 3H2 grade ($\mu_r \sim 2000$, loss factor < 5 at 1 MHz) scores best. With these we get 10 mV amplitude output pulses in 50Ω (MCP at 1800 V, measured with a FET probe).

We have also tested both versions of the pre-amplifier/discriminator cards that are part of the PCOS system. Both expect 5 ns rise time pulses, the difference is in the decay time of the input pulses: 30 ns and 100 ns for the 2735DC and the 2735PC, respectively. The pulses from the anodes, via the decoupling transformers, are a lot faster: 1 ns rise time and 1 ns decay time. Not surprisingly the fastest of the two versions handles these pulses best. The conclusion²⁶ is that, even though our input signal is faster than specified, it is amplified and discriminated well by the 2735DC card.

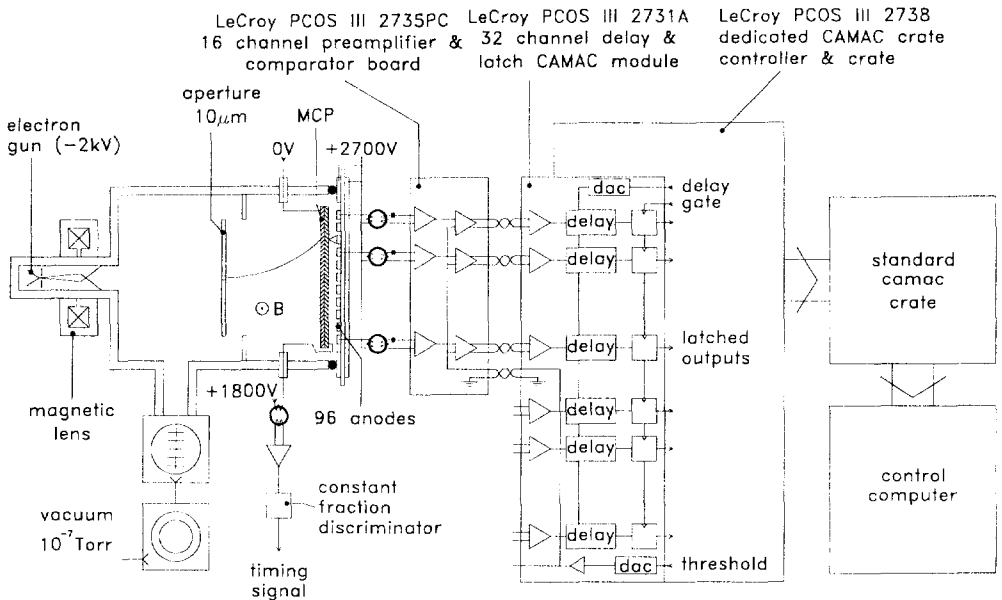


Figure 5.3 Setup to test the combination of the MCP/MSA detector with LeCroy's PCOS III system. An electron source, magnetic lens, and aperture (at the left) provide a varying illumination of the dual MCPs. The 96 channel MSA is coupled to the 2735DC preamplifiers using miniature transformers. The timing signal is picked up from the MCP exit plane, also using a miniature transformer.

5.4 Multi strip anode detector design considerations

In this section the electrical and mechanical demands on the detector will be discussed.

5.4.1 Electrical aspects

High frequency aspects

The signals from the detectors fall in the high frequency (HF) range fast and must be treated with HF design rules in mind. Figure 5.4 shows the main signal path as a thick line, this path has to be kept as short as possible to reduce the (self) induction. A good solution would be to make this signal path a transmission line, but this is difficult in practice.

Although not shown explicitly in Fig. 5.4 the secondary side of the transformers is also part of the signal path. By twisting the wires a transmission line is formed, and by tuning the number of twists/length the characteristic impedance can roughly be tuned to match that of the pre-amplifiers.

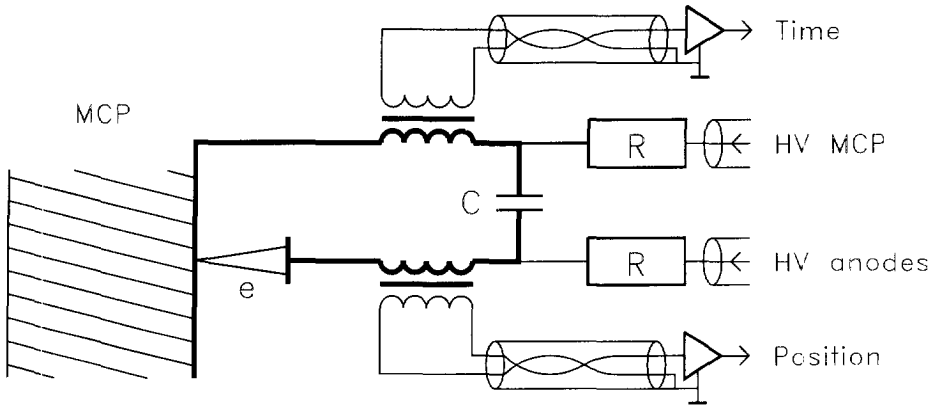


Figure 5.4 The thick line indicates the HF circuit for clouds of electrons leaving the MCP exit plane. The transformer in the MCP supply line picks up a timing signal, the transformer connected to the anode (1 of 96) on which the cloud lands provides a position signal. The capacitor C provides a short HF path. The resistors R serve to limit the current in case of a HV breakthrough.

Crosstalk aspects

With 96 and 192 channels and weak, fast, signals that are strongly amplified, the risk of crosstalk and oscillations is serious. In the detector design this has led to a solution where the signal lines connecting the strips either are as far apart as possible (in the vacuum feedthrough), or form a transmission line (in the form of twisted-pair wire). Twisting also serves to both emit and receive less noise, so this works both ways reducing crosstalk. To further reduce noise-pickup the twisted pairs have been shielded per group of 8 pairs (individual shielding would have led to an unacceptable total thickness).

All signals are pre-amplified as soon as possible, reducing the cable length to about 0.4 m. The discriminator outputs are twisted-pair wires carrying complementary (ECL) signals, in this way the radiation of the 'hard' digital signals from these cables is reduced.

High voltage aspects

With high voltage there is always the risk of instabilities or damage due to breakthroughs. To minimize the probability of a breakthrough the critical mechanical parts have rounded edges, see Fig. 5.5 for an example. Also, the decoupling transformers have been wound in such a way that the primary and secondary windings could be made from one long Teflon insulated wire each, without soldered connections that need to be insulated.

To reduce the effects of a breakthrough there are current limiting resistors in the supply lines, so that in the case of a breakthrough only the capacitance inside the detector is discharged, and not also the large (coaxial) cable capacitance (see Fig. 5.4).

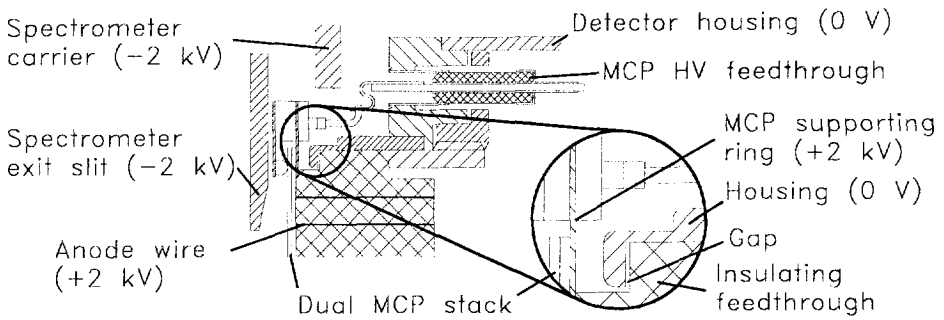


Figure 5.5 Detail of the (Auger) MCP, detector, and detector housing. Note the rounded edges of the housing where it is near the lead connecting the MCP HV. Also note the gap between the housing and the insulating feedthrough which increases the breakover length. In this gap is also the lead ring that provides the vacuum seal (not shown). The voltages shown are maximum values with respect to ground (0 V) and do not all occur simultaneously.

5.4.2 Mechanical aspects

Ultra high vacuum aspects

The ultra high vacuum (UHV) requirement for the microscope poses severe restraints on the materials that can be used. Two aspects are of importance: lack of out-gassing and the ability to withstand elevated temperatures (up to 200°C) during bakeout.

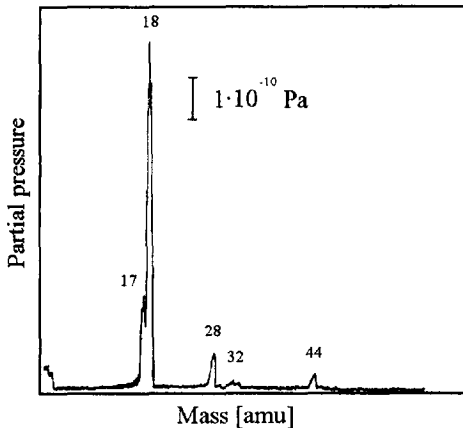


Figure 5.6 Residual mass spectrum of 20 cm² Stycast 1266 after 4 hours of pumping. The total pressure was $1.5 \cdot 10^{-9}$ Pa., mainly caused by water ($H_2O=18$) and air ($N_2=28$ and $O_2=32$). The peak at 44 might be CO_2 .

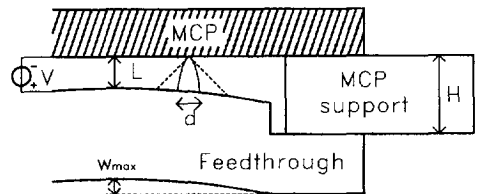


Figure 5.7 The MCP-anode distance L should be as small as possible to minimize spread out d , taking into account the deflection w_{max} caused by the 1 atm. pressure difference.

5. Detectors

Mainly for these reasons we have first tried to construct a detector made from glass with embedded tungsten wires, which would have been ideal from the UHV point of view. Because of problems with the tungsten wire positioning, we had to abandon this approach.

The final detectors are made from Stycast 1266, a two-component epoxy with remarkably low out gassing. Figure 5.6 shows the residual mass spectrum of a 20 cm² disk of Stycast 1266 after only 4 hours of pumping. The main peak (mass 18) is caused by water and the peaks at 28 and 32 are probably caused by residual N₂ and O₂, respectively. After mass 44 (maybe CO₂) no visible peaks occur, which indicates that the Stycast is not out gassing (which would probably produce hydrocarbons). A disadvantage of Stycast is that it can only be heated to about 100°C.

MCP-anode distance

The electrons from the MCP will spread out while traveling to the anode, if this spreading is too large the electron cloud will not end up on one anode strip, but on two or more. Although the PCOS system can handle clusters, giving the center position of a multi-anode hit, spreading over more than one anode is still disadvantageous because the signal per anode is decreased, leading to a worse signal/noise ratio at the discriminators.

The cloud diameter d at the anode is proportional to L/\sqrt{V} , where L is the MCP-anode distance and V is the accelerating voltage over this distance (see Fig. 5.7). The maximum voltage that can be applied over a given distance is roughly proportional to this distance, so even if we apply the maximum voltage at every distance, d still increases as \sqrt{L} . For this reason we have tried to make d as small as possible, leading to $d \geq 10 \mu\text{m}$ (within the tolerances with which we can machine the feedthrough, and with which we could measure the MCP support ring thickness H we should never get below this value, if for instance the support ring is slightly bent, the effective H will be larger, and so will d). Langstaff and Birkinshaw²⁷ describe a detector where the MCP rests on the passivation layer of a silicon chip, and in their case d is as small as $\sim 4.5 \mu\text{m}$. They warn that the space charge effect can cause extra spread-out of the beam, making a short MCP-anode distance even more important.

A further danger is that, in our case where the anodes are mounted directly on the vacuum wall, this wall (feedthrough) will bend under the pressure difference when the system is brought under vacuum, possibly damaging the MCP (see Fig. 5.7). For this reason the minimum MCP-anode distance d has to be at least as large as the expected pressure-induced deflection in the center of the feedthrough. For the maximum deflection of a free standing circular disk Timoshenko²⁸ gives

$$w_{\max} = \frac{3(5 + \mu)(1 - \mu)q a^4}{16 E h^3},$$

where $\mu = 0.25$ (number of Poisson), the radius of the energy loss detector (the largest of both detectors) $a = 68 \text{ mm}$, its thickness $h = 27 \text{ mm}$, the force $q = 1450 \text{ N}$ for 10^5 Pa pressure difference, and Young's modulus $E = 1.34 \cdot 10^9 \text{ Nm}^{-2}$ for Stycast (from Hasimoto²⁹). The resulting deflection $w_{\max} = 0.9 \mu\text{m}$, which is negligible compared to our aim of $d \geq 10 \mu\text{m}$.

5.5 Energy loss electron detector design

5.5.1 Increasing MCP efficiency for 100 keV electrons

As can be seen in Fig. 5.2 the efficiency of MCPs for 100 keV electrons is only about 15% or so. To improve this value several approaches are possible, to evaluate these it must be kept in mind that the timing and position resolution of 1 ns and 0.25 mm (~1 anode strip width) and the maximum count rate ($>10^6 \text{ s}^{-1}$) must not be deteriorated.

Low density films of insulators

Tornow⁶⁹ describes a method to increase the detection efficiency to almost 100% using a low density layer of a highly insulating material such as KCl or BaF₂. This layer is evaporated on an aluminum foil which acts both as carrier and as electric connection. The process by which the secondary electrons are generated is not completely understood, Tornow refers to an article by Goetze³⁰ which describes two possible processes and which presents more general measurements on the secondary emission yield of insulating films.

Experiments in our group³¹ with layers of KCl (BaF₂ is rather poisonous) on aluminum (household) foil have shown this method to work but have also shown that the layer is very susceptible to moisture, making the gain unstable. In our UHV microscope this may not need to be a problem, providing that it is possible to bake out the foil in situ - and assuming that it is possible to regenerate these foils in such a way. Another disadvantage is that the insulator needs to charge up before the multiplication starts, for low currents this might be a problem.

Scintillator - photo cathode

Another method to increase the detection efficiency might be to first convert the 100 keV electrons to photons in a scintillator, and to convert the photons back to (low energy) secondary electrons which can be accelerated to enter the MCP with optimum energy. First of all the scintillator must have very short rise (for the time resolution) and decay (to prevent noise due to background light from long-lived states) times. Secondly the scintillator must be thin enough so that the primary electron leaves the scintillator before the interaction region becomes too large (decreasing the position resolution), although for 100 keV electrons and 0.5 mm wide strips this is probably not a real issue. Thirdly the scintillator must have a high efficiency for 100 keV electrons in order to produce enough photons.

Degrader foil

Finally it is probably possible to decelerate the 100 keV electrons by passing them through a foil, causing them to lose energy in collisions, and choosing the thickness so that most of them leave the foil with some energy left. The disadvantages of this method are that the foil only works for one accelerating voltage, and that the scattering of the electrons in the foil might cause unacceptable loss of position information and consequently loss of energy resolution.

Efficiency improvement conclusions

Because no clearly preferred method was found, it was decided to postpone this decision, taking into account in the design of the detector that at a later stage a foil or scintillator might need to

be added. This has been done by providing space for such a device, by providing holes for mounting screws, and by providing electrical feedthroughs.

5.5.2 Energy loss detector design

The design of the energy loss detector is based on the Auger electron detector: dual MCPs with anodes deposited directly on the feedthrough. Because of the problems in making the Auger electron detector there is no working energy loss detector, but the design - assuming that the process by which the Auger electron detector is made can be mastered - is shown in Fig. 5.8 and is described below.

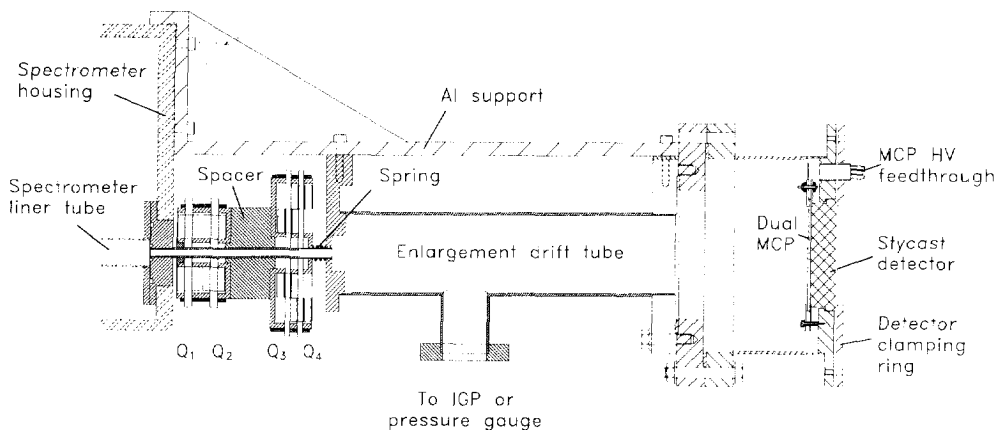


Figure 5.8 Overview of the post spectrometer optics and the energy loss detector. At the left the housing and drift tube of the spectrometer are partly visible. Next follow the four quadrupoles of the post-spectrometer optics, a long drift tube where the spectrum enlarges, and finally the detector consisting of dual MCPs and anodes deposited on a Stycast feedthrough.

The detector itself is just an enlarged version of the Auger detector, with straight instead of curved anodes. The MCP-anode distance is determined by a groove in the detector, as shown in Fig. 5.7.

To be able to place Q_1 as close as possible to the spectrometer the exit flange of the spectrometer has been adapted. The thin liner tube inside the quadrupoles is welded to a flange that meets with the adapted flange, the quadrupoles slide over this tube and a spring removes any play (and plates with varying thickness can be inserted at the other end to change the quadrupole positions). To prevent charging the inside of the liner tube has been gold-coated.

The large drift tube starts as soon as possible after Q_4 , this is where the beam starts to spread out rapidly. At the end of the large drift tube a conflat flange allows mounting of the detector, and the middle of the tube there is a conflat flange (facing down) which can be used for an additional ion getter pump, electric feedthroughs for the detector, or a pressure gauge.

Future improvements

There are some parts that still need to be designed: a shield to block X-rays generated by the zero-loss peak, a holder for the connector to the anode feedthrough, and a means to measure the position of the zero-loss peak (which can be used to correct for energy-drift).

The shield is probably best designed as a series of Al and Pb rings with increasing hole diameter (so that the beam just fits through). The idea is that the parts of the beam that fall beside the detector hit an Al ring, creating relatively soft X-rays, and that these X-rays in turn are absorbed in a Pb ring.

The connector for the anodes is probably most easily mounted by making a short tube on the detector clamping ring into which it slides. An idea has been to use computer style connectors consisting of rows of pins on 0.1 inch spacings, but it turns out that the standard connectors that meet with these pins take up too much space.

The zero-loss peak detector might most easily be made from two closely spaced wires or two PIN-diodes placed next to the MCP. If the signal from both wires or diodes is equal, the peak is centered on them. The procedure would then be to first center the zero-loss peak on the detectors, next the beam is deflected by a certain amount, bringing the energy range of interest on the detector. If necessary the zero-loss peak is brought back to the detector at regular intervals to correct for drift. Another possibility might be to decrease the intensity of the zero-loss peak by chopping the beam, leaving it only on the MCP for a small fraction of the time, and measuring the peak position with the energy loss detector itself.

The design of the flange which holds the detector has some extra mounting positions around the MCP for the Al/Pb stack and/or a zero-loss peak detector. Extra feedthroughs (like the MCP HV feedthroughs) can be used to electrically connect a zero-loss peak detector.

5.6 Auger electron detector design

5.6.1 Anode shape

The maximum width of the spectrometer exit slits is 25 mm, so the 96 anodes should fit in this space, leading to about 0.25 mm pitch. MCPs are manufactured in round shapes, the rectangle with the largest area that can be put in a circle is a square, so to use the MCP most efficiently the anodes should fill a $25 \times 25 \text{ mm}^2$ square (and the MCP must have a 35 mm effective diameter). To take the curved image of the spectrometer entrance slit into account the anodes must be curved as shown in Fig. 5.9.

To prevent charging the areas around the square anode area that fill up the circle of the MCP must also be conducting. This leads to the anode pattern depicted in Fig. 5.10, note that only the odd-numbered anodes have been drawn to prevent the figure from filling up completely. The anode width is 180 μm , with a 50 μm gap.

5. Detectors

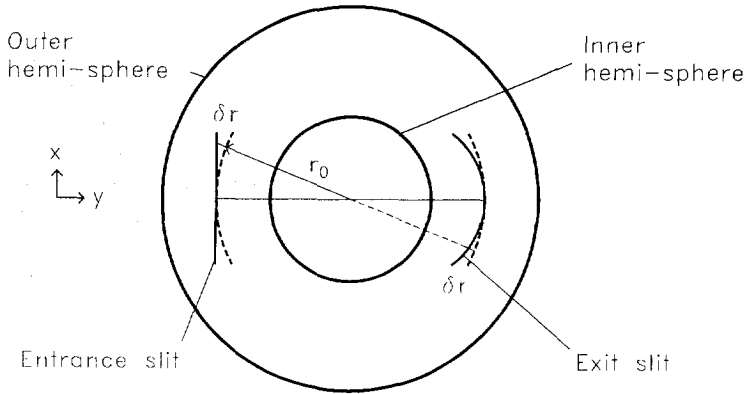


Figure 5.9 Auger electron energy spectrometer. The straight entrance slit is imaged on to a doubly curved line (solid lines). At a height x the straight entrance slit deviates a radial distance δr from the curved line which is imaged on an identically curved line, where δr follows from $(\delta r + r_0)^2 = x^2 + r_0^2$. The image of the straight slit will be the same distance δr from the image of the curved line, but to the other side. The resulting doubly curved line is the ideal detector channel shape.

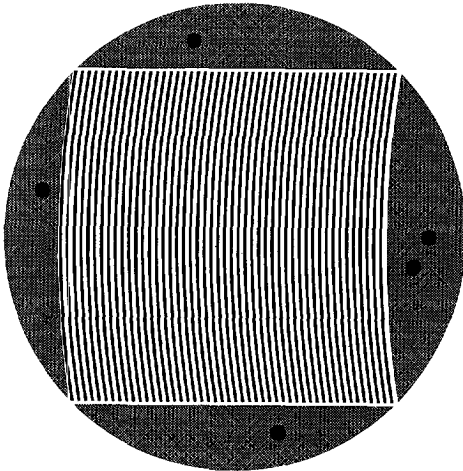


Figure 5.10 Shape of the anode pattern, note that only the odd-numbered anodes have been drawn. The four segments that fill up the circle collect the charge that does not fall on the strips.

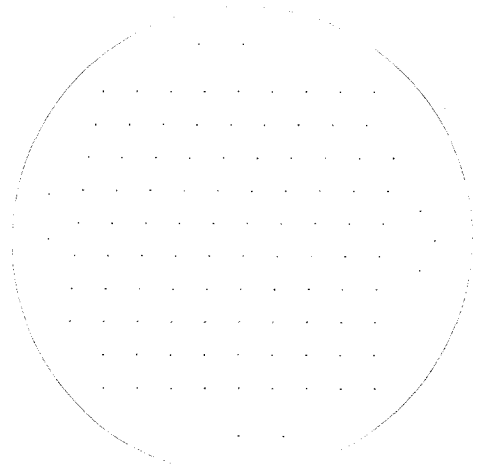


Figure 5.11 Pattern of the feedthrough wires, each wire ends under an anode. The extra wires (two at top, left, and bottom, three at the right) are for the connector alignment and to contact the segments.

5.6.2 Auger detector feedthrough

Each anode must be connected to an electrical vacuum feedthrough, so that it can be connected to the pre-amplifier. Because of HF and noise considerations, the signal path between the anode and the amplifier must be as short as possible, and must be shielded. To prevent crosstalk the feedthroughs should be as far apart as possible, and if possible should be shielded. Because the anodes are at high voltage, the feedthrough should also be able to withstand several kV with respect to the microscope ground; the mutual voltage differences between the anodes are negligible.

The use of commercial multi-pin feedthroughs has several disadvantages. First of all we have not been able to find a 96-pin feedthrough, so two or more feedthroughs would be required, which is not possible in the available space. Secondly there is a serious wiring problem: we would have to connect 96 closely spaced anodes to 96 feedthroughs, and to prevent crosstalk the wires should be shielded, preferably they should be 150 Ω coaxial cables (matching the amplifier input impedance).

To circumvent these problems we have decided to try and make a feedthrough on which the anodes can be deposited directly. This solves the wiring problem in vacuum, it minimizes the signal length in vacuum, and by distributing the 96 (almost 100) feedthroughs in a 10×10 pattern over the 25×25 mm² space they can be 2.5 mm apart, further than if the anodes are only connected at the edges, see Fig. 5.11. It also minimizes the total size of the pattern to be deposited. Figure 5.12 shows how each feedthrough wire ends up beneath a unique anode strip.

The capacitance between two adjacent wires is in the order of 1 pF, which, at the characteristic frequencies of 250 MHz, correspond to 600 Ω . If this value is compared with the pre-amplifier input impedance of 150 Ω , we see that we can expect about -14 dB coupling, and that it is essential to keep further coupling as small as possible (by going to transmission lines as soon as possible).

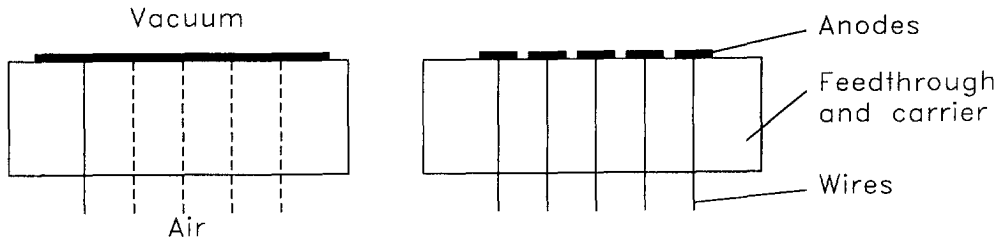


Figure 5.12 Two cross sections (mutually 90° rotated) of a feedthrough that also serves as the carrier for the anodes. With a feedthrough wire ending beneath each anode there is no need for wiring in the vacuum. The dashed lines are not in the plane of the cross section.

5.6.3 Detector housing

Figure 5.13 shows a cross section of the microscope at the detector level, looking from above. The MCP must be positioned as close as possible to the image of the spectrometer entrance slit (which falls on the exit slit), so it needs to be rather deep inside the spectrometer. The space

5. Detectors

available after the conflat UHV flange is rather limited because of the microscope support column, and this makes it impossible to design a detector that can be removed from the spectrometer while the spectrometer is mounted on the microscope.

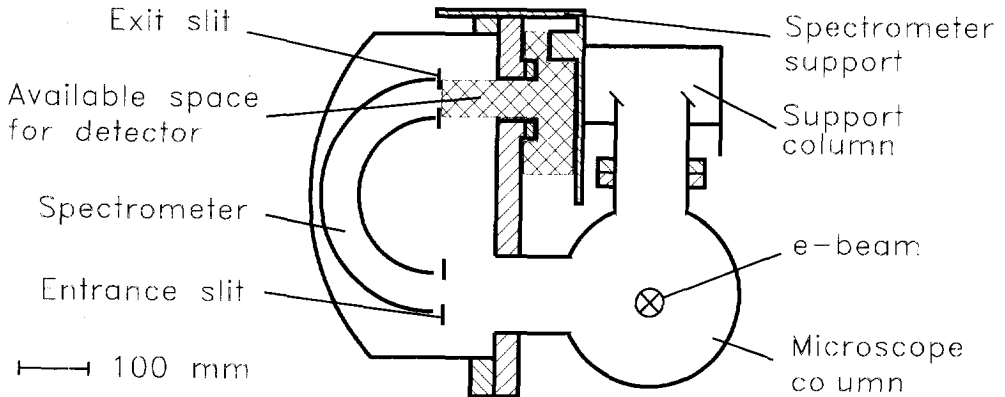


Figure 5.13 Horizontal cross section through the microscope at the Auger electron detector level. The available space for the detector (crosshatched) is limited by the microscope support column and the spectrometer support. The image of the entrance slit falls on the exit slit, the MCP must be positioned as close to this image as possible.

The detector housing must allow positioning of the MCP as close to the exit slit as possible, it must be possible to remove the actual detector from the housing, the housing must provide high voltage feedthroughs for the MCP, and it must be UHV-compatible. Figure 5.14 shows the detector housing that has been designed to meet these demands.

With the conflat flange at the right the detector housing is connected to the spectrometer housing. The bellows allow the detector to be positioned (as close to the image of the spectrometer entrance slit as possible) in an UHV-compatible way. Because the total length is slightly too large and because the pressure difference pushes the detector toward the spectrometer exit slit, the adjustment lever always needs to pull the bellows toward the flange, three adjustment screws push the lever away from the flange and allow both shortening and tilting of the housing.

The actual detector is held inside the narrow tube at the left end, with a lead seal between the housing and the detector. The detector is pushed against this seal from the inside, by a tube that is pushed into the narrow tube by twelve M3 screws. Around the detector and the narrow tube are four electrical feedthroughs which are used to make the electrical connections to the MCP and which hold it in place as well.

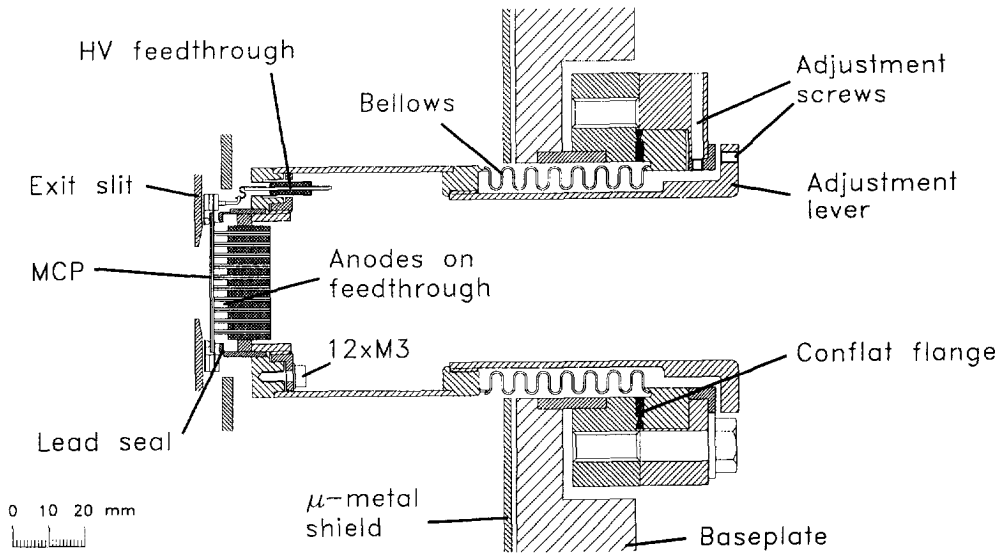


Figure 5.14 Housing of the detector, as positioned in the spectrometer. The MCP is supported by the four (only one visible) HV feedthroughs. The feedthrough with the anodes uses a lead vacuum seal, and is pushed against this seal by twelve M3 screws (one visible in the mirror position of the HF feedthrough). The whole spectrometer is encased in a μ -metal shield to prevent stray magnetic fields from interfering with the electron trajectories.

5.6.4 Detector connector

To connect all 96 anodes a custom connector has been made which uses miniature spring contacts. To keep all signal paths as short as possible the decoupling transformers have been placed immediately after the connector, inside the bellows of the detector housing. In order to be able to disassemble the connector housing it consists of two halves, which are held together by two screws and the brass tube that holds the transformers. The transformers have been slid into tubes which have almost been cut in half. The transformer wires pass through the slits made by sawing the tubes almost in half. Each tube houses sixteen transformers, so six tubes are required to house all transformers.

The connector housing must also provide connections for the electrical feedthroughs, for this purpose it has two metal cylinders on the outside, against which springs connected to the feedthroughs push. Both the cylinders and the springs have been gold coated to ensure reliable connections.

5. Detectors

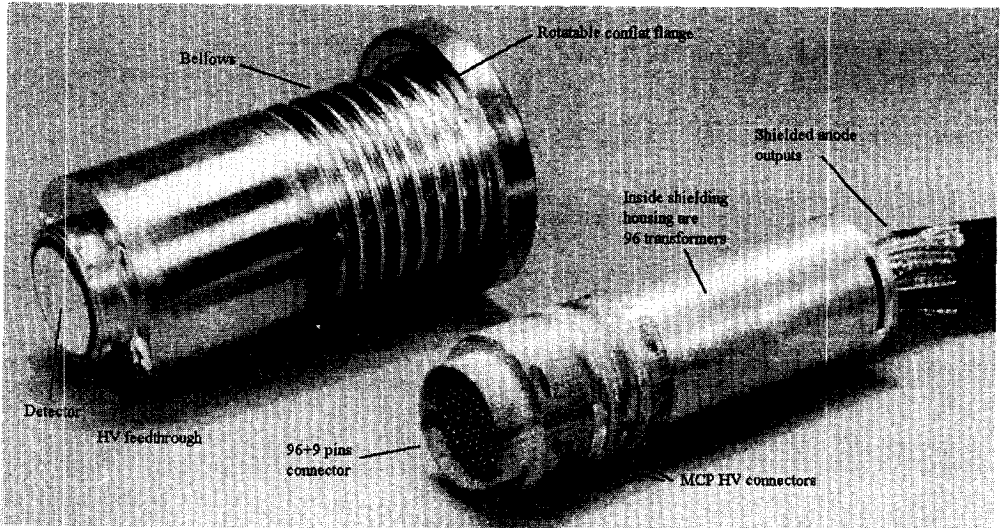


Figure 5.15 Left: detector housing, visible are the first (glass) detector, the MCP feedthroughs (the MCP is not mounted) and the bellows. Right: detector connector, visible are the 96 spring contacts for the anodes and the two metal rings which connect to the MCP feedthroughs.

5.6.5 Glass-tungsten detector

Because a feedthrough/detector made from only glass and metal is optimal from an UHV-point of view, we have first tried to construct such a device. Because we could not position the tungsten wires accurately enough (to make contact with the anode pattern) we had to give up this approach. Nevertheless the technique still seems attractive for designs with a somewhat less stringent position requirement, so the process we worked out is described here.

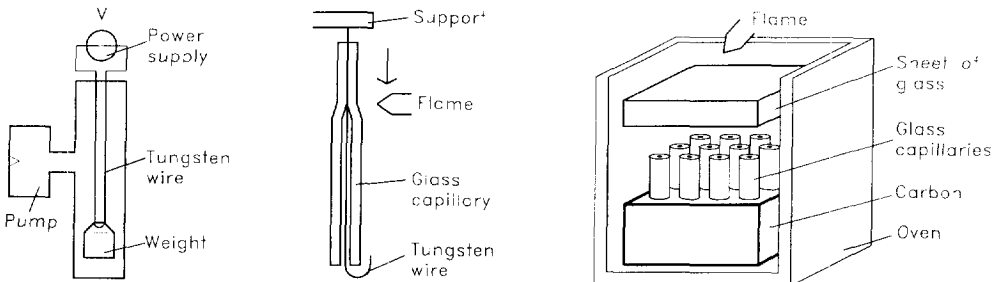


Figure 5.16 The tungsten wire was first cleaned and degassed by heating it white-hot in vacuum for several minutes. A glass capillary was then placed over the suspended wire, by heating the glass just to melting point with a flame the wire was fused in the glass. The capillaries were then cut to length. Correct diameter pieces were placed in a carbon block with holes at the feedthrough positions and a plate of glass was put on top. In an oven the assembly was pre-heated and finally a flame was used to melt the glass.

The tungsten wire we used was not straight, was contaminated, was heavily oxidized, and contained gas that led to bubbles when the wire was embedded in glass. To overcome these problems the wires were heated white hot for several minutes under vacuum conditions (better than 10^{-4} Pa.).

In order for the glass to wet the tungsten, it is necessary to first slightly oxidize the tungsten. This was done by heating the wires in air to a very dull red (just visible in a darkened room) for several seconds. There are several types of tungsten oxide, and only one works well. If the oxide is yellow, the wire has been too hot. When the wire has been embedded in glass, the color of the wire as seen through the glass indicates if the oxidation was correct: a silver metallic color means too little oxidation, a golden color means correct oxidation, and a black color means too much oxidation.

The wire was next embedded in glass capillaries to prevent oxidation during the rest of the process. Starting at the top the glass was heated with a small flame so that the glass flowed around the wire. From the areas where the wire had the correct color pieces of about 30 mm length were cut, and these pieces were sorted to thickness with better than 0.1 mm accuracy.

In a block of carbon holes were drilled with a CNC drill, in a pattern that would ensure that each hole center would coincide with an anode strip. In these holes the capillaries were placed, and a sheet of glass was placed on top. The whole assembly was heated in an oven that could be opened from above, and finally, using a large flame, the glass sheet and capillaries were molten together, after which the oven was slowly cooled.

The result was a thick sheet of glass with capillaries (that were in the carbon mold) sticking out on one side. The space between the capillaries was filled with epoxy to prevent the capillaries from breaking off and to strengthen the whole detector. This was then cut to shape and the surfaces with wires in them were polished. Finally the anode pattern was applied using lithographic techniques.

Because however the tungsten wires were not positioned precisely enough, not all wires ended up at the correct anode strip, and the detector could not be used. We also did not see a way of increasing the position accuracy: the main problem is that the wires (capillaries) must be held in position from below, while we require the accurate positioning at the top, where the wires can freely move (bend) when the glass is molten.

Acknowledgments: Joop Nieuwland and Henk Lucas did their utmost best to make the glass detector a success. They spend many hours cleaning the tungsten wires, oxidizing them, embedding them in glass capillaries (which they had first made to size), cutting the capillaries to the correct length pieces, sorting the pieces to outside diameter using a micrometer, and finally melting a sheet of glass over the capillaries to fuse them all together. Their craftsmanship is superb, and that even they could not obtain the required tolerances, must be seen as proof that this approach is not feasible.

5.6.6 Stycast detector

Because we could not obtain sufficient accuracy using glass, we switched to Stycast 1266. This two-component epoxy has very good UHV properties (see Fig. 5.6), and it is almost as fluid as water when the components have just been mixed, making it ideal for casting.

5. Detectors

Instead of tungsten, which was chosen for its compatibility with glass, we used golden wires in the Stycast to match the golden anodes. To position these wires we used two thin copper foils in which 0.1 mm diameter holes had been drilled at the desired positions using a CNC drill. The foils were placed on top of each other, and a 35 mm long, 80 μm diameter, golden wire was put in each hole. These wires were glued to one of the foils (with the long end sticking out the other foil). When all the wires had been placed, the foils were pulled apart and were placed in a Teflon mold, glued side down. The wires were pulled taut one by one, bending them so they could not slip back.

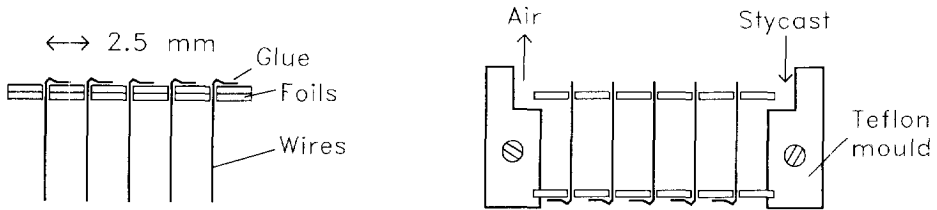


Figure 5.17 Construction of the Stycast detector. Golden 80 μm diameter wires were put through two copper foils with 0.1 mm diameter holes and were glued to one of the foils. When all wires had been placed the foils were pulled apart and were placed in a Teflon mould. Finally de-gassed Stycast was poured in the mould. Although not shown clearly the upper foil is also held by the mould, there are four holes for the air and Stycast around the inner circumference of the mould.

The two components of the Stycast were measured out and after mixing the Stycast was evacuated for about 10 minutes to remove air bubbles caused by the mixing. Next the Stycast was poured in the mold, which was then evacuated for about 10 minutes to remove any air left in it, the mold was topped up, and the Stycast was left to harden for 24 hours.

When the Stycast had hardened, the mold was split in two halves, and the block of Stycast was removed. It was then given a heat treatment as recommended by the manufacturer (one hour at about 80°C), to give it its maximum strength. Using a lathe, the detector was brought into its final shape. The two surfaces of the detector where the wires come out were ground using fine grinding powder, resulting in a matt surface. Polishing, resulting in a clear surface, turns out to give worse results. This either because the gold and the Stycast react differently to polishing, or it is because the matt surface provides the gold with a better hold. The golden anode pattern was deposited on one surface, and on the other surface round contact pads were deposited around each wire so that the pins of the connector only need to be aligned within the dimension of these pads.

At the moment of this writing another Stycast-based detector is under construction. Several improvements on the previous scheme have been implemented: The wires are straightened by rolling them between two glass plates (one plate lies on the table, the other is moved perpendicular to the wire that lies between them). This trick greatly eases the insertion of the wires in the foils, as it also removes extrusions made by cutting the wire. Another improvement is that now two foils are used on each side: the inner foils have small holes and position the wires. These foils are however necessarily very thin and cannot keep the wires taut. The outer foils are much thicker (more like plates) and also have much larger diameter holes. The wires are glued to the thick foils; in this setup the wires can be kept much straighter. One final

point is that the Stycast is now poured in several batches, with several hours between the batches. This is to prevent excessive heat generation as the Stycast hardens.

Because the wires are now much straighter, it is possible to remove more of the Stycast top layers (without danger of wires passing through the surface at the wrong position). This will hopefully solve the polishing problems.

5.7 References

1. L.J. Richter and W. Ho, Position-sensitive detector performance and relevance to time-resolved electron energy loss spectroscopy, *Rev. Sci. Instrum.* **57** (1986), 1469-1482.
2. C. Martin, P. Jelinsky, M. Lampton, R.F. Malina and H.O. Anger, Wedge-and-strip anodes for centroid-finding position-sensitive photon and particle detectors, *Rev. Sci. Instrum.* **52** (1981), 1067-1074.
3. C.L.C.M. Knibbeler, G.J.A. Hellings, H.J. Maaskamp, H. Ottevanger, and H.H. Brongersma, Novel two-dimensional position-sensitive detection system, *Rev. Sci. Instrum.* **58** (1987), 125-126.
4. M. Lampton and C.W. Carlson, Low-distortion resistive anodes for two-dimensional position-sensitive MCP systems, *Rev. Sci. Instrum.* **50** (1979), 1093-1097.
5. R.S. Gao, P.S. Gibner, J.H. Newman, K.A. Smith and R.F. Stebbings, Absolute and angular efficiencies of a microchannel-plate position-sensitive detector, *Rev. Sci. Instrum.* **55** (1984), 1756-1759.
6. R.S. Gao, W.E. Robert, G.J. Smith, K.A. Smith and R.F. Stebbings, High-resolution position-sensitive detector, *Rev. Sci. Instrum.* **59** (1988), 1954-1956.
7. C. Firmani, E. Ruiz, C.W. Carlson, M. Lampton and F. Paresce, High-resolution imaging with a two-dimensional resistive anode photon counter, *Rev. Sci. Instrum.* **53** (1982), 570-574.
8. P. Downie, D. Litchfield, R. Parsons, D.J. Reynolds, and I. Powis, High-resolution position-sensing resistive anode microchannel plate detector systems suitable for megahertz count-rates, *Meas. Sci. Technol.* **4** (1993), 1293-1296.
9. R.M. Tromp, M. Copel, M.C. Reuter, M. Horn von Hoegen, and J. Speidell, A new two-dimensional particle detector for a toroidal electrostatic analyzer, *Rev. Sci. Instrum.* **62** (1991), 2679-2683.
10. M. Lampton and F. Paresce, The Ranicon: A resistive anode image converter, *Rev. Sci. Instrum.* **45** (1974), 1098-1105.
11. W. Parkes, K.D. Evans and E. Mathieson, High resolution position-sensitive detectors using microchannel plates, *Nucl. Instrum. and Meth.* **121** (1974), 151-159.
12. L.J. Richter, W.D. Miehler, L.J. Whitman, W.A. Noonan and W. Ho, Improved multidetector for time-resolved electron energy loss spectroscopy, *Rev. Sci. Instrum.* **60** (1989), 12-16.
13. L. Evensen, A. Hanneborg, T. Happ, A.H. Wuosmaa, and R.R. Betts, A fast low noise silicon detector for electron spectroscopy up to 1 MeV, *Nucl. Instrum. and Meth.* **A326** (1993) 136-143.
14. D. McMullan, B.G. Williams, and T. Sparrow, Parallel detection for EELS, *Electron Microscopy and Analysis* (1985), 169-173.

5. Detectors

15. J.V. Hatfield, S.A. Burke, J. Comer, F. Currell, J. Goldfinch, T.A. York, and P.J. Hicks, A novel position-sensitive detector using an image-sensing integrated circuit, *Rev. Sci. Instrum.* **63** (1992), 235-240.
16. J.V. Hatfield, J. Comer, T.A. York, and P.J. Hicks, A new generation of integrated multichannel single-particle detectors, *Rev. Sci. Instrum.* **63** (1992), 792-796.
17. K. Birkinshaw and D.P. Langstaff, Silicon technology in ion detection - a high resolution detector array, *Int. J. of Mass Spectr. and Ion Process.* **132** (1994), 193-206.
18. Hamamatsu Photonics K.K., *Characteristics and applications of microchannel plates*, Technical manual RES-0795.
19. R.R. Goruganthu and W.G. Wilson, Relative electron detection efficiency of micro channel plates from 0-3 keV, *Rev. Sci. Instrum.* **55** (1984), 2030-2033.
20. K.H. Hermann and M. Korn, Measurement of the detection quantum efficiency of microchannelplates for medium energy electrons, *J. Phys. E: Sci. Instrum.* **20** (1987), 177-181.
21. R.W. Wijnaendts van Resandt, Absolute quantum efficiencies of micro-channelplates for 8-28 keV electrons, *J. Phys. E: Sci. Instrum.* **13** (1980), 1162-1164.
22. R.P. Tornow, A new method to measure and increase the detection efficiency of a microchannel plate for 100 keV electrons, *Meas. Sci. Technol.* **1** (1990), 576-580.
23. W.B. Feller, Low noise and conductively cooled microchannel plates, *SPIE 1243, Electron Image Tubes and Image Intensifiers* (1990), 149.
24. J. Kawarabayashi, H. Takahashi, T. Iguchi, M. Nakazawa, A. Takahashi, and R. Tokue, New array type electron multiplier as a two dimensional position sensitive detector, *Nucl. Instrum. and Meth.* **A353** (1994), 172-175.
25. P.M. Johnson, S.D. Beames, S. Bell, and B. Lohmann, Implementation of a position sensitive system in a scattered electron-Auger electron coincidence experiment, *Rev. Sci. Instrum.* **65** (1994), 3178-3182.
26. J. Dirker and J.S. Faber, *PCOS III test*, internal report DO-ISO collaboration, Delft (1992), unpublished.
27. D.P. Langstaff and K. Birkinshaw, The Dependence of the Resolving Power and Sensitivity of a Discrete Electrode Detector Array on the Proximity of a Microchannel-plate Electron Multiplier, *Rapid Comm. in Mass Spectr.* **9** (1995), 703-706.
28. S. Timoshenko and S. Woinowsky-Krieger, *Theory of plates and shells*, McGraw-Hill Kogakusha Ltd, Tokyo (1959).
29. T. Hasimoto and A. Ikushima, Mechanical properties of Stycast 1266 at low temperatures, *Rev. Sci. Instrum.* **51** (1980) 378-379.
30. G.W. Goetze, A.H. Boerio and M. Green, Field-Enhanced Secondary Electron Emission from Films of Low Density, *J. of Appl. Phys.* **35** (1964), 482-489.
31. H.A. Brink, *Onderzoek naar de mogelijkheid de detectie efficiency van MCPs te verbeteren met behulp van veld-versterkte-emissie*, internal report Particle Optics Group, Delft (1994), unpublished.

6 Data acquisition system

This chapter describes the data acquisition system. After a brief introduction the requirements and an overview of the system are presented. The remainder of the chapter consists of a detailed description of the system hardware and software.

6.1 Introduction; design philosophy

In the previous chapter we have seen that true parallel detectors, with a separate output for each energy channel, are the only type currently able to handle the count rates in our experiment. These detectors are however, of course, useless without a data acquisition system that meets their count rate and timing capabilities. Such a system has been designed and built. During the design several aspects played an important role (the design philosophy):

- We wanted a modular system for several reasons: it is easier to design, it makes any changes later (if required) easier, and by using commercially available components the development time can be reduced.
- To handle the high non-coincident count rates the strategy is to throw away unwanted events as soon as possible. As the complexity of decisions about the signal increases, the count rate must decrease.
- To provide flexibility all settings that might need to be varied have been brought under computer control. It has also been made possible to read-out all these settings, so a program can determine the state of the system.

Because there was no experience in the Charged Particle Optics Group with data acquisition systems with the complexity of this system, a collaboration with the Radiation Technology Group (also at the Department of Applied Physics) was formed. Most of the design described below has been performed in close collaboration with Rob Hollander, Victor Bom, Jef Dirker, and Jan Westerman, all from the last group.

6.2 System requirements

The first question is of course *what* we wish to measure. The project is aimed at the *time-coincident* detection of energy loss and Auger electrons, so this is one type of spectrum we must be able to acquire, and this is where the focus lies. In order to be able to tune the energy loss and Auger spectrometers we must also be able to measure non-coincident (single) *energy loss* and *Auger* spectra, and to tune the coincidence time windows we need to be able to measure a *time* spectrum (between energy loss and Auger electrons).

The second question is with which specifications we must be able to do these measurements. The data acquisition system requirements, as stated in the collaboration proposal¹, are:

6. Data acquisition system

Energy loss single rate:	10^6 s^{-1} total over all 192 channels, maximum 10^5 s^{-1} per channel.
Auger single rate:	10^6 s^{-1} total over all 96 channels, maximum 10^5 s^{-1} per channel.
Coincident rate:	$5 \cdot 10^4 \text{ s}^{-1}$ total, of which at the most $4 \cdot 10^4 \text{ s}^{-1}$ are false, assuming a 20 ns time window, and with a maximum of 10^4 s^{-1} per any set of energy windows.
Timing:	Timing with 1 ns accuracy, time windows must be Auger energy dependent to correct for time-of-flight (TOF) variations, maximum time variation over all Auger detector channels is 20 ns.
Detectors:	Dual micro channel plate (MCP) followed by multi strip anodes (MSA), at least 10^6 charge amplification, timing output from MCP 3 ns rise and 30 ns fall times.

The count rate requirements have been derived by assuming a 1 nA probe current, a 1% fraction of the primary electrons experiencing an energy loss in the 0 to 2 keV range, producing an Auger electron in the same energy range, flat energy loss and Auger spectra, and a 100% collection and detection efficiency. These assumptions are of course fairly crude, the problem is however that the outcome depends very strongly on the specimen under observation, so a more accurate estimation does not seem possible.

In any coincidence experiment the timing requirement is: *'the narrower the time window, the better'*, with a lower limit set by the coincidence peak width. In our coincidence experiment we are trying to filter out the correlated energy loss and Auger events, there is however always a possibility that an energy loss event falls in the same time window as an Auger event caused by a second (uncorrelated) energy loss event. The probability that this happens is proportional to the width of the time window (and to the square of the primary beam current), so the narrower the time window the higher the true/accidental ratio.

A lower limit on the time window width is set by the requirement that all correlated events must fall in it. The time spread which determines this minimum width arises from three sources: the time scale on which the interactions in the specimen occur, TOF variations from specimen to detector, and the time jitter in the detectors and the electronics.

The interactions in the specimen occur on a negligible time scale ($< 1 \text{ ps}$). The TOF variations of the (relatively slow) Auger electrons is in the order of a several nanoseconds. Because we measure the energy of the Auger electrons, the energy dependent contribution can be corrected by applying a separate time window for each energy. What remains then is the TOF variation within the energy width of one channel, and the angular TOF dependence, see Chap. 3 for more details. From the MCPs in the detectors a 1 ns timing accuracy is possible, and the rest of the electronics - with reasonably careful design - should be able to match this value.

6.3 System overview

The data acquisition system is shown schematically in Fig. 6.1. Both the energy loss electrons and the Auger electrons are energy dispersed before they are detected by dual MCPs combined with multi strip anodes. The signal from the MCPs is amplified after which an accurate and amplitude independent timing signal is derived using constant fraction discriminators (CFD, not

shown in Fig. 6.1). The MSA position outputs are handled by LeCroy's PCOS III system, this system provides amplifiers/discriminators for each channel and it can latch the status of all inputs and encode the triggered channels (the position module in Fig. 6.1).

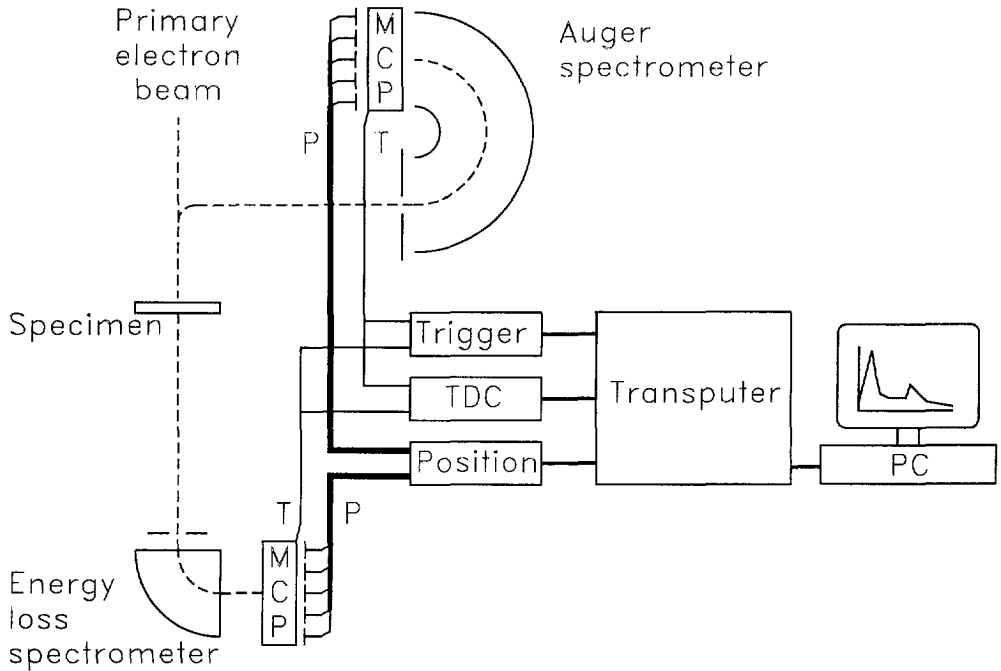


Figure 6.1 Schematic overview of the microscope, detectors, and data acquisition system. Both the energy loss and the Auger electrons are energy dispersed before they are detected by dual micro channel plates (MCP) combined with multi strip anodes (MSA). From the MCPs timing signals (*T*) are derived which are sent to the trigger unit and to the time-to-digital-converter (TDC). If the trigger unit detects an event the trigger information, the TDC information, and the position information (*P*) from the MSAs are sent to the transputers which perform further (real-time) processing. The spectra collected by the transputers are transferred to a PC for display and storage.

The trigger unit can detect three types of events: single energy loss, single Auger, and coincidence events. Coincidence and time spectra can be enabled as distinct types of spectra in the trigger unit, both however require the detection of coincidences (be it with different time window settings), so the only difference is in the type of event that the trigger unit reports. If the trigger unit detects a suitable (enabled) event it starts a readout cycle, this involves enabling the time-to-digital-converter (TDC) and the PCOS system. If not all the required data is available (if for instance the energy loss latch in the PCOS system contains no triggered channels at all) the event can be rejected, preventing a time-consuming read-out cycle.

If the event is not rejected, a read-out cycle is started, and the data from the trigger unit, the TDC, and the PCOS system is sent to a buffer memory (which serves to flatten peaks in the

6. Data acquisition system

count rate, not shown in Fig. 6.1). Two transputers take alternating turns to read the data from this buffer and further process the data, for instance applying a second (narrower) time window that depends on the Auger energy.

After a measurement has completed the spectra in the transputer memory are sent to the acquisition control PC, which displays and stores the spectra. This PC also controls the whole experiment: it sets the discriminator thresholds, the timing settings (including the coarse time window width) and the events to be triggered, it uploads the transputer programs and controls the transputers, and it communicates with the microscope control PC, for instance setting the Auger electron energy (range) that falls on the detector.

The remainder of this chapter will discuss the hardware and software in more detail.

6.4 CES hardware

The CES (Coincidence Electron Spectroscopy) hardware consists of several units: the signal pre-processing, the PCOS III system, the delay unit, the trigger unit, and the ECL bus coupler. All of these are described below.

6.4.1 Signal pre-processing

If an electron hits the entrance plane of an MCP, it should result in a cloud of about 10^6 electrons leaving the exit plane of the MCP, on a time scale of at the most a few ns. This results in two electrical signals: a current pulse in the MCP power supply line to replenish the charge on the MCP, and a current pulse from the anode(s) on which the cloud of electrons was collected. Although we have not yet been able to test the system using the final detectors a test setup has been used to confirm the suitability of the techniques described below (see section 4.3 on page 70).

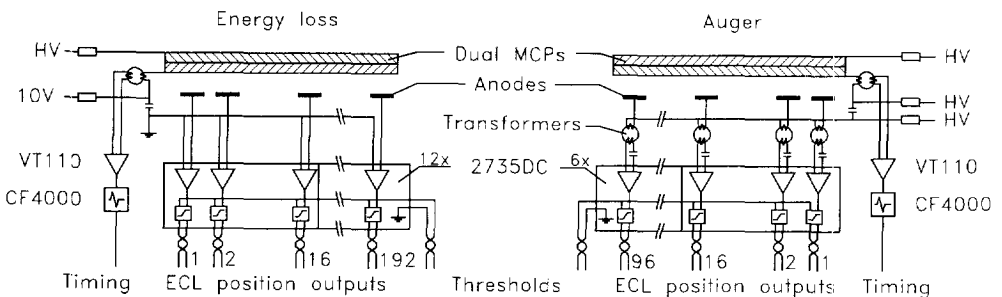


Figure 6.2 Signal pre-processing. The timing signals from the MCP exit planes are pre-amplified using VT110 amplifiers and CF4000 constant fraction discriminators to derive an amplitude independent timing signal. The position signals are preamplified using LeCroy's 2735DC boards. These boards have 16 amplifiers and discriminators each and feature complementary ECL outputs. Because the Auger anodes are at high voltage (HV) 1:1 transformers are used to decouple the HV.

Timing signals

The pulse in the Auger MCP power supply line is picked up by a 1:1 transformer, which serves to decouple the high voltage (HV, up to 3 kV) of the MCP. This transformer is home made from several turns of twisted-pair Teflon coated wire around a donut shaped miniature ferrite core (Philips 4322.020 3H2, $\phi 6 \times \phi 4 \times 2$ mm). The twisted pair acts as a coaxial cable, where one strand is used as the primary winding, and the other as the secondary winding. For the fast pulses we have the coupling is almost 100%, with negligible signal loss.

The output of this transformer is preamplified as soon as possible by a fast timing preamplifier (EG&G model VT110) which provides $\times 20$ amplification. The resulting signal is transported over about 2 to 3 m to the CFD (EG&G model CF4000) which provides a NIM output (with less than 1 ns time jitter).

The energy loss MCP will be connected in the same way, except that here we can keep the anodes at ground potential. The MCP exit plane will however be at several tens of volts with respect to the anodes, so we also need a decoupling transformer for the timing signal.

Position signals

Each anode is connected as soon as possible to one of the inputs of a LeCroy PCOS 2735DC preamplifier/comparator board. These boards provide 16 inputs which are preamplified and discriminated, so for the 96 channels of the Auger detector 6 boards are needed, and another 12 boards are needed for the 192 energy loss channels. For the Auger MCP again decoupling transformers - as described above - are used, combined with 1 nF series capacitors to prevent decoupling of the amplifier inputs to ground.

The ECL outputs of the boards are transferred via twisted pair flatcable over a distance of about 7 m to the 2731A delay and latch modules (see below). The discrimination threshold control voltage is also supplied over this flatcable and is computer controlled via the 2731A modules.

Much attention has been paid to the reduction of HF noise pickup. All input wires are shielded. The pre-amplifier boards are mounted in a copper box and the lids of this box use gold-coated spring contacts to ensure HF tightness. The power supply inputs are first filtered using RF chokes and capacitors, and we keep the power supplies away from the detectors/preamplifiers (at the other side of the room, about 3 m). To avoid ground loops we normally try to keep the grounds of individual units separated, using one grounding wire to a central grounding point per unit. In the case of the pre-amplifiers it is however sometimes necessary to directly interconnect units (with the cable shielding) and trial and error is used to find which grounds must be connected.

6.4.2 PCOS system

The PCOS III system of LeCroy handles the encoding of the position channels. The ECL outputs of the discriminators (see the previous section) are connected to the 2731A delay and latch modules. These modules have 32 inputs each so 9 modules are needed to handle all 192+96 channels. They must be in a separate CAMAC crate because the 2738 controller uses the CAMAC bus in a nonstandard way, achieving 10 times the normal speed of CAMAC. The 2738 in turn is connected to the 4299 PCOS read-out unit in a standard CAMAC crate. This unit

6. Data acquisition system

clusterizes the channels that were hit, and the width and centroid information for each cluster can be read out over a 16 bit ECL port at 100 ns per word.

The delay and latch units also contain digital to analog converters for the pre-amplifier thresholds and for the internal delays. This means that both can be set per 2731A unit, i.e., per 32 channels.

The custom build OR-unit provides outputs which indicate if at least one channel in a group of channels has been hit. This information is used during the delay tuning procedure and during a measurement to see if an event has to be rejected because of missing data.

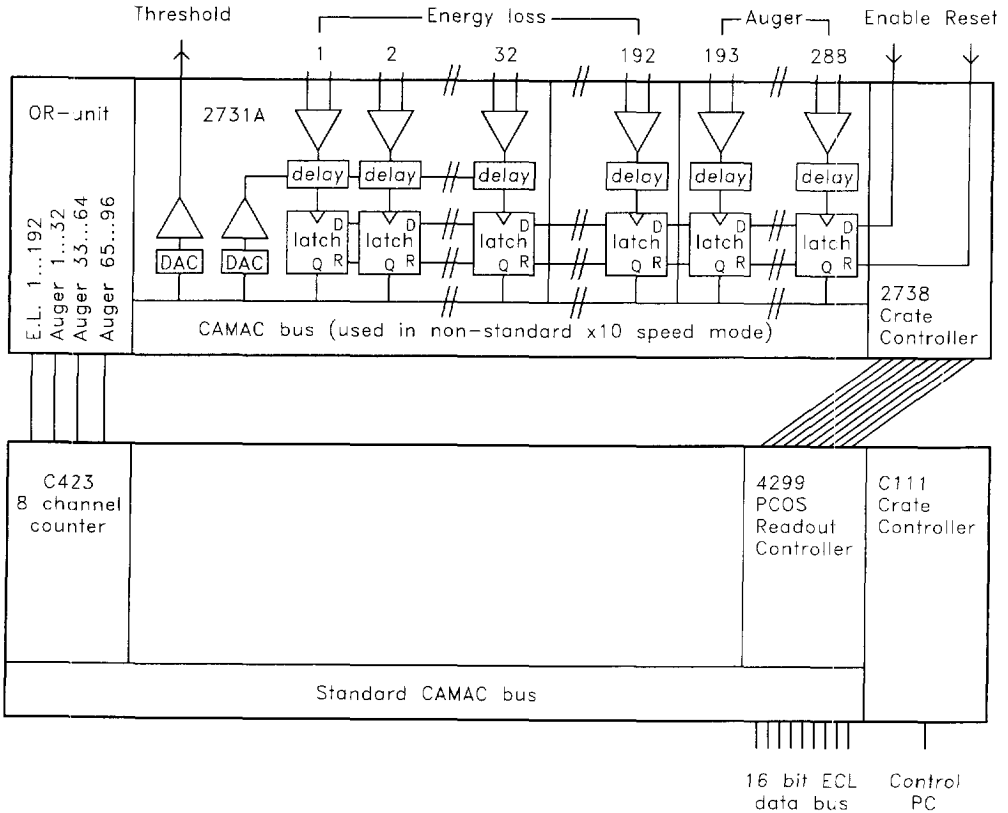


Figure 6.3 PCOS III system. The 2731A delay and latch units handle 32 inputs each (two 2735DC boards), so nine of these units are needed for all 288 position channels. The units are in a dedicated CAMAC crate that is controlled by the 2738 in a non-standard way, enabling read-out of the units at 10 times the normal speed. Via the 4299 Readout Controller the data is clusterized, resulting in a 16-bit data stream over the ECL bus. The (custom-build) OR-unit provides signals indicating that at least one channel in a group has been hit and is used for tuning (with the counters) and reject (with the trigger unit, not shown) purposes.

6.4.3 Delays

The delay unit provides accurate and stable variable delays for the energy loss and Auger timing signals. In Fig. 6.4 the delay chain for the energy loss signal is shown, an identical chain is used for the Auger timing signal (with delays A1 . . . A5 instead of E1 . . . E5).

Delay E1 produces a fixed 30 ns pulse width, because the dead time for delay E2 is always shorter than 30 ns this sets the dead time, independent of E2.

Delay E2 serves to align the energy loss and Auger timing pulses so that the energy loss pulses arrive just before the Auger pulses. It consists of two types of delays: long (> 20 ns) delays are made from lengths of coaxial cable, in this way these delays are pipelined and do not influence the dead time. A short variable delay is made using an integrated timing circuit. All the individual delays have been calibrated, and because the integrated timing circuit can produce a longer delay than the shortest cable delay it is possible to set any delay value between 320 and 643 ns with an accuracy and stability < 1 ns. Note that the cable-delay of 320 ns is always inserted to compensate the minimum 300 ns delay of the PCOS system.

Delay E3 determines the time window width (the Auger signal equivalent A4 exists to keep the circuits identical, but it is not really needed).

Delay E4 synchronizes the time window output with the energy loss timing (the coincidence output becomes active upon the arrival of an Auger electron, this moment can vary within the time window width).

Delay E5 produces a fixed delay so that when the TDC is triggered (if a coincidence is detected) it can see a delayed version of the timing pulses.

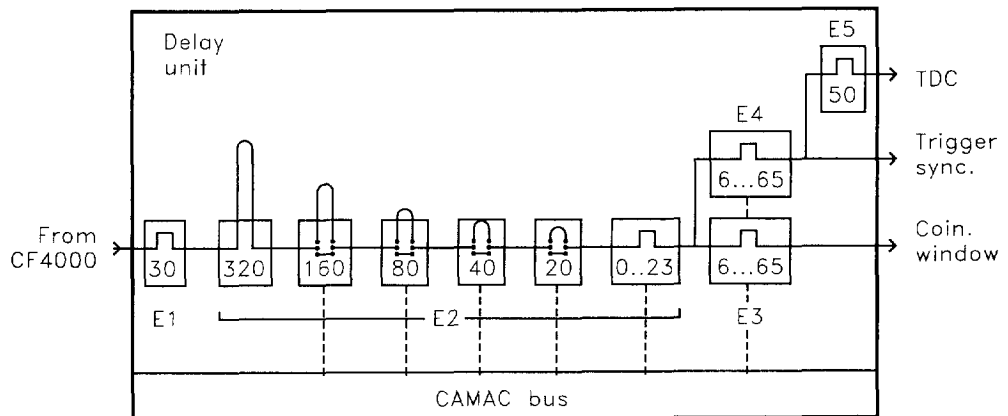


Figure 6.4 Delay unit. The above schematic is for the energy loss timing signal, an identical circuit is used for the Auger timing delays (A1...A5). The timing signal from the constant fraction discriminators is first shaped to a 30 ns pulse, which is delayed a fixed 320 ns. Additional delays of 160, 80, 40, and 20 may be inserted under computer control. A fine delay (variable pulse width) allows setting the total delay within 90 ps. Delay E3 determines the width of the coincidence window, delay E4 lasts slightly longer and synchronizes the time window output to the energy loss signal. Delay E5 provides a further 50 ns delay for the TDC.

6.4.4 Trigger unit

The trigger unit (see Fig. 6.5) can be set to respond to any combination of three events: single energy loss, single Auger, and coinciding energy loss and Auger events. It also contains the rejection logic for incomplete data and controls the read-out cycles.

The count rates for single energy loss or Auger events are much higher than for the coincidences, to reduce the rates that the rest of the system must handle it is possible to only count one out of $N = 1 \dots 256$ events, dividing the rate by N .

The coincidences are formally split in two separate modes, depending on whether a timing spectrum or a coincidence spectrum is being made. There is no difference between these modes as far as the trigger unit is concerned, but the way the transputers treat the data is different.

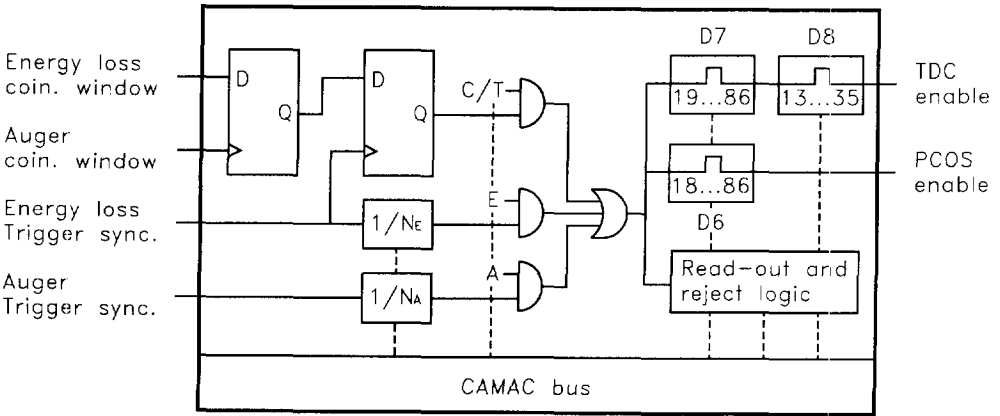


Figure 6.5 The trigger unit can detect coincidences and can react to single energy loss and Auger events. The rate of the latter two can be reduced by factors N_E and N_A . Each of these events can be enabled individually with the Time, Coincidence, Energy loss and Auger bits. The trigger unit also contains the TDC enable delays D7 and D8, the PCOS enable delay D6, and the rejection and read-out logic.

Detection and rejection

When an (enabled) event is detected, the TDC and the PCOS latch are enabled during certain time windows, and because the signals they use are delayed slightly longer than the signals used by the trigger unit, they can record the same event - slightly delayed in time.

After these time windows have elapsed, the trigger unit checks which data is available: that the TDC has seen both an energy loss and an Auger pulse, that the energy loss latch has seen at least one triggered position channel, and that the Auger latch has seen at least one triggered position channel. Depending on the type of trigger event, and on separate reject-enable settings, it is possible to reject an event if some data is missing. In this way a time-consuming readout cycle can be skipped.

Read-out cycle

If the event is not rejected, a read-out cycle is started. The trigger unit is the first to have its data ready and sends a 16 bit data word to the coupler. The coupler is like a three-way switch: it passes either the data of the trigger unit, the TDC, or the PCOS system to the buffer memory. The TDC is second in line (sending one data word), followed by the PCOS system. The number of data words that the PCOS system sends varies, depending on the number of channels that was triggered. It clusterizes triggered channels, per detector all clusters are transmitted one at a time. Clusters with width 1 (i.e., a single channel) require only one 16 bit data word containing the position, wider clusters require two data words with both position and width.

Note that even for single events the TDC is always read-out, because the PCOS system needs some time to prepare the first clustered information there is no time penalty in doing this, and it simplifies the electronics. The transputers just ignore the TDC data when it is not required.

Dead time

The dead time for events that are immediately rejected is equal to the coincidence window width or 30 ns, whichever is greater.

The dead-time for events that are rejected because some data is missing is roughly the width of the coincidence window, and the width of the PCOS (latch) enable window, and about 50 ns, so for a 20 ns coarse time window width and a 30 ns PCOS enable window this is about 100 ns.

The total (dead) time required to perform a read-out depends on the number of data words send by the PCOS system. There is an initial dead time equal to the width of the coincidence window, and the width of the PCOS enable window, and (roughly) 200 ns. Each data word send by the PCOS system requires an additional 100 ns, the minimum for a coincidence event is 4 data words (trigger, TDC, single energy loss channel, single Auger channel), so for a 20 ns coincidence window, and a 30 ns PCOS window, and one strip in each detector the total dead time is 650 ns.

6.4.5 Transputer hardware

The transputer hardware is hosted in a VME crate. This crate houses only two cards: one with the transputers, and one with the buffer memory.

Transputers

We use a VME card with two 20 MHz INMOS T800 transputers providing about $7 \cdot 10^5$ flops each. This 2TP-VME² system has originally been designed for the *ZEUS* project by the Electronic department of NIKHEF-H. The final version (MK4) is also sold commercially. This is what we bought.

The board features 4 Mb (16 Mb optional) private memory for each transputer and 512 kB triple ported memory (which can be accessed from either transputer or from the VME bus), VME access from either transputer, pipelined VME read/write cycles, and handling of VME interrupts and bus-errors.

The triple ported memory is slower than the private memory because of the arbitration: the first transputer that starts an access will automatically prevent other accesses until it has

6. Data acquisition system

finished. Read-modify-write cycles are still even slower: a transputer must first lock the triple ported memory for its own use, then perform the read-modify-write cycle, and finally it must release the memory again. The triple ported memory is however very useful for shared data, for instance to store spectra.

A 20 Mbit s^{-1} RS 422 link connects the transputers to the outside world (the acquisition control PC). The transputers are booted over this link and all communication with the acquisition program on the PC takes place over this link (commands, acquired spectra).

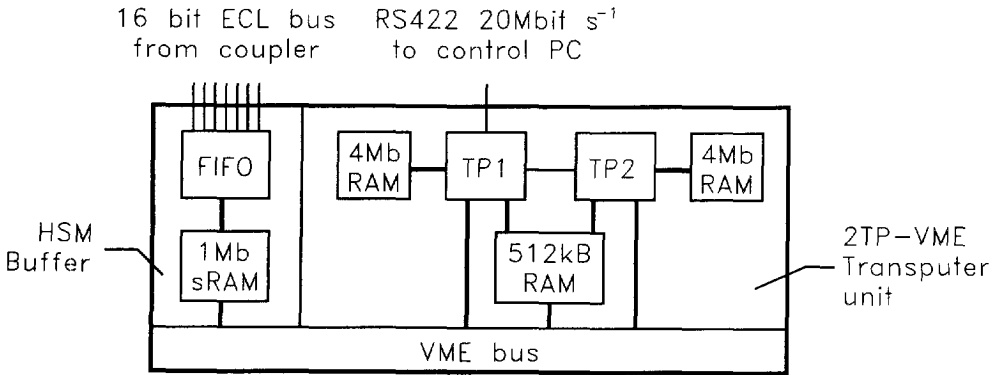


Figure 6.6 Transputer hardware. The HSM unit contains 1 Mb of memory that acts as a buffer. It is filled with data via a 16 bit ECL bus, and the two transputers take turns reading its contents via the VME bus. A small first-in-first-out (FIFO) buffer prevents data loss while the transputers are reading from the HSM. The transputers each have 4 Mb of private memory, and they share 512 kB of triple ported memory (which can also be accessed via the VME bus). One of the transputers is connected to the control PC via a RS422 serial line.

Buffer memory

We use a HSM8170 triple ported VME memory unit³ with 1 Mb static RAM as a buffer between the acquisition hardware and the transputers. This buffer serves to flatten peaks in the acquisition rate, so that the transputers only need to handle the average rate.

The buffer is filled via a 16 bit differential ECL port, which is in turn buffered by a 128×16 bit first-in-first-out (FIFO) memory. It is emptied over the VME bus by the transputers. While the transputers are reading blocks of data from the buffer the FIFO buffers any data that comes in over the ECL port. This means that the data blocks read by the transputer must not be too large, because then reading one block may take so long that the FIFO overflows.

6.5 CES software

The CES software consists of two parts: the software for the transputers, and the software for the data acquisition control PC (the software for the microscope control PC is discussed briefly in Chap. 4). The demands on these two programs are somewhat different: because the transputers must process as much data as possible in real time the emphasis is on speed, while the emphasis for the acquisition control PC software is more on functionality, allowing many experiments from within one program.

6.5.1 Transputer software

The transputer software must handle as many events per second as possible, and the exact actions that need to be performed depend on the experiment, on the type of spectra that are required. One way of increasing performance is therefore to write programs that are dedicated to only a few (maybe only one) experiments. However, coincidence, single energy loss, and single Auger spectra can be handled very efficiently by one single program, so separate programs are not always necessary.

Programming language

We program the transputers in OCCAM, a language specially developed for multi tasking, multi processor systems such as ours. We use the development library and cross-compiler supplied by INMOS, more specifically the version that runs under MS-DOS.

Common code

There are two types of code that can be reused: the first is the code common to both transputers, i.e., the code that performs specific actions on the experiment data. This code is common to the transputers but varies between programs. The second type is code that does not vary between programs: there are several 'household' tasks that need to be performed in any experiment, and the code to do this can be the same for all programs. These 'household' tasks consist of:

- Communication with the control PC. The commands used in this communication consist of a fixed set of commands (reusable) and experiment specific commands (non-reusable).
- Handling of interrupts. The most important one from our point of view is the buffer-full interrupt, which means that the buffer should be copied to the private memory of one of the transputers, and that that transputer must start processing the data. It occurs before the buffer is completely full, so the transputers still have some time to react. The other interrupts indicate errors that occurred and are counted for statistical purposes, to see if for instance the experiment is not running too fast:
 - FIFO overflow interrupt. This indicates that the FIFO received more data than it can buffer, for instance because a transputer took too long reading data from the buffer.
 - Buffer overflow interrupt. This indicates that the transputers took so long to handle the data they previously fetched from the buffer that they were not ready for the next load when it came. This means that the data rate is too high.

6. Data acquisition system

- Hardware errors: VME bus errors, dynamic memory refresh errors, external events A and B, external errors. These have never occurred yet.

Acquisition data format

Although the programs perform different tasks, they must all handle the same raw data that comes from the acquisition hardware (via the buffer). The transputers process this data serially in the same order as in which the buffer memory was filled. This means that in principle they can expect to see a trigger word, a TDC data word, and zero or more PCOS data words, after which the sequence repeats.

To provide robustness in case the data sequence is in some way corrupted, the three most significant bits of each 16 bit data word are used to indicate the data type. In this way a corrupt sequence can be recognized, and by simply skipping data until the next trigger word the process can be resynchronized. At the moment only four of the eight possible word types are used, Table 6.1 lists the format of these four types.

bit 15...13	data type	bit 12...0	legend (x=unused)
110	trigger word	x xxxx xxxx caet	t=1 time e=1 energy loss a=1 Auger c=1 coincidence
010	TDC	x xxxx tttt tttt	tttt tttt=8 bit time [ns]
000	PCOS position	a aaaa aass sshh	a aaaa aa=unit address ss ssh=strip address / cluster center h=half bit cluster center (h=1 if bbbb is an even number)
100	PCOS width	0 0000 0000 bbbb	bbbb=# strips in cluster

Table 6.1 Format of the 16 bit data words from acquisition hardware. The PCOS delay&latch units each handle 32 strips, because we number the Auger units as 1 to 3 and the energy loss units as 4 to 9 the total position (a aaaa aass sshh) simply indicates the strip position, with 0 to 190 as Auger strips and 192 to 574 as energy loss strips (191 and 575 are impossible, they would indicate a cluster centre outside the detector).

Performance

Westerman⁴ has studied the performance we can expect from the two transputer system. His conclusion is that we should be able to handle $2 \cdot 10^5$ coincidence events per second, assuming one single energy loss channel and one single Auger channel per event, and assuming that we require 45 transputer instructions (of 25 transputer clock cycles each) to process one event.

There is still room for optimization of the current transputer software: the spectra and the look-up table for the time windows are currently stored in shared memory. Moving these to private memory should give some performance gain:

- Currently about 23 lines of OCCAM source code must be executed when a coincidence

event is accepted, 2 of these lines (locking and releasing the private memory) can be removed if the spectra are moved to private memory. These lines however contain very simple commands that probably take up less than simply $2/23 = 9\%$ of the total time, so the gain is probably only a few percent in the maximum rate at which coincidence events can be accepted.

- Much more often than accepted an event is rejected. Especially the narrow time window will probably reject many events, to apply this window the time window lookup-table must be accessed. Although these accesses are read-only and do not require locking of the private memory there is a risk that if both transputers are simultaneously processing data they might spend a significant amount of time waiting for each other.

Transputer programs

The program *ces.btl* can simultaneously build four types of spectra from the incoming data, namely time, energy loss, Auger, and coincidence spectra.

The time spectra consist of a 256×191 matrix of 32 bit integers. Each element contains the number of times that the corresponding combination of time (0 to 255 ns) and Auger channel (0 to 191) occurred during the measuring time.

The energy loss and Auger spectra consist of linear arrays of 32 bit integers, with 192 and 384 elements, respectively. Each element contains the number of times that the corresponding channel (energy) was triggered during the measurement time - note however that this value still needs to be multiplied by the energy loss and Auger divisors, respectively.

The coincidence spectra consist of a 384×192 matrix of 32 bit integers. Each element contains the number of times that a coincidence occurred between the corresponding energy loss and Auger channels.

The program *anal.btl* is for analysis purposes. Instead of using only the cluster center as a measure of the energy (channel number) of incoming electrons, it de-clusterizes the energy loss and Auger data, counting 1 count in each of the channels that fall in the cluster. In this way it is possible to get an indication of the crosstalk between channels. This program also records a time spectrum that is independent of the Auger channel (i.e., sums over all Auger channels), simply using a 0 to 127 element array for the time data, where each element corresponds to a 1 ns wide time bin.

6.5.2 PC software

The software on the data acquisition control PC must perform a variety of tasks, the most important of which are to control the data acquisition hardware, to control the transputers, to store, recall and graphically display spectra, and to communicate with the microscope control PC. This program should also be able to do the most often needed (or time-consuming) alignments automatically.

The program *ces.exe* performs all these tasks. It has been written in Turbo Pascal, mainly because of experience with this language in the Particle Optics Group. The tasks it performs will be described below.

Communication between PCs

Measurements will normally be controlled by the data acquisition control PC. However, several microscope variables that may need to be changed in the course of an experiment, are controlled by the microscope control PC. For example, the probe position needs to be varied for line scans or two-dimensional scans, and the central energy that falls on the Auger electron detector needs to be varied for energy spectra broader than the detector range.

The communication between the PCs is set up such that they exchange packets of data. Each packet contains a command, followed by a variable amount of data (depending on the command). Although in principle either PC can initiate a packet, which the other PC must send a reply to, up to now there has only been a need for the data acquisition control PC to initiate packets. Packets must be transmitted, and replies must be received, within a certain time, if not the communication was deemed unsuccessful. The advantage of this is that short interruptions (if the serial cable was unplugged for some reason) do not 'hang' either PC, and with a little luck running experiments continue when the connection is restored. The format of the packets is described in Table 6.2.

byte	1	2	3	4	L-3	L-2	L-1	L
function	packet length L		data word 1		...		data word N		checksum	

Table 6.2 Format of the data packets transferred between the data acquisition PC and the microscope control PC. All packets start with a word containing their length L (in bytes), followed by N data words (2 bytes each), and a checksum. The packet length L and the number of data words N are related via $L = 2 \cdot (1+N+1)$. The first data word contains a command or reply code, if additional data is required it follows in data words 2 to N. The minimum data length $N = 1$, and the minimum packet length $L = 6$. The checksum is the sum over bytes 1 to L-2, modulus FFFFh.

The hardware for the communication is the standard serial port that every PC has (which has that additional advantage that it is platform independent - should we ever switch to another operating system on either PC then only the software on that machine will need to be rewritten). For the low-level hardware in-out (IO) routines we have used a freely available package⁵.

Spectra file format

To store the spectra we have looked for existing standard formats that can contain different types of data. Our wishes are to store spectra of varying dimensions and varying data-size, including minimum and maximum values for the x and y axes, a title, labels for the axes, and the original file name and date. Unable to find a suitable existing format that meets these demands we have defined our own format, which is described in Table B.1 (in Appendix B).

Spectra display

Because there is a plethora of programs to display and manipulate spectra we have not paid too much attention to this feature. It was however felt that it is necessary to be able to view spectra

(graphically) from within the acquisition program in order to (interactively) tune the apparatus. We have used a commercial library of display routines⁶ to provide a simple means of displaying one-dimensional spectra either linearly or logarithmically, and to display two-dimensional spectra and to rotate these around any of the three axes.

For the off-line analysis we find Microsoft Excel and Microcal Origin the most practical programs for one-dimensional and two-dimensional spectra, respectively.

6.6 Automatic tuning procedures

There are three sets of delays that need to be tuned. The first set sets the width of the time window and the position of the Auger events relative to this window. The second set sets the position and width of the TDC enable window. The third set sets the width of the PCOS enable window and the position of the individual position channel signals relative to this window.

6.6.1 Time window search

To understand what needs to be tuned it is useful to look at the timing of the signals, see Fig. 6.7. The energy loss and Auger electrons leave the specimen at the same time, but due to differences in time-of-flight (TOF) they arrive at the detectors at different times. Furthermore the Auger electrons have a TOF that varies significantly with their energy and starting angle (see Chap. 2), indicated as ΔTOF .

Delays E2 and A2 each provide a delay that is variable between 346 and 668 ns. Their purpose is to compensate the differences between energy loss and Auger TOF so that Auger electrons fall in the time window E3 (started by the arrival of an energy loss electron). Because we want to keep this window as narrow as possible we need to tune E2 and A2 so that the time peak falls in the center of the narrowest window that can accept it.

Delay E4 finally serves to obtain a coincidence trigger signal which is time-referenced to the energy loss electrons, rather than to the Auger electrons. E4 should be slightly longer (5 ns) than E3.

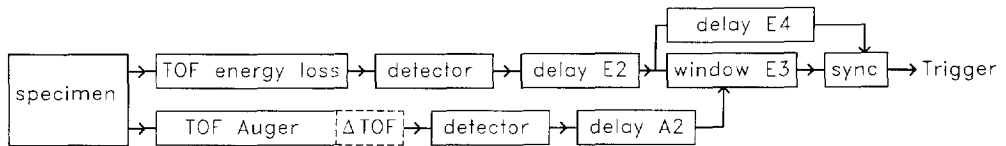


Figure 6.7 Time window tuning. Delays E2 and A2 should position the peak in the time spectrum in the center of the time window. The width of the time window is set by delay E3 and should be as narrow as possible while still containing the whole peak. Delay E4 serves to obtain a coincidence trigger signal which is related to the arrival of energy loss electrons, rather than to the arrival of Auger electrons with their varying TOF (indicated by ΔTOF).

To tune the delays we first need to record a time spectrum. Note that we cannot do this using the TDC, because the TDC is triggered by this section, and if the delays are not set correctly it will

6. Data acquisition system

not see anything. A further problem is that the TDC only sees about 20 ns, while we need to be able to search a 600 ns region. The way we do record the time spectrum is the following: we set E3 to its minimum value and E4 to a slightly longer value. We then sweep E2 and A2 over their whole range, counting the number of coincidences per second at each step of the sweep. The resulting time spectrum will consist of a background due to accidental coincidences (unrelated energy loss and Auger events), with a superimposed peak when the correlated events fall in the time window. The position and width of this peak are used to set E2 and A2, as well as E3 and E4. Because the minimum width of E3 (23 ns) is not negligible, we need to take this in to account when determining the delay values.

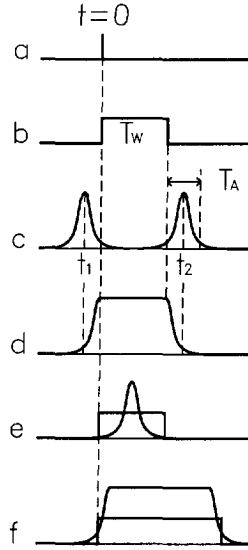


Figure 6.8 Coarse time window adjustment.

Figure 6.8 shows how we need to set the delays for the two possible cases: time peak smaller and time peak broader than the minimum window width. In (a) an energy loss electron comes in, defining $t = 0$. In (b) we see the time window E3 which is started by the energy loss electron. This window has (minimum) width T_w . In (c) we see two situations during the scan of E2 and A2: at $t = t_1$ the time peak just starts to fall in the time window, and at $t = t_2$ it almost leaves the time window. The width of the time peak is T_A . In (d) we see the measured time peak, which has a width $T_M = T_A + T_w$. In (e) we see the case that the time peak is narrower than the minimum time window ($T_A < T_w$). In this case we need to move the time peak to the center of the time window (to $t > 0$). In (f) we see the case that the time peak is broader than the minimum time window ($T_A > T_w$), in that case we need to widen the time window to $T_w = T_A$. The peak should again be moved to the center of the window.

6.6.2 TDC enable window

Again it is useful to first look at the signals involved, Fig. 6.9 continues from Fig. 6.7. If we see a coincidence in the time window E3 we wish to let the TDC measure the exact time difference between the energy loss and the Auger signals. Because E4 and E5, and A4 and A5, delay the energy loss, and the Auger signals, this is still possible.

To reduce the probability that the TDC measures the time between the wrong signals (an earlier energy loss event, for example) we only enable it when we expect both signals to arrive. On the other hand we do not want the TDC to miss any events that fall in the time window, so the TDC enable window should fall over the time window, (relatively) starting slightly earlier, and finishing slightly later. In this way the timing information should always be present.

The TDC enable window is shaped by delays D6 and D7. Delay D6 is the hold-off before the TDC is enabled and D7 is the width of the TDC enable window.

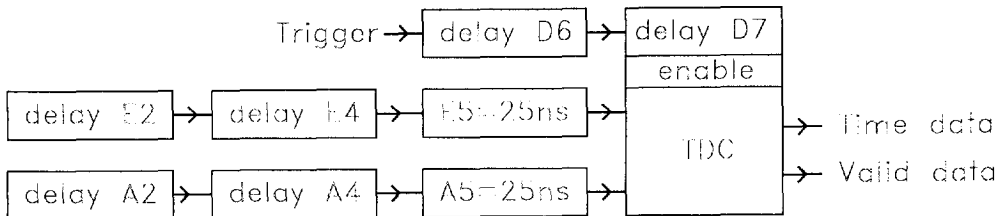


Figure 6.9 TDC enable window. Delay D6 determines the delay before the TDC is enabled after a coincidence trigger and delay D7 determines how long the TDC remains enabled. Delays E5 and A5 provide an extra delay of the timing signals so that these are still available when the TDC is enabled. The 'valid data' signal from the TDC indicates that it has seen both the energy loss and the Auger signals.

To tune the delays we again first need to record a time spectrum. In this case we do that by setting the TDC enable window D7 to a slightly larger (3 ns) width than the coarse time window E3, sweeping its position with D6, and counting the number of TDC-valid-data signals per second at each step of the sweep. Note that we should not set D7 to its minimum width: we would then never be able to catch Auger events that arrive more than this width after an energy loss event. The correct setting of D6 is simply to the center of the peak of the TDC valid data signal.

Note by the way that the reason to tune delay D6, and not just calculate it from the values of the other delays, is that it not only depends on other delays (which we have calibrated and know accurately), but also on the lengths of the coaxial cables interconnecting the units of the data acquisition system. We have labeled all cables, but should one cable accidentally be substituted by a cable of a different length the delays will change. We have about 1 ns accuracy in all timing signals, this corresponds to 0.2 m of coaxial cable. Delay D7 on the other hand only depends on E3, which has accurately been calibrated and is independent of cable length.

6.6.3 PCOS enable window

The PCOS enable window serves to latch the status of all position channels (192 energy loss and 96 Auger) if a trigger occurs. At the end of this signal the PCOS system will encode the channels that were triggered, resulting in a stream of cluster widths and centroids. Again we start by looking at the delays involved, see Fig. 6.10.

All 192+96 delays should be set so that the position information from the detector channels arrives just in the PCOS enable window. Because the energy loss TOF variation is negligible, all 192 energy loss delays will be set to the same value. For the Auger channels there can be a significant TOF variation, Auger electrons that have a higher energy will have a shorter TOF so their delay should be set to a longer value. The delays can however only be set per group of 32 adjacent channels, so the PCOS enable window will have to be wide enough to accept the largest TOF variation between 32 channels.

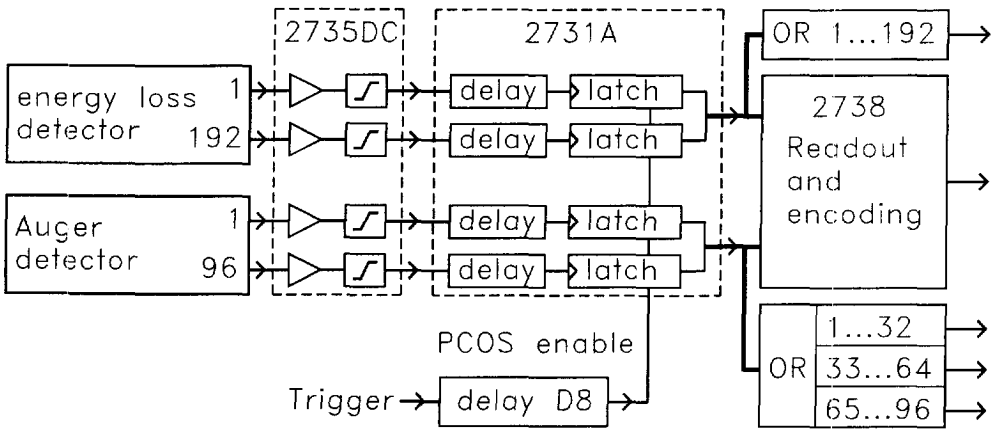


Figure 6.10 PCOS enable window. The 192 energy loss channels and the 96 Auger energy channels are each pre-amplified, discriminated, and delayed. If the signal from a channel comes in while the PCOS enable signal is present it will clock a '1' in its latch. The PCOS enable signal is started by the coincidence trigger and lasts for a time set by delay D8. The outputs of all energy loss latches are OR-ed, providing a '1' if at least one energy loss channel is triggered. The same is done for the Auger channels, except that they are OR-ed per 32 channels.

To tune the delays we set the PCOS enable width D8 to its minimum value and sweep all delays simultaneously. We count the number of OR-ed energy loss signals per second in each step of the sweep, and do the same for the three OR-ed Auger signals. If all is well each of these four time spectra will display a peak, we set the channel delays to the value where the peak started to rise, and set the PCOS enable window D8 to the width of the widest of the four peaks. In this way all position signals should fall in the PCOS enable window.

6.6.4 Peak find routine

Because we wish to automate the tuning procedures, we need routines to let the software automatically find the (time) peaks in the spectra. We have however not yet been able to find a 100% reliable algorithm, so we display the spectrum, together with the position and width of the peak that the software found, and ask the user to confirm or edit these values.

The first peak finding algorithm we tried fitted a background and a Gaussian peak to the spectrum (so it had four parameters: background level, Gaussian peak position, width, and amplitude) but the problem is that you tend to end up with a peak with the width of your total spectrum, which compared to $t = (-\infty, +\infty)$ is in a way true.

What we do now is to look for points in the spectrum that are more than several times the standard deviation above the average of the graph. If several adjacent points have this property, they constitute a peak. The largest peak (in volume) is assumed to be the peak we are looking for. The implementation is as follows: we start at both edges of the spectrum, calculating an average and a standard deviation over the first five points from both sides (so the peak should not start in this area). If the next point is below a fudge factor (we use 2.0) times the standard deviation we add it to the background and recompute the average and the standard deviation, if its not we add it to a series (peak). In this way the peak is not included in the calculation of the average and the standard deviation.

We estimate the standard deviation as $s^2 = \Sigma(Y_i - \bar{y})^2 / (N - 1)$, where Y_i ($i = 1$ to N) are the N data points, and $\bar{y} = \Sigma Y_i / N$ is the estimated average. To compute a moving standard deviation we use the relation $\Sigma(Y_i - \bar{y})^2 = \Sigma Y_i^2 - 2\bar{y}\Sigma Y_i + \Sigma \bar{y}^2$, substitution of the average in this equation leads to $s^2 = [\Sigma Y_i^2 - (\Sigma Y_i)^2 / N] / (N - 1)$.

6.7 References

1. *Coincident Electron Spectroscopy at nm scale (CES)*, project description DO-ISO-HF collaboration, Department of Applied Physics, Delft University of Technology, Delft, the Netherlands (1993), unpublished.
2. *Hardware description of the 2TP_VME_LA module*, Electronic department NIKHEF-H, Amsterdam (1990).
3. *HSM 8170 Triple port high speed memory instruction manual*, Creative Electronic Systems S.A., Route du Pont-Butin 70, CH-1213 Petit-Lancy 1, Geneva, Switzerland.
4. J. Westerman, *Realisatie van een meetprogramma m.b.v. transputers t.b.v. het C.E.M.-project*, thesis Hoger Technisch Onderwijs, Rotterdam, the Netherlands (1992), unpublished.
5. M Schultz, *ASYNC11 - Interrupt-driven asynchronous communications for Turbo Pascal*, Version 1.1 (1989), Copyright © 1989 Rising Edge Data Services.
6. Quinn-Curtis, *Library of Turbo Pascal numerical and graphical routines* (1992).

7 Measurements

7.1 Introduction

This chapter describes the first experiments that were performed with the Auger microscope. The first part considers the illumination of the specimen by the primary beam. Next we present data on Auger and EELS spectroscopy (on different materials) as well as results of mapping of a specimen using secondary electrons. We conclude with a coincidence experiment on carbon.

7.2 Characterization of the primary beam at the specimen position

Probe size

During the design phase the, somewhat ad hoc, specifications for the focussed electron probe were set to be as a 1 nm diameter beam with a 1 nA current (Kruit *et al.*¹). The actual probe size has been determined experimentally by scanning the beam from a hole in a carbon foil onto the foil itself. The resulting change of the secondary electron signal is shown in Fig. 7.1.

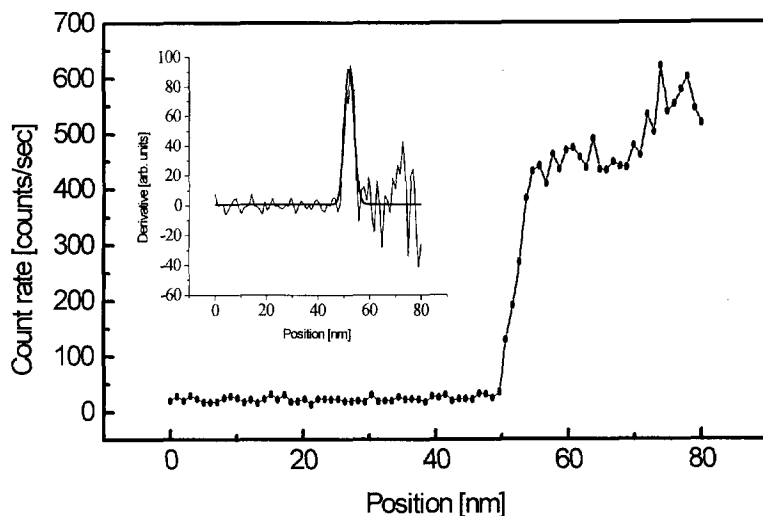


Figure 7.1 Line scan from a hole in a carbon foil (left) to the foil itself (right). The signal results from secondary electrons (of about 5 eV energy) that are generated in the carbon foil. The inset shows the derivative of the same signal with a Gaussian fit. The line scan demonstrates a probe size of about 4 nm.

7. Measurements

Depending on the definition for the spot size, we find that the signal rises from 10% to 90% of the final intensity in 3.5 nm. The increase in noise when the beam is positioned on the carbon foil, as seen in the right part of Fig. 7.1, may result from corrugation of the foil. An alternative approach is based on differentiating the line scan and fitting a Gaussian through it (shown in the inset of Fig. 7.1). Then we find a beam profile with a full-width half-maximum of 4.0 nm.

Spot size	C2 aperture [μm]	Spot diameter [nm]	Beam current [pA]
Spot 1 C1 = 0.34 A C2 = 1.31 A	<none> (C2 = 1.27 A)		160000
	70	27	3200
	30	14	420
	10	9	44
Spot 2 C1 = 0.41 A C2 = 1.05 A	<none> (C2 = 1.03 A)		60000
	70	20	450
	30	15	60
	10	11	15
Spot 3 C1 = 0.51 A C2 = 0.94 A	<none> (C2 = 0.95 A)		10000
	70	15	120
	30	13	18
	10	10	5
Spot 4 C1 = 0.69 A C2 = 0.88 A	<none> (C2 = 1.03 A)		2400
	70	17	14
	30	17	7
	10	11	2
Spot 5 C1 = 1.11 A C2 = 0.85 A	<none> (C2 = 0.97 A)		280
	70	18	5
Spot 6 C1 = 1.62 A C2 = 1.00 A	<none> (C2 = 0.99 A)		80
	70	9	3

Table 7.1 Probe size and probe current as a function of the C1 excitation and the C2 aperture (C2 is used to focus the beam to a spot, or to maximize the beam current if no aperture is present).

These probe sizes are routinely obtained and are definitely smaller than found in a conventional Auger microscope. In fact, they are only comparable to those found in a dedicated instrument².

The additional elements in the primary beam (the pre-deflector and the Auger electron deflector) do not affect the probe size.

Probe current as a function of size

The count rates in both the Auger and EELS spectra are of course directly related to the current in the probe. Table 7.1 summarizes the probe size and the probe current for different settings of the condenser lens and different apertures.

The probe sizes in Table 7.1 were estimated by eye from the fluorescent screen while the beam was focused on a thin part of the specimen. Our experience is that the eye tends to overestimate the probe size by a factor of about two, because it cannot handle the high dynamic range between the actual spot and the tail of the spot. The current in the beam was measured using an electrometer connected to the specimen holder while the beam was focused on the (thick) support grid. The specimen was at a positive voltage to attract secondary electrons which might otherwise have escaped.

The values in Table 7.1 indicate that the geometric probe size is only small compared to the total probe size (because, given the brightness of the electron source, we should otherwise have more current). We have the feeling that the present probe size may be affected by mechanical vibrations or electronic instabilities, which we hope to correct in the near future.

Source brightness

The brightness of the Field Emission Gun was also determined. For this we use the fringe method as proposed by Fransen *et al.*³. The result is a brightness of $5 \cdot 10^6 \text{ A m}^{-2} \text{ srad}^{-1} \text{ V}^{-1}$. This value is of the same magnitude as the one given by Mul *et al.*⁴ for a similar source.

Specimen drift

Apart from the beam characteristics also the stability of the specimen position is relevant: we would like to position the beam at a selected part of the specimen and to be able to study this area for some time without it drifting away. The specimen position in the plane perpendicular to the primary beam is controlled with a piezo stage which is used in two modes:

- Rough (discrete steps) repositioning is done using the slip-stick principle, in this case we observe a large drift of the specimen directly after repositioning (piezo creep). After about 10 seconds the stage has settled.
- Fine (continuous) positioning is done by applying an offset voltage on the piezos, the drift is in this case in the order of 1 nm minute^{-1} . This implies that, at the moment, the drift becomes comparable to the spot size only after several minutes, and only in cases where a complete area is scanned, may specimen drift still be a problem.

We have measured the drift of the stage by recording TEM images with a CCD camera at five minute intervals. Three easily recognizable features on the specimen were followed, the inset in Fig. 7.2 shows how these features moved with time. From this inset the total drift (distance between successive points in the inset) has been calculated, this is shown in Fig. 7.2 itself.

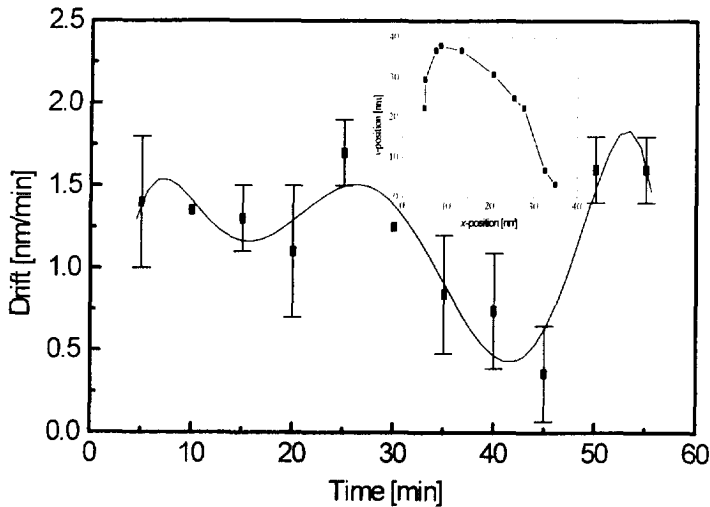


Figure 7.2 Specimen drift over a 55 minute period. The inset shows the specimen position as a function of time; the points are 5 minutes apart.

7.3 Auger spectroscopy

Experimental setup

Since no parallel detector was available yet all experiments were done using the timing output of the micro channel plate that was placed behind the exit slit of the energy analyzer. In all experiments the specimen was held at a potential of -240 V and the Auger electron deflector was at $+60\text{ V}$, so the electrons were accelerated 300 eV before entering the deflector.

The parallelizer coil current was set to give maximum count rate at the detector. The central energy of the Auger electron deflector was always chosen so that the energy range of interest could pass. The potentials of the seven-electrode transport lens were set according to the values from computer simulations (van der Stam⁵), interpolating between the nearest simulation results, and then manually adjusted for maximum count rate at a given energy. This often resulted in a much lower potential of electrode 2 and electrode 6, which means the lens effect both at the entrance and the exit was stronger than calculated. We are uncertain why this gives better results. The width of the entrance slit of the hemispherical analyzer was between 1 and 2 mm, the exit slit was opened to roughly the same value.

Results

The Auger spectrometer has been used to measure both secondary electrons (with an energy of only a few eV) and real Auger electrons resulting from core-hole excitations (and having an energy up to about 1 keV). There are two modes of operation. Firstly, we can perform energy

scans with the (focused) beam on a particular spot. Secondly, the focused beam can be scanned over the surface and electrons of a specific (and fixed) energy can be used to create an (element specific) map.

Energy scans

We have obtained energy scans in the energy window between 0 and 1 keV, with the primary beam focused to a spot with a diameter between 3 and 10 nm. In this way we were able to measure the secondary electron signal and to identify the Auger edges of the following elements: carbon (KLL-edge, 265 eV), silver (MNN-edge, 355 eV), titanium (LMM-edge, 381 and 416 eV), oxygen (KLL-edge, 503 eV) and nickel (LMM-edge, 707, 772 and 844 eV).

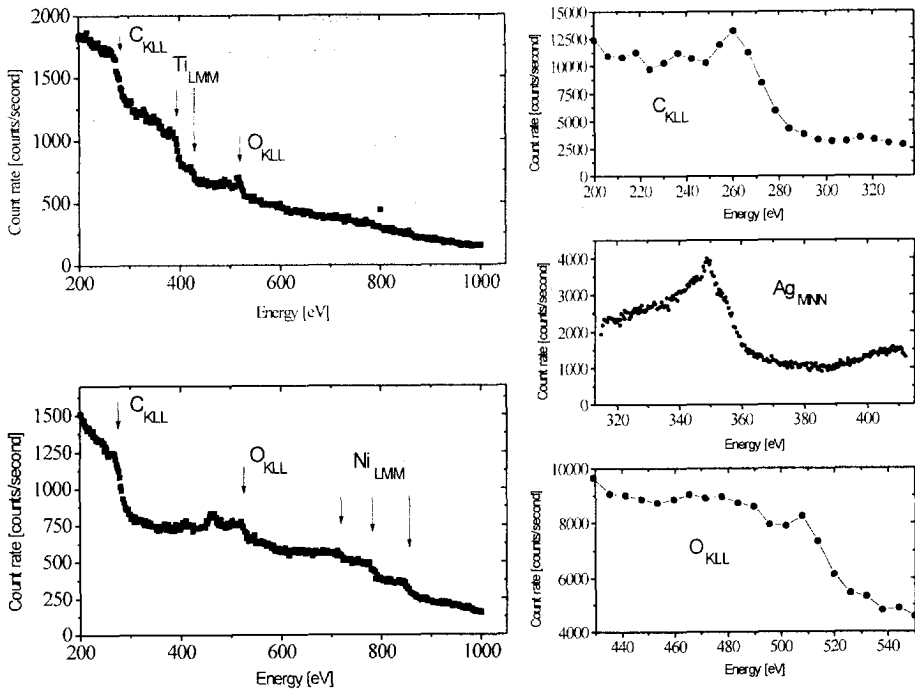


Figure 7.3 Auger spectra of titanium and nickel showing a wide range of energies. To the right the Auger edges of carbon, silver and oxygen are shown in more detail.

Figure 7.3 is a display of the various Auger lines. These spectra were observed without special preparation of the specimen and indicate that the present vacuum is sufficient for identification of elements. The materials were chosen because we expect to use them in future experiments or because they are of interest from a material science point of view. We do have the feeling that other elements are measurable as well provided that their Auger edges are not too high (above 1.5 keV). This implies that the Auger lines of most elements are within the reach of our instrument. It is also noted that valence band transitions (LVV, MVV) occur at relatively low

7. Measurements

energies (< 100 eV) and that they are of special interest because of the relation to the band structure of materials; these energies of course can easily be measured for all elements.

Mapping

Using the signal of the (tuned) Auger spectrometer we have mapped several geometries. Using secondary electrons we obtained images of a carbon film with gold islands. Since the secondary electron yield of gold is higher than that of the carbon support the islands appear as bright areas, see Fig. 7.4. By resolving these small gold clusters (with a diameter smaller than 10 nm) we demonstrate the spatial resolution of the microscope.

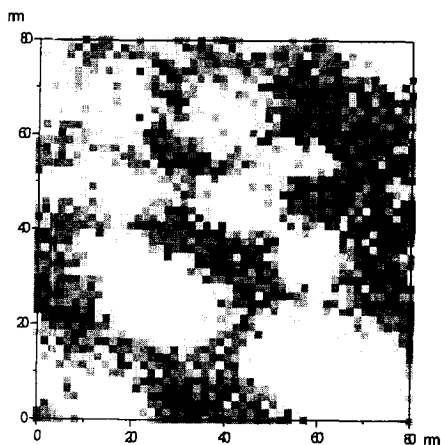


Figure 7.4 Secondary electron image of small gold clusters (bright) on a carbon foil (dark). The smaller gold islands are only 10 nm across, demonstrating a resolution in the order of a few nanometers.

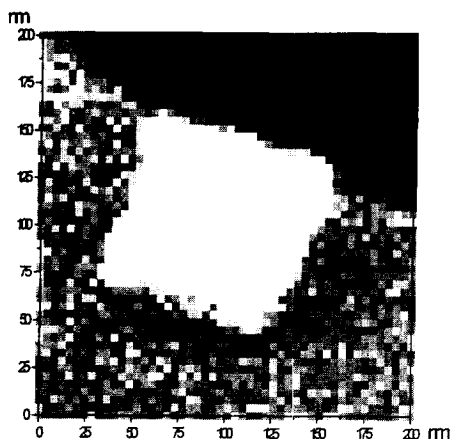


Figure 7.5 An MgO cube (bright) on a carbon foil (gray); the upper right part is a hole in carbon foil (dark). The image is obtained using oxygen Auger KL electrons with an energy of 500 eV.

Figure 7.5 displays a MgO cube on a carbon support using oxygen (KLL) Auger electrons. The signal rises in about one pixel (4 nm) and this map again illustrates the spatial resolution, now in elemental mapping. In other experiments we have also mapped MgO cubes using secondary electrons and carbon (KLL) Auger electrons. These experiments show that the Delft Auger Microscope can be used for scanning electron microscopy and scanning Auger microscopy (element mapping) with nanometer resolution.

Quantitative information from Auger spectra

A MgO cube on a carbon foil provides an interesting system that allows us to extract more quantitative information. Using the serial detector, we scanned the beam four times over a MgO cube. The detector was tuned at the carbon KLL-edge (265 eV) and the corresponding background signal was obtained at a somewhat higher energy (295 eV). Similarly the oxygen

KLL-edge (at 500 eV) and the background signal (530 eV) were measured. For both the carbon and the oxygen we then calculated $(I_{edge} - I_{background}) / (I_{edge} + I_{background})$ at each position in the line scan. In this way we obtained the intensity of the Auger edges as a function of the position; the algorithm also removes topographic effects from the data. The reduced data are shown in Fig. 7.6 and give a relative measure for the carbon and oxygen content in the cube and the foil.

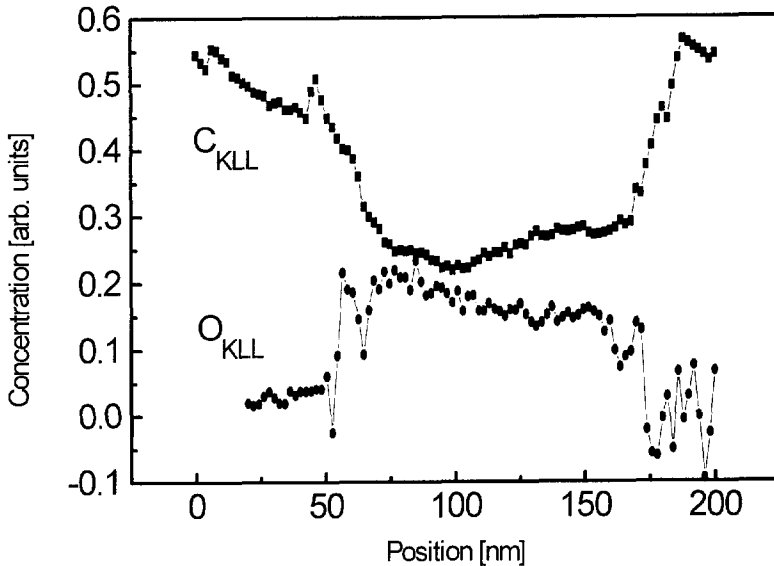


Figure 7.6 Carbon and oxygen concentration in a line scan over a MgO cube on a carbon foil. The carbon content drops when the beam moves from the foil onto the MgO cube (center part) and later rises again on the foil. The intensity of the oxygen KLL line is maximal at the position of the MgO cube.

On the MgO cube the intensity of the carbon line drops to about 50% of the value on the foil. At the same time the oxygen content increases: it scatters around zero on the carbon foil and increases at the position of the cube. A zero order approximation can be used to quantify the carbon signal (using the intensity at the carbon foil as a reference). Assuming the thickness of the carbon foil to be of the order to 5 to 10 nm the change of intensity implies a thickness of the carbon layer on the MgO cube of about 3 to 5 nm or 10 to 15 monolayers. Given the vacuum conditions, and the mobility of the carbon atoms due to the elevated temperature in the electron beam, this value seems reasonable. Unfortunately there is not such a gauge for the intensity change of the oxygen line. As a general remark, however, one would expect a larger change of the relative carbon and oxygen content if the specimen were more clean. From Fig. 7.6 it can also be seen that the lateral resolution in these experiments is 10 to 15 nm (the width of the 10%-90% intensity interval). This value is worse than the previously obtained resolution, due to drift of the specimen between the different energy line scans.

7.4 Energy loss spectroscopy

The energy loss spectrometer, in combination with the post-spectrometer optics (Brink⁶), still awaits the installation of a parallel detector. It can, however, be operated with the conventional slit, scintillator, and photo multiplier combination acting as a serial detector. For this the post-spectrometer optics are tuned in such a way that as much signal as possible arrives at the slit-scintillator position. A spectrum is then obtained by making a standard scan with the spectrometer magnet. When the zero-loss peak was part of the spectrum, the scan was made starting at the maximum energy value and going back. In this way the 'blinding effect' of the zero-loss peak on the scintillator was reduced as much as possible. The slit-width was adjusted to give both sufficient spectral resolution (typically of the order of 1 eV) and a high count rate.

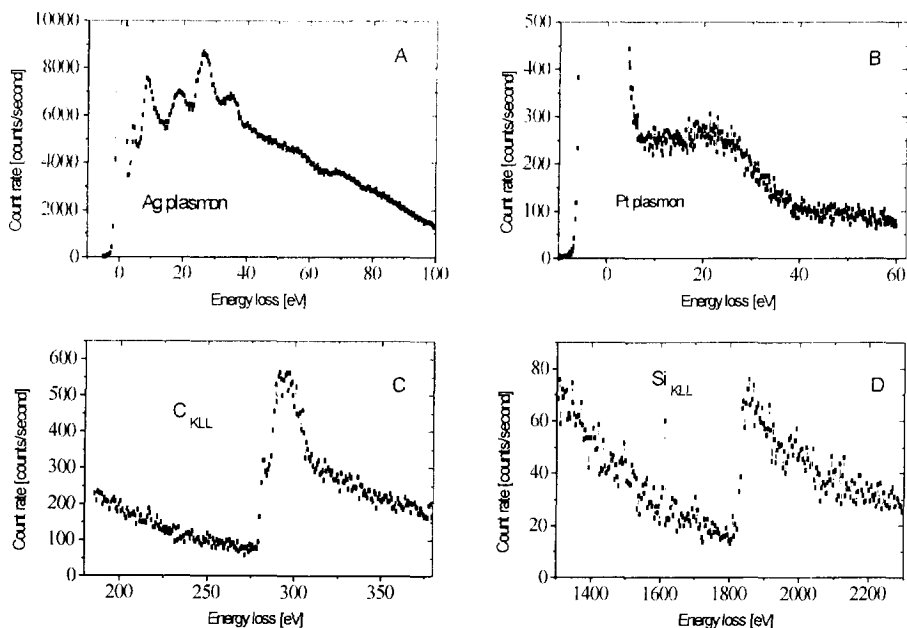


Figure 7.7 Low-loss (plasmon) energy spectra of silver (A) and platinum (B). The lower two graphs show the carbon (C) and silicon (D) KLL-edges.

Figure 7.7 shows low-loss (plasmon) spectra of platinum (A) and silver (B). The performance of the energy loss spectrometer is further illustrated in the lower two graphs, showing the carbon KLL-edge of carbon (C) and silicon (D). The jump ratio (intensity of the K-edge with respect to the background) is 10 and the π^* edge (the small peak close to the main edge) is well resolved. According to its specifications a jump ratio of (at least) six should be obtainable and the observation of the π^* indicates an energy resolution of the order of 1 eV (as expected from the specifications). Also, the silicon KLL-edge at a much higher energy is well visible. Based on these data we think that our energy loss spectrometer behaves according to expectations.

7.5 Coincidence Spectroscopy

7.5.1 CES test measurements

We first tested the CES data acquisition system separately from the microscope. To simulate the coincidence experiment we have positioned a radioactive source emitting pairs of α -particles between two photo multipliers. This leads to single pulses from the photo multipliers when only one of the α -particles is detected, and coincidences when both are detected. We have connected one photo multiplier to a single energy loss channel, and the other photo multiplier to a single Auger channel. Figure 7.8 shows the result of this experiment.

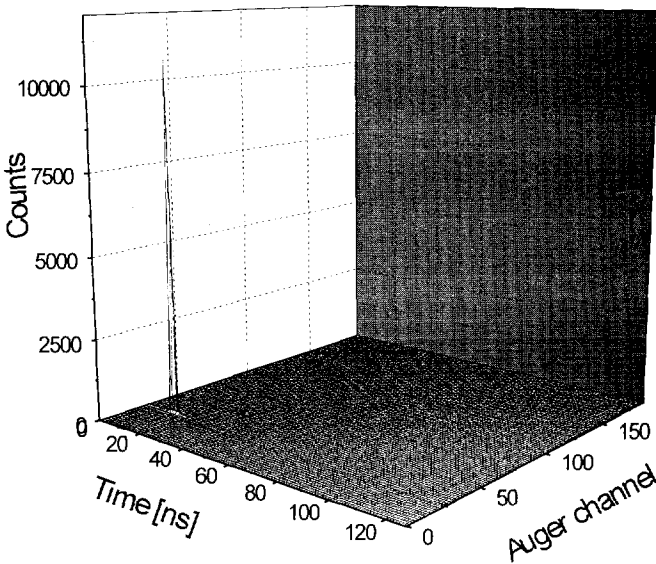


Figure 7.8 Test of the CES data acquisition system using two photo multipliers and a radioactive source. The time peak is within the 1 ns resolution of the TDC, and there is no crosstalk between the Auger channels.

7.5.2 Time spectrum

With both the Auger and the EELS spectrometer in working order the field of coincidence spectroscopy is in principle available as well. Because the CES electronics were still under development, the first experiments have been performed using a time-to-amplitude-converter (TAC), an analog-to-digital-converter (ADC), and a histogrammer. The first step in a coincidence experiment is the experimental determination of the time window. Electrons that are physically correlated (i.e., the energy loss electron and the resulting secondary or Auger electron) should arrive within a certain time window to be interpreted as the result of a coincident event.

7. Measurements

Before the timing is done, both the pulses in the Auger and the energy loss channels are shaped using constant fraction discriminators. Then, the time window is obtained using a time-to-amplitude converter; pulses from the energy loss spectrometer serve as the start- and those from the Auger spectrometer as the stop-signal. A typical time spectrum obtained in this way is shown in Fig. 7.9. The energy loss spectrometer was tuned at the plasmon peak while the Auger detector was set at the secondary electron peak; these energies are chosen on purpose for their high count rates (measurements on a thin carbon foil).

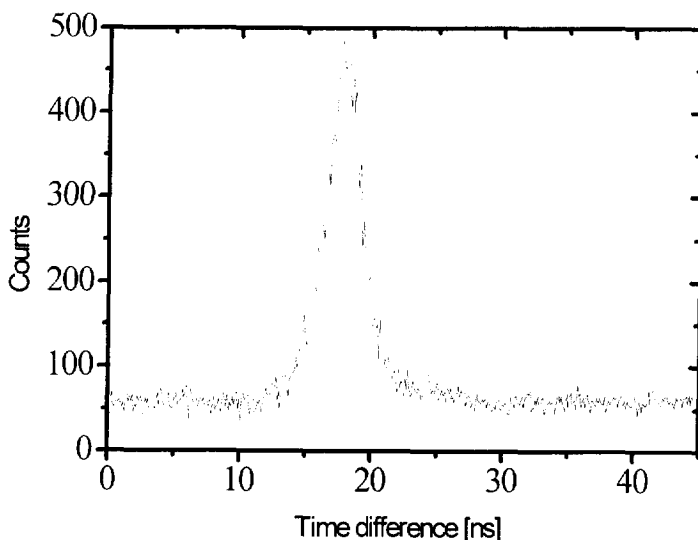


Figure 7.9 Time spectrum in a coincidence experiment; start signals from EELS electrons at the plasmon energy and stop signals from secondary electrons. Measurements on a thin C foil.

From Fig. 7.9 it can be seen that the electrons that are potentially interesting in a coincidence experiment arrive in a time window which is about 5 ns wide. The time difference between the start and stop pulses depends on the energy of the Auger electrons under study; on top of that there is an arbitrary offset given by the lengths of the cables before the signals enter the time-to-amplitude converter. Once the peak in the time spectrum has been found, it is considered to be fixed and a time window around it is used to discriminate between true and false coincidences (a count in the energy loss channel is considered to be a true coincidence when also a count on the secondary electron detector was detected in the selected time window).

A complete set of experiments then consists of a coincident energy loss spectrum, a non-coincident one, and their ratio. The latter is a measure for the probability that a secondary electron is created by an energy loss equal to the EELS energy. Figure 7.10 displays such a set of spectra: standard energy loss (A), coincidence (B), and ratio spectrum (C), respectively.

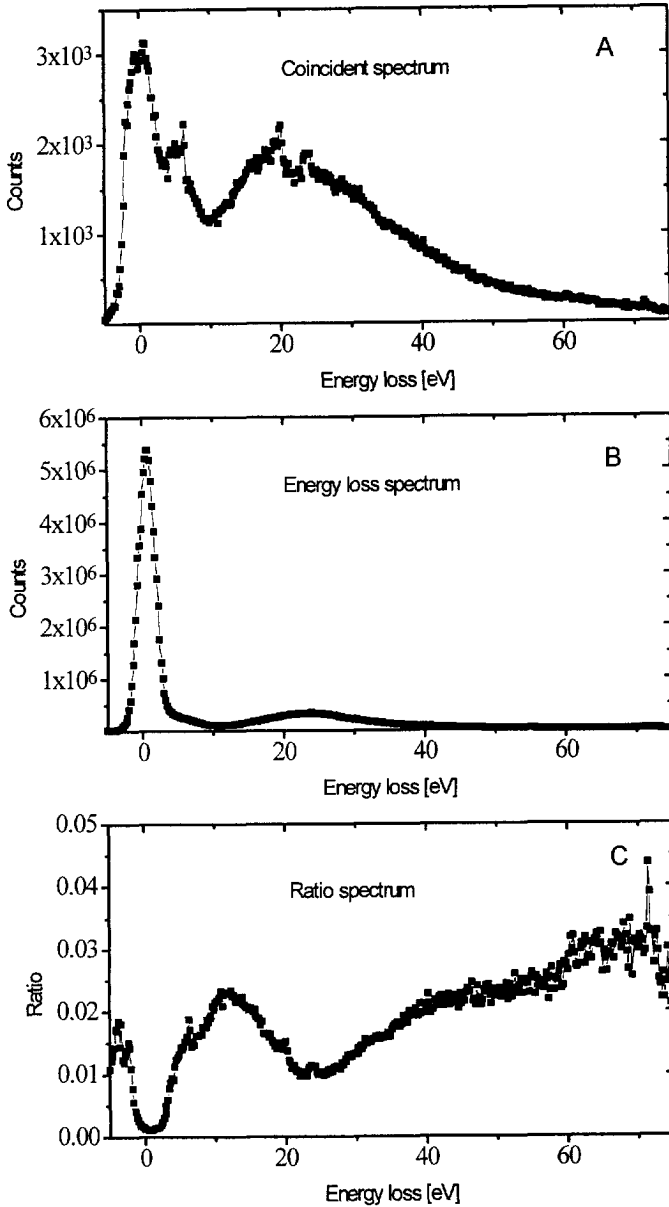


Figure 7.10 Coincidence spectrum (A), energy loss spectrum (B), and the ratio of these at each energy loss (C).

7. Measurements

These three spectra can be interpreted as follows. The coincident energy loss spectrum in Fig.7.10.A shows a kind of zero-loss peak, which is due to false coincidences. Of course coincidences at an energy loss equal to zero are impossible, but due to the high number of electrons in the zero-loss peak the probability for a false coincidence is relatively high, which explains the peak. The broad structure around 25 eV is due to bulk plasmons. The conventional energy loss spectrum in Fig.7.10.B shows similar features as the coincident one in Fig. 7.10.A, the major differences being that the zero-loss peak is now fully developed, and that the signal is less noisy due to the much higher count rate.

As can be seen from the ratio spectrum in Fig.7.10.C the generation rate for secondary electrons is higher at energies around 15 eV than close to the bulk plasmon energy of carbon. The energy of 15 eV suggests a relation with surface plasmons since these appear at lower energy losses ($E_{\text{surface plasmon}} = E_{\text{bulk plasmon}}/\sqrt{2}$). Apparently the decay of surface plasmons forms an effective channel to produce secondary electrons. The gradual increase of the generation rate at increasing energy losses (as seen between 30 and 70 eV) is consistent with the concept of stopping power. This predicts that more secondary electrons are produced when a larger energy loss is experienced. The results as presented here reproduce the findings of other experiments: Pijper and Kruit⁷, Müllejjans and Bleloch⁸, and Scheinfein *et al.*⁹.

7.6 Data acquisition system performance

Maximum single rates

The timing signal from the Auger MCP exit plane was pre-amplified by a VT110 pre-amplifier, was discriminated by a CF4000 constant fraction discriminator, and was fed to the timing input of the CES data acquisition system. The divisor was set to 1 to obtain the highest rate in the system. We used the *ces.bit* transputer program which can handle all four types of spectra (so not a special test program optimized for high single rates). The measurement time was 60 s, and this time was long enough to prevent start-up effects due to buffering. We triggered only one position channel and the PCOS-enable window was 40 ns wide. The reject options were disabled, the watchdog was enabled (so events were rejected if they were not accepted within $\pm 10 \mu\text{s}$ by the buffer memory).

At the highest count rate that the system could handle we had $3.25 \cdot 10^6$ counts on the hardware counter, and the transputers counted $2.8 \cdot 10^6$ events (so 14% of the events were rejected because the buffer memory was full and could not be emptied because the transputers were still calculating). This means that $4.7 \cdot 10^4$ events per second is the highest singles rate that the system can handle, with the divisors set to their maximum value of 256 we should be able to handle $1.2 \cdot 10^7$ single events per second. This is well within the specification of 10^6 counts per second per detector.

Although the energy loss detector is not yet ready we can expect the same maximum values because it also based on an MCP. Connecting the Auger signal to the energy loss input (of course) resulted in identical maximum rates.

Maximum coincident rates

Normally only a fraction of the Auger and energy loss signals is coincident, to measure the maximum rate of coincidence events we have connected the Auger timing signal to both the Auger and the energy loss timing inputs - in this way all events are coincident (after the delays have been tuned). The transputers used the program *ces htl*.

First of all we measured a time spectrum. In this case the maximum rate we could handle was $4 \cdot 10^4$ events per second on the rate-meter. We let the system measure for 60 s to prevent start-up (buffer) effects. During the first try the transputers locked up after 30 s (we are not sure why), the second attempt succeeded. The counters showed $2.7 \cdot 10^6$ energy loss, Auger, and coincidence events and $2.1 \cdot 10^6$ valid data signals from TDC. This indicates that the TDC enable window was perhaps not perfectly tuned. The two-dimensional spectrum (time and Auger energy) from the transputers contained $1.7 \cdot 10^6$ counts in one single peak, so 37% of the events were rejected because the buffer was still full (the reject options were disabled, so also events without valid TDC data were sent to the transputers). This means that the system can handle $2.8 \cdot 10^4$ coincidence events per second - while measuring a time spectrum.

Measuring a coincidence spectrum is different because the transputers now have to apply a time window to each event. By using a look-up table which accepts any time and by enabling all reject options we ensured that the transputers had to accept all events, and consequently had to handle the highest rate possible. Doing this we found that in 60 s the transputers accepted $1.7 \cdot 10^6$ events out of $2.1 \cdot 10^6$, so they rejected 22% and handled $2.8 \cdot 10^4$ events per second, which is close to the $5 \cdot 10^4$ that we aimed for in the design.

7.7 References

1. P. Kruit, W.Th. Wenckebach and C.W.E. van Eijk, *Coincidence electron spectroscopy with nanometer scale resolution*, project proposal FOM/STW - Technische Natuurkunde en Innovatie (1991), unpublished.
2. J. Liu, G.G. Hembree, G.E. Spinnler, and J.A. Venables, High resolution Auger electron spectroscopy and microscopy of a supported metal catalyst, *Surf. Sci. Lett.* **262**, L111 (1992).
3. M.J. Fransen, E.P.N. Damen, C. Schiller, T.L. van Rooy, and H.B. Groen, Extraction of source parameters from point projection microscopy images, *Proc. of the International Field Emission Symposium*, Wisconsin, USA (1995).
4. P. Mul, B.J.H. Bormans and M. Otten, Design of the CM20 FEG, *Philips Electron Optics Bulletin*, **130** (1991).
5. M.A.J. van der Stam, J.E. Barth and P. Kruit, Design of a multi mode transport lens with optimization program SOEM, *Proc. SPIE conference on Charged-Particle Optics*, W.B. Thompson, M. Sato, A.V. Crewe, Eds., SPIE - The International Society for Optical Engineering, Bellingham, **2014** (1993), 45-56.
6. H.A. Brink, *The Post EELS Optics*, masters thesis Delft University of Technology, The Netherlands (1995), unpublished.
7. F.J. Pijper and P. Kruit, Detection of energy-selected secondary electrons in coincidence with energy-loss events in thin carbon foils, *Phys. Rev. B.* **17** (1991), 9192-9200.

7. Measurements

8. H. Müllejans and A.L. Bleloch, Ratio between the energy-loss spectrum in coincidence with secondary electrons and the normal energy-loss spectrum for thin carbon films in the carbon K-edge region, *Phys. Rev. B.* **46** (1992), 8597.
9. M.R. Scheinfein, J. Drucker and J.K. Weiss, Secondary-electron production pathways determined by coincidence electron spectroscopy, *Phys. Rev. B.* **47** (1993).

Appendix A - Alignment procedures

Introduction

The optics of the microscope can be divided into three groups: the illumination optics, the energy loss analysis optics, and the Auger electron energy analysis optics. The energy loss system alignments can be found in the manual of the spectrometer¹ and in the thesis of Brink², which describes the post spectrometer optics. The alignment procedures for the illumination optics and the Auger electron analysis optics are given below.

It is important to realize that alignment is not a one-pass process but an iterative cycle: after having performed all alignments it is likely that some of the first alignments should be done again (because they can be adjusted better now that the whole system is more aligned).

A.1 Illumination optics alignment

The illumination system should be aligned from the gun to the specimen and that is the order in which the alignments are presented here. Some of these alignments are standard microscope alignments and can also be found in the EM430 Operating Instructions³, in the book of Chescoe⁴, and the article by Sell⁵. Other alignments are specific to our microscope, for instance the alignment procedure of the Auger electron deflector.

A.1.1 Getting light

The first step is to get light on the viewing screen. Unless the microscope is seriously misaligned, this should not be a problem. If no light is visible first perform the following checks, before trying to realign the system (and possibly ruining the current alignment):

- 1) Is the high tension on, and at 100 keV? Note that the HT cannot be switched on if one of the safety checks fails, the most common problems are: not enough pressure in the HT tank and in the FEG electronics chamber (must at least be 4 bar), a closed valve (V7, between the gun and the specimen chamber or V4, between the specimen chamber and the viewing chamber), no lead shields on specimen chamber viewing ports, too warm cooling water, or cooling water not running.
- 2) Is the beam not blocked? Try moving the specimen stage and removing the apertures.
- 3) Check the C1, C2, and objective lens settings, try varying the C2 current. For most settings the currents should be 0.5 to 1.5 A, 1 to 2 A, and 11 to 12.5 A, respectively.
- 4) Is the FEG on, and is there an emission current (10 to 50 μA)? Note that after having been switched off for a day or longer the FEG needs about 24 hours to get back to full emission. Very low emission in first few hours is normal (the chamber warms up slowly, and the emission is an exponential function of the temperature).
- 5) Do all other lenses and the deflectors receive current? Check that the P80 system is switched on and that all cables are plugged in.

If all the above is OK but you still do not see light successively try the following:

- 1) Remove the specimen and the apertures.
- 2) Degauss the Auger electron deflector and - if possible - try to switch it off completely.
- 3) Restore a set of saved settings (known to have worked) for the P80 system, or delete the file *augertem.sav*, so the program will use the build-in defaults.
- 4) Turn all alignment knobs on the microscope to their middle position, or unplug deflection coils and stigmators.
- 5) Use a radiation (X-ray) detector to try to detect the radiation generated by the beam. Good places (radiation leaks) are stainless steel covers for unused ports and especially the viewing screens (fool the interlocks on the radiation shields with a piece of scotch tape). If you cannot measure radiation, try moving the beam around with the gun tilt alignment. If you do measure radiation, you should be close to getting light on the viewing screen.

A.1.2 Gun tilt and shift alignment

The purpose of this alignment is to aim the beam straight through the centers of the C1 and C2 lenses. Misalignment manifests itself by movement of the center of the spot on the viewing screen if the strength of either lens is varied. For a first alignment, remove the C2 aperture, for the final alignment an aperture must be inserted.

Procedure:

- 1) Choose a 'high' C1 setting, somewhere between 2 and 4. Focus the beam to a spot with C2. Move the spot to a known position on the viewing screen, for example the small circle in the middle, using the *beam* shift controls.
- 2) Choose a 'low' C1 setting, 1 to 3 positions lower than the previous setting. Refocus the beam with C2.
- 3) Maximize the intensity on the screen with the gun tilt controls.
- 4) Move the spot back to the position of step 1 using the *gun* shift controls. Repeat these last two steps to get maximum intensity at the spot position from step 1.
- 5) Repeat steps 1 to 4 until no further improvement is possible.

The trick is that in both step 1 and step 2 the gun image below the C1 lens (imaged onto the viewing screen with the rest of the lenses) is off-axis, but that in step 2, with a weak C1 setting, it is further from the axis. Moving it back to the position of step 1 is therefore in the direction toward the optical axis.

Note that due to remanent magnetism in C1 and C2 it is impossible to get this alignment perfect for all C1 and C2 settings. For this reason the alignment should be performed around those C1 and C2 settings that are also used in practice.

A.1.3 C2 aperture alignment

This aperture should be positioned in the center of the C2 lens. If this is not the case an off-axis part of C2 is used, and changing the C2 strength will result in movement of the spot on the viewing screen.

Procedure:

- 1) If no light is visible, move the aperture until there is (or choose a larger aperture to start with).
- 2) Focus the beam to a spot on the screen with C2.
- 3) Modulate the excitation of C2 with the left hand, and adjust the aperture position with the right hand until the spot center stays in the same place (so the spot grows and shrinks around the center). Readjust beam shift to keep light, if necessary.

A.1.4 Tilt pivot point alignment

The purpose of this alignment is to let beam tilt cause only tilt on the sample, and not also shift. This means that the tilt pivot points (where tilt- x and tilt- y deflect the beam) must coincide with the crossover (gun image) between the C2 lens and the objective lens: this crossover is the object that is imaged on the sample by the objective lens, all rays leaving an object from the same point will come together in the corresponding point in the image.

There are two ways to perform the alignment. The standard method is to adjust the position of the pivot points to match the position of the crossover (3b below). The other method is to adjust the position of the crossover (using C2) to match the pivot point position. To minimize the aberrations of the Auger electron deflector, we wish to have the crossover inside this deflector. It is however difficult to know the exact position of the crossover, while the position of the pivot point can be adjusted fairly accurately (within ± 10 mm). Using the second method, it is possible to align both the tilt pivot points and the position of the crossover.

Procedure:

- 1) Focus the beam to a spot with C2.
- 2) Choose tilt alignment x . Start with zero wobbler amplitude A_W , slowly increase the amplitude until the spot on the screen splits into two spots: the wobbler alternates between $+A_W$ and $-A_W$ offset on beam tilt- x , an incorrect pivot point will lead to shifts in opposite directions, splitting the spot in two.
- 3a) To find the correct specimen position when the pivot point as has been placed in the Auger electron deflector: adjust the C2 excitation to achieve this, and then refocus the spot on the specimen by varying the objective lens excitation and the specimen height. This last adjustment cannot be done very accurately, but it should get the specimen in the range where you can perform step 3b without moving the pivot point positions too much.
- 3b) Adjust the tilt pivot point distance Z until the spots are as close as they can get.
- 4) Adjust the rotation correction until the spots coincide.
- 5) Repeat steps 2 to 4 for the y -direction.
- 6) Increase the wobbler amplitude and repeat steps 3 to 5 to get a better alignment.

Note that because an incorrect tilt pivot point setting causes beam shift, setting the pivot point to the correct position will remove this shift, causing the beam to move. If necessary, adjust the shift to keep the spot in view.

A.1.5 Beam tilt alignment

The purpose of this alignment is to let the beam go through the center of the objective lens. If this alignment is not correct, changing the objective lens strength will cause beam shift. Note that the tilt pivot point alignment must have been carried out.

Procedure:

- 1) Focus the beam to a spot with C2.
- 2) Modulate the objective lens (rotate the camera length knob as far counter clockwise as it will go, push the button in the knob, and rotate the knob one click further counter clockwise).
- 3) Adjust beam tilt until the spot only changes size concentrically, without movement of the spot center.

A.1.6 Shift pivot point alignment

This is very similar to beam tilt alignment, but now the pivot points for beam shift must be adjusted so that shift causes only shift on the specimen - without tilt. In principle this can be done by a procedure similar to the one for tilt pivot point alignment, but then in diffraction mode. The rotation correction in step 4 of the tilt pivot point alignment must have been performed first.

The correct position of the pivot point for beam shift is in the back focal plane of the objective lens. *In practice this is difficult: the back focal plane is far from the scan coils, making it hard to tune the pivot point position, and the available range for shift is small (because the scan coils are working almost 1:1 against each other, the netto tilt in the pivot point is relatively small).* An incorrect, but easier method is to tilt the beam near C2. This position will cause tilt during shift (but relatively little) and the range for shift is much larger. Using this method, the alignment simply consists of setting both pivot points to 0 mm.

A second advantage of this position, is that only one scan coil excitation is changed when the spot is moved. If both the upper and lower scan coils are used the ratio between the excitations is critical, and because the digital to analog converters make finite steps jumps can be observed as the ratio between the coils changes, leading to artifacts when a line or two-dimensional position scan is made. Setting the pivot point to -25 mm (in the upper scan coil) does not have the same effect because the rotation correction takes place in the upper coils, so now the ratio between x and y coils is critical.

A.1.7 12-pole alignment

The alignments of the 12-pole consist of setting the rotation of the dipole and setting the centers of the quadrupoles and sextupoles. The rotation of the dipole is a matter of preference and can be chosen freely.

Centering the quadrupole

If the centers of the quadrupoles do not coincide with the beam center, a change in their excitation will cause the beam to move. The alignment procedure is therefore as follows:

- 1) Turn the strengths of the quadrupoles to zero. Focus the beam to a spot with C2 and place the spot in a known position (for instance the small circle in the center of the screen).
- 2) Increase the x -quadrupole strength until maximum or until the spot threatens to leave the screen.
- 3) Set the x -quadrupole x -shift and y -shift so that the spot center is back in the original position.
- 4) Turn the x -quadrupole to zero strength, and repeat steps 2 and 3 for the y -quadrupole.

Note that the quadrupole alignment button has three states: If it is off (red light) pushing it once will select the x -quadrupole alignment and will switch the light to green, pushing it a second time will select the y -quadrupole alignment (the light stays green). All further pushes will toggle between x -quadrupole and y -quadrupole alignment.

Centering the sextupole

This procedure is identical to the quadrupole alignment procedure, just read sextupole wherever it says quadrupole in the above.

Quadrupole strength

The quadrupole strength should be set to achieve the roundest spot on the specimen. The condenser stigmator however has a much larger range, and (with the 12-pole quadrupole contribution off) it should be adjusted first for optimum roundness, after which the 12-pole generated quadrupole should be used for the final adjustment. Image the probe on the viewing screen, and choose successively larger magnifications, so that the (un)roundness of the spot can be seen clearly.

The adjustment consists of setting strength and rotation. Although the idea seemed good at the time of the control software development, results in practice indicate that a conventional control, with two independent quadrupole strengths, is perhaps easier to work with.

Sextupole strength

The sextupole should be adjusted after the quadrupole, to remove the final unroundness from the probe. We have not yet been able to make such small probe sizes that this effect becomes important (because of mechanical or electrical disturbances).

A.2 Auger electron optics alignment

The Auger electron optics can be divided into the parallelizer, the deflector, the transport lens, and the spectrometer. For each of these alignment procedures are given below.

A.2.1 Parallelizer coil alignment

The parallelizer coil extends the $1/z^2$ monopole field of the objective lens until the magnetic aperture just below the Auger electron deflector. The alignment consists of tuning the parallelizer coil current to the objective lens current so that the sum of the magnetic fields best approximates

the monopole field. This probably manifests itself as a maximization of the collection efficiency, i.e., a maximization of the Auger electron count rate.

The same can be said for the small extra coil at the end of the parallelizer. At the moment this coil experiences the same current as the parallelizer coil, but in opposite direction (to minimize the bump near the magnetic aperture, see Fig. 4.8 on page 59).

An alternative, but rather trial-and-error method, consists of trying successive parallelizer and transport optics settings and minimizing the periodic focusing effect of the parallelizer. When you've found such a setting: *store it!*

Perhaps the safest method is to make a best $1/z^2$ fit to the measured fields, and to adjust the coil currents accordingly. Small adjustments to maximize the count rate can then be done without much risk of finding a local optimum.

A.2.2 Auger deflector alignment

The Auger electron deflector influences two beams: the primary electron beam, and the beam of Auger electrons. The alignments therefore also consist of two parts: the first is the effect on the primary beam (no tilt or shift) and the second is the effect on the Auger electrons (deflection over 90° by the largest possible range of Auger electron energies). The primary beam alignment must be performed first, so that the second alignment can be performed without moving the beam over the specimen.

Primary beam alignment

The purpose of this alignment is to let the combination scan coils, pre-deflector, and Auger electron deflector have no effect on the primary beam: no tilt or shift at the specimen. The alignment consists of tuning the scan coil and pre-deflector settings so that they provide the correct deflections to compensate the effect of the electrostatic and the magnetic field of the Auger deflector.

Procedure:

- 1) Turn the Auger energy down to 0 eV, turn the E percentage to 100% and the B percentage to 0%. Degauss the deflectors by pushing the Auger energy button twice (the light in this button should flash for several seconds during the degauss procedure).
- 2) Focus the beam to a spot with C2, place the spot in a known position (preferably the small circle in the center of the viewing screen).
- 3) Switch on the objective lens modulator (see beam tilt alignment), the spot should change size concentrically around the position chosen in step 2.
- 4) Turn up the Auger energy by about 100 eV (or less if the spot threatens to leave the screen).
- 5) Check the scan coil rotation setting: changing the scan coil percentage should move the spot along the same line as changing the pre-deflector percentage does. If you cannot complete the next step try changing the rotation over 180° .
- 6) Change the scan coil and pre-deflector settings so that the image is the same as in step 3. Note that if you turn down the pre-deflector you need to degauss it, if this causes the spot to move (off screen) turning *up* the pre-deflector should bring it back: by degaussing the remanent magnetic field has become less strong and more current is needed to create the

- same total field.
- 7) Repeat steps 4 to 6 until an Auger energy of about 1 keV has been reached. Then turn the energy down to 0 eV, and the E percentage to 0% and the B percentage to 100%. Degauss again.
 - 8) Turn up the Auger energy, do this very slowly to start with (about 1 to 3 eV at a time). Later on successively larger steps can be made.
 - 9) Repeat steps 4 to 6. Note that turning down the energy requires degaussing afterwards.

Auger beam alignment

The purpose of this alignment is to adjust the electrostatic and magnetic field so that the largest energy range can pass over 90° . Setting the E and B percentages to 100% uses the build in estimates for the effect of the two fields. Especially the estimate for B is not very accurate. A first alignment consists of finding the B percentage that produces maximum count rate with the E percentage set to zero, and then choosing double that value for B , and a 100% for E . This is however still not very accurate because it is difficult (due to hysteresis) to adjust B for maximum count rate. The procedure below produces a graph from which better estimates can be found. For this calibration you need to be able to measure the Auger electron count rate. The best is to use the computed transport lens settings, but if this fails (you do not count any electrons), you can try to use the lens as a drift tube.

Procedure:

- 1) Tune both the E and B percentages to 100%, set the Auger deflector to the energy with which the zero-energy secondary electrons will pass through it (the potential difference between the Auger deflector and the sample, $V_7 - V_{spec}$), select the secondary electron peak and tune the analyzed Auger energy (not the Auger deflector energy!) so that the count rate is at its maximum.
- 2) The easiest way to do the sequence of measurements is to start at a weak Auger deflector setting and slowly increase the setting (in this way you do not need to degauss after every step). Turn the E percentage down to 5 to 10% (so you have some room for tuning), turn the B percentage down to 0%, and degauss.
- 3) Turn up the B percentage by 5 to 10%. Even if the primary beam alignment of the previous section has been performed, the beam will probably still move, adjust beam shift so that the same part of the specimen is illuminated. Tune the E percentage to maximize the count rate. Write down the E and B percentages at which the maximum occurs.
- 4) Repeat step 3 until the B or E percentage is at about 180%, or at the limit of a power supply (you will hear a beep when you try to increase a setting which is near its limit). Note that as the E and B percentages come closer to the achromatic point the count rate gets harder to maximize.
- 5) Make a graph of the points you measured, see Fig. A.1 for an example. Where the straight line intersects the $E = 0$ axis, is where the B percentage is at half its optimum value: only the magnetic force is used to deflect the electrons over 90° . At the achromatic point the magnetic force is twice as strong, and the electrostatic force works in the opposite direction to compensate (and is therefore half the optimum magnetic force). So the optimum B percentage (B_{opt}) is twice the value of where the line intersects the $E = 0$ line. The optimum E percentage is found by the point on the straight line with $B = B_{opt}$.

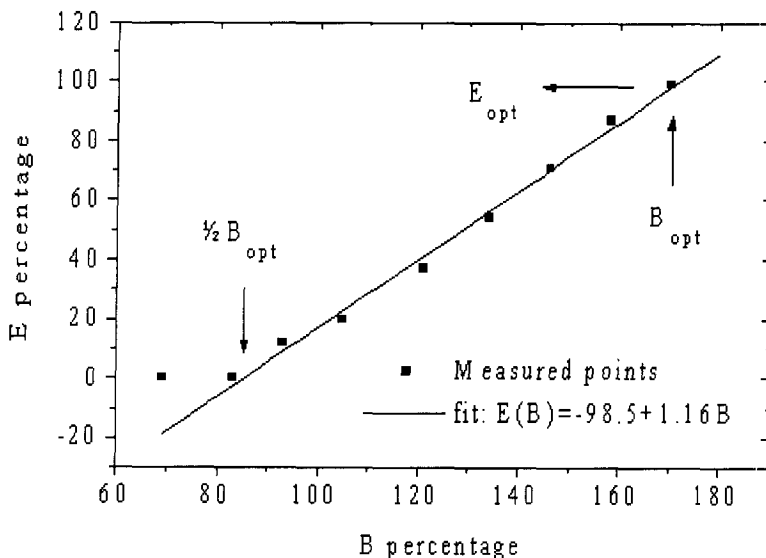


Figure A.1 Auger deflector alignment: the points are measured B and E percentages producing maximum count rate. Because the first two points both have $E = 0$ the first of these two has not been used for the straight line fit. The optimum B and E are found from the straight line fit by assuming $E(\frac{1}{2}B_{opt}) = 0$ and $E_{opt} = E(B_{opt})$. This results in $B_{opt} = 170\%$ and $E_{opt} = 99\%$.

A.2.3 Transport lens alignment

The transport lens consists of seven electrodes with potentials V_1 to V_7 . V_1 is determined by the energy which is analyzed and is described in more detail in the next section. V_2 to V_6 are derived from interpolation between the two closest energies for which optimum settings have been found from simulations. By choosing the percentage (between 0 and 200%) of the interpolated value that is actually used it is possible to tune these settings. Because the simulations sometimes jump between modes of operation the interpolation may be far from optimum, and there is no clear optimization routine: just fiddle with the percentages of V_2 and V_6 until you see optimum transmission. Be careful not to optimize on one energy: the gain there may be the loss at other energies, and doing an energy scan may reveal that the only energy transmitted is the one that was optimized. Finally V_7 can be chosen freely between -100 and +100 V. It is usually set to +60V to further accelerate low energy electrons.

A.2.4 Auger spectrometer alignment

The parameters to adjust are the entrance slit width, the exit slit width, the voltage V_{180} over the hemisphere, and the potential difference $V_1 - V_{spec}$ between the analyzer and the specimen.

Slit widths

For a parallel detector with 48 energy channels the optimum entrance slit width is 0.43 mm^6 . The exit slit should be wide open when using the parallel detector, or it should be set to the width of one channel (0.5 mm) in serial mode. If the system is used in serial mode, a setting with lower pass energy and wider slits is more optimal (from a transmission point of view). The transport lens will also have to be re-optimized if such a different setting is used.

Voltage V_{180} over the hemisphere

The voltage over the hemisphere is given by $V_{180} = f_{180} C_{180} U_{180}$, where f_{180} (= 0 to 200%) is a fraction set by the user during alignment, C_{180} is a spectrometer constant, and U_{180} is the spectrometer central energy. Because $U_{180} = E_{RES} R_{180} / 2d_{chan}$ is a function of the energy resolution E_{res} (energy range per detector channel) the calibration of V_{180} with f_{180} should be done so that the detector covers an energy range ΔU equal to the number of energy channels times the energy resolution. This can only be done by measuring known energy spectra, and adjusting f_{180} until this condition is met.

The spectrometer constant $C_{180} = 2R_{180}(R_o - R_i) / q R_o R_i$, where q is the electron charge and R_o (= 166 mm), R_{180} (= 138.5 mm), and R_i (= 111 mm) are the analyzer outer, central, and inner radii, respectively. This gives a value of $C_{180} = 5.17 \cdot 10^{18} \text{ C}^{-1}$.

Finally d_{chan} (= 0.5 mm) is the width of an energy channel, given by the width of the detector (24 mm) divided by the number of energy channels (48).

Voltage difference between analyzer and specimen

If we wish to analyze electrons that leave the specimen with energy U_0 we need to accelerate or decelerate them to the central energy of the spectrometer, U_{180} . To achieve this the voltage difference between the spectrometer and the specimen must be $V_1 - V_{SPEC} = (U_0 - U_{180}) / q$, where V_1 is the spectrometer central potential, V_{SPEC} is the specimen potential, and q is the electron charge. Because U_{180} is a function of the analyzer resolution (alignment), the voltage difference needs to be recalibrated when the energy resolution setting is changed or recalibrated.

The potential of the specimen may be chosen freely, and should be used to optimize the collection efficiency and minimize the time-of-flight of low energy electrons, by accelerating these as soon as they leave the specimen. This then determines $V_1 = f_1 (V_{SPEC} + (U_0 - U_{180}) / q)$, where f_1 (between 0 and 200%) is the percentage set during alignment.

It should be noted that f_1 adjusts the slope of the energy-voltage relation, there is no provision to change the offset in this relation. As long as the P80 power supplies do not control the specimen voltage (as is the case at the moment of writing) an offset can be introduced by having a difference between the laboratory power supply that sets the specimen voltage, and the value which has been 'told' to the P80 system. Another option - if the energy range that falls on the detector is not critical - is to change the energy resolution correction factor f_{180} , in turn changing the analyzer pass energy U_{180} .

A.3 References

1. Gatan Inc., *Instruction manual for Electron Energy Loss Spectrometer Model 607*, Pleasanton California, USA (1982), unpublished.
2. H. Brink, *The Post EELS Optics*, graduation report Delft University of Technology, The Netherlands (1995), unpublished.
3. N.V. Philips Gloeilampenfabrieken, *Operating Instructions EM430*, part no. 9432 060 09001, Eindhoven, The Netherlands (1983), unpublished.
4. Dawn Chescoe and Goodhew, P.J., *The Operation of Transmission and Scanning Electron Microscopes*, Oxford University Press, Oxford, UK (1990).
5. Peter Sell, *Outline of the alignment of a TEM*, ASU Winter School 1991, Arizona State University, Arizona, U.S.
6. M.A.J. van der Stam, J.E. Barth and P. Kruit, Design of a multi mode transport lens with optimization program SOEM, *Proc. SPIE conference on Charged-Particle Optics*, W.B. Thompson, M. Sato, A.V. Crewe, Eds., SPIE - The International Society for Optical Engineering, Bellingham, **2014** (1993), 45-56.

Appendix B - Tables

B.1 Spectra file format

Offset	Length	Format	Function
0	81	string[80]	Spectrum title
81	81	string[80]	Label x-axis
162	81	string[80]	Label y-axis (unused for one-dimensional spectra)
243	81	string[80]	Label z-axis
324	13	string[12]	Original file name
337	2	word	Original file date - years
339	2	word	Original file date - months
341	2	word	Original file date - days
343	2	word	Original file date - hours
345	2	word	Original file date - minutes
347	2	word	Original file date - seconds
349	4	longint	<i>DimX</i> , Dimension x-direction (# of points)
353	4	longint	<i>DimY</i> , Dimension y-direction (# of points)
357	8	double	<i>MinX</i> , Minimum x-axis (x-value at first point)
365	8	double	<i>MaxX</i> , Maximum x-axis (x-value at last point)
373	8	double	<i>MinY</i> , Minimum y-axis (y-value at first point)
381	8	double	<i>MaxY</i> , Maximum y-axis (y-value at last point)
389	4	longint	<i>DataSize</i> , # of bytes per point
393	4	longint	Data type (0 = unsigned, 1 = signed, 2 = float)
397	<i>DimX</i> · <i>DimY</i> · <i>DataSize</i> bytes of data		

Table B.1 Format of the data files for storing spectra. The files start with a 397 byte header, followed by $DimX \cdot DimY \cdot DataSize$ bytes which contain the z-data for each point. The sequence is $z[1,1], \dots, z[1,DimX], \dots, z[DimY, dimX]$. All data types are Pascal style, e.g. a string[80] consists of 1 byte with the string length followed by 80 bytes of string content. The currently defined formats for the z-data are unsigned, signed, and float, assuming $DataSize = 4$ this would mean a dword, longint, and single, respectively.

B.2 Transport lens settings

Res [eV]	Energy [eV]	U_1 [eV]	U_2 [eV]	U_3 [eV]	U_4 [eV]	U_5 [eV]	U_6 [eV]	U_7 [eV]
1.0	2100	537.6	1539.3	2824.4	13999.9	962.9	2149.6	2100
1.0	1600	537.6	1632.6	2635.9	13992.3	1143.5	1567.3	1600
1.0	1100	537.6	964.9	3722.4	14000.0	930.4	1117.9	1100
1.0	600	537.6	811.9	3349.7	13997.8	1198.3	559.9	600
1.0	300	537.6	734.5	3238.4	14000.0	1423.2	262.0	300
1.0	150	537.6	1026.1	6354.6	14000.0	1020.5	117.1	150
1.0	60	537.6	1623.2	8455.4	1887.4	365.8	49.0	60
0.8	2100	403.2	1557.0	3469.3	13999.9	786.7	2205.1	2100
0.8	1600	403.2	1416.1	3198.8	14000.0	920.4	1626.3	1600
0.8	1100	403.2	1153.3	2947.8	13999.9	1122.4	1089.0	1100
0.8	600	403.2	994.4	2642.0	14000.0	1471.9	577.7	600
0.8	300	403.2	817.8	2759.6	13993.8	1609.0	260.3	300
0.8	150	403.2	776.5	3560.9	14000.0	1382.9	100.8	150
0.8	60	403.2	1395.2	6865.9	1488.4	282.0	52.7	60
0.5	2100	268.8	1237.0	2764.5	9871.9	439.4	2322.9	2100
0.5	1600	268.8	1190.1	2715.6	10261.0	524.9	1695.3	1600
0.5	1100	268.8	1093.4	2579.5	10671.7	660.3	1114.3	1100
0.5	600	268.8	914.8	2330.5	11093.5	924.7	585.1	600
0.5	300	268.8	766.5	2230.8	11314.4	1184.5	278.9	300
0.5	150	268.8	669.0	2360.1	11184.6	1230.4	112.2	150
0.5	60	268.8	553.8	3535.2	6687.2	478.3	43.1	60
0.25	2100	134.4	641.2	1374.5	4345.0	127.3	2716.2	2100
0.25	1600	134.4	642.2	1399.1	4622.9	162.5	1923.1	1600
0.25	1100	134.4	622.1	1386.3	4903.9	212.9	1226.1	1100
0.25	600	134.4	558.2	1305.8	5284.7	312.8	612.6	600
0.25	300	134.4	458.5	1169.1	5560.9	463.0	293.0	300
0.25	150	134.4	380.6	1110.0	5629.8	589.6	139.5	150
0.25	60	134.4	313.8	1218.7	5416.1	578.9	40.1	60
0.1	2100	53.8	224.7	448.2	1188.9	14.1	4228.9	2100
0.1	1600	53.8	241.7	496.2	1409.0	21.8	2665.1	1600
0.1	1100	53.8	253.9	535.2	1624.9	38.5	1550.4	1100
0.1	600	53.8	255.1	558.1	1865.7	68.2	713.9	600
0.1	300	53.8	234.6	537.7	2062.8	109.0	315.1	300
0.1	150	53.8	195.6	483.0	2194.3	164.7	147.6	150
0.1	60	53.8	152.6	444.7	2255.5	236.2	55.9	60

Table B.2 Calculated optimum transport lens settings for five energy resolutions and seven transport lens entrance (deflector exit) energies. Figure B.1 shows how the energies are translated to voltages on the transport lens.

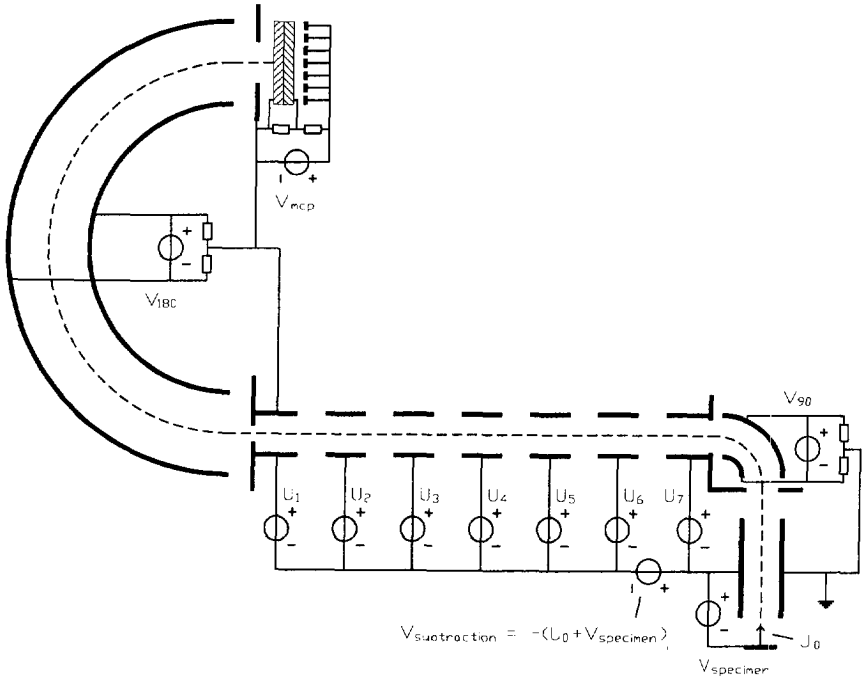


Figure B.1 Overview of the voltage supplies in the Auger electron analysis system. The specimen is normally at -240 V . The Auger electron deflector is normally at $+60\text{ V}$ (U_7). A negative high voltage supply is set so that the electrons that leave the specimen with the energy of interest (U_0) have zero energy with respect to its output. Supplies U_1 to U_6 than directly set the energy the electrons have at electrodes 1 to 6.

B.3 Remote control commands

Value	Associated command	#	of bytes of additional data
100h	Send Auger energy	4	longint (lo/hi word) energy in meV
101h	Send Auger resolution	4	longint (lo/hi word) resolution in eV
102h	Request Auger energy	0	
200h	Send EELS energy	4	longint (lo/hi word) energy in meV
300h	Mark current shift as origin	0	
301h	Send x-offset relative to origin	4	longint (lo/hi word) offset in Å
302h	Send y-offset relative to origin	4	longint (lo/hi word) offset in Å
Value	Associated reply	#	of bytes of additional data
8000h	Last received message was OK	0	
8001h	Checksum error	0	
8002h	Packet too small (< 6 bytes)	0	
8003h	Packet too large (> 1024 bytes)		
8004h	Packet timed out	0	
8005h	Unknown command/reply	0	
8100h	Not enough data	0	
8101h	Too much data	0	

Table B.3 Command codes to, and reply codes from, the microscope control PC, their meaning, and additional data (if required).

Summary

In the Charged Particle Optics Group in Delft a Transmission Electron Microscope has been build in which not only energy loss electrons can be analyzed, but also secondary and Auger electrons. This thesis describes the work done in the 'Coincidence Electron Spectroscopy at Nanometer Scale' project, aimed at the detection of time-coincidences between the energy-loss and the secondary electrons, using multi channel detectors to decrease the measurement times:

Fast (10^5 cps per channel) parallel-channel electron detectors with nanosecond timing resolution were designed, based on micro channel plates and multi strip anodes. The energy loss electron detector has 192 channels, the secondary electron detector has 96 channels. By integrating the anodes with the multi-pin vacuum feedthrough the design has been kept compact, and many wiring problems have been avoided.

A matching data acquisition system, largely based on the commercial PCOS III system by LeCroy, has also been designed and build. A dual-transputer processing unit allows flexible processing of the data stream from the PCOS system. In this way different experiments can be performed easily, by reprogramming the transputers.

The project also required computer control over parts of the microscope, for example to be able to make line- or 2-dimensional scans over the specimen. This has also been realized, including a user friendly interface.

Finally the first measurements using the microscope are presented, including Auger, energy loss, and coincidence spectra.

Samenvatting

Nederlandse titel:

'Instrumentatie voor Parallel-Parallel Coincidentie Elektronen Spectroscopie'

In de vakgroep Deeltjes Optica in Delft is een Transmissie Elektronen Microscop gebouwd waarmee niet alleen energieverlies elektronen, maar ook secundaire en Auger elektronen geanalyseerd kunnen worden. Dit proefschrift beschrijft werk dat gedaan is in het kader van het 'Coincidence Electron Spectroscopy at Nanometre Scale' projekt, gericht op de detectie van energieverlies en secundaire elektronen in tijdcoincidentie, gebruikmakend van meerkanaals detectoren om de meettijd te verkorten:

Snelle (10^5 cps per kanaal) parallelle elektronen detectoren met nanoseconde tijd-resolutie zijn ontworpen, gebaseerd op micro-channel-plates en multi-strip-anodes. De energieverlies detector heeft 192 kanalen, en de sekundaire elektronen detector heeft 96 kanalen. Door het integreren van de anodes op de multi-pin vacuüm doorvoer is het ontwerp compact gebleven, en zijn veel bedradingsproblemen vermeden.

Een bijpassend data acquisitie systeem, grotendeels gebaseerd op het PCOS III systeem van LeCroy, is eveneens ontworpen en gebouwd. Een twee-transputer rekeneenheid maakt het mogelijk de datastroom uit het PCOS systeem flexibel te verwerken. Op deze manier is het mogelijk om verschillende experimenten uit te voeren, simpelweg door het herprogrammeren van de transputers.

Het projekt vereiste ook computerbesturing van delen van de microscoop, onder andere om lijn- en tweedimensionale scans te kunnen maken. Dit is ook gerealiseerd, samen met een gebruikersvriendelijke interface.

Tenslotte worden de eerste metingen met de microscoop gepresenteerd, waaronder Auger, energieverlies, en coincidentie spektra.

Curriculum vitae

Jacob Simon Faber (beter bekend als Pybe) is geboren te Amsterdam, op 19 maart 1966. Tijdens zijn jeugd heeft hij onder andere in Indonesië en in Lesotho (Afrika) gewoond. In 1985 heeft hij het VWO examen op het Erasmus College in Zoetermeer behaald, waarna hij Technische Natuurkunde is gaan studeren aan de TH Delft. In 1991 is hij afgestudeerd aan de TU Delft, bij de vakgroep Deeltjes Optica, op het onderwerp 'Possibilities for Parallel Detectors in Coincidence Measurements'. Na erkend te zijn als gewetensbezwaarde heeft hij 16 maanden vervangende dienstplicht gedaan, wederom bij de vakgroep Deeltjes Optica. Daarna is hij nog 32 maanden in dienst geweest bij de Stichting Fundamenteel Onderzoek der Materie (FOM), werkzaam als Onderzoeker In Opleiding, alweer bij de vakgroep Deeltjes Optica. Sinds 1 januari 1996 werkt hij bij Philips Electron Optics B.V te Eindhoven.